Supplementary Material: Variational approach to open quantum systems with long-range competing interactions

Dawid A. Hryniuk[1,2,*] and Marzena H. Szymańska[1]

[1] *Department of Physics and Astronomy, University College London, Gower Street, London, WC1E 6BT, United Kingdom*
[2] *London Centre for Nanotechnology, University College London, Gordon Street, London WC1H 0AH, United Kingdom*

(Dated: December 18, 2025)

CONTENTS

* d.hryniuk@ucl.ac.uk

SUPPLEMENTARY NOTE 1. T-VMC+MPO METHOD – ADDITIONAL DETAILS

A. Sequential Metropolis sweep

The MPO ansatz for the density matrix after vectorization into a MPS is explicitly given by

$$|\rho\rangle = \sum_{\{x_i\}} \sum_{\{\alpha_i\}} A^{x_1}_{\alpha_1\alpha_2} \dots A^{x_N}_{\alpha_N\alpha_1} |x_1 \dots x_N\rangle , \tag{S1}$$

where $\{x_i\}$ and $\{\alpha_i\}$ are called the "physical" and "virtual" indices of the MPO, respectively. Our approach relies on sampling representative many-body configurations $\{\boldsymbol{x}\}$ from the distribution $p(\boldsymbol{x}) = |\langle \boldsymbol{x}|\rho(t)\rangle|^2 / \sum_{\boldsymbol{y}} |\langle \boldsymbol{y}|\rho(t)\rangle|^2$, where the probability amplitudes become

$$\langle \boldsymbol{x}|\rho\rangle = \sum_{\{\alpha_i\}} A^{x_1}_{\alpha_1\alpha_2} \dots A^{x_N}_{\alpha_N\alpha_1}. \tag{S2}$$

An efficient and cost-effective approach is to apply a sequence of Metropolis updates on each site of the lattice [1]. Let us define the partial matrix products

$$L_j = \sum_{\{\alpha_i\}} A^{x_1}_{\alpha_1\alpha_2} \dots A^{x_j}_{\alpha_j\alpha_{j+1}}, \qquad R_j = \sum_{\{\alpha_i\}} A^{x_j}_{\alpha_j\alpha_j+1} \dots A^{x_N}_{\alpha_N\alpha_1}, \tag{S3}$$

which satisfy the recurrence relations $L_{j+1} = L_j A^{x_{j+1}}_{\alpha_{j+1}\alpha_{j+2}}$ and $R_{j-1} = A^{x_{j-1}}_{\alpha_{j-1}\alpha_j} R_j$ with $L_0 = R_{N+1} = \mathbb{1}$. We also note that $\langle \boldsymbol{x}|\rho\rangle = L_N = R_1$. To generate a new sample $\boldsymbol{x}'$ given an existing sample $\boldsymbol{x}$ with $q = \langle \boldsymbol{x}|\rho\rangle$ and a set $\{R_j\}$ we proceed for $j = 1, \dots, N$ as follows:

1. Propose a new single-body configuration x'_j from a uniform proposal distribution.
2. Calculate the Metropolis acceptance probability $p(x_j \leftarrow x'_j) = q'/q$ where $q' = \operatorname{tr} L_{j-1} A(x'_j) R_{N-j}$.
3. With probability $p(x_j \leftarrow x'_j)$, set $x_j \leftarrow x'_j$ and $q \leftarrow q'$.
4. Compute and store $L_j = L_{j-1} A(x_j)$.

The above algorithm produces a new Monte Carlo sample $\boldsymbol{x}'$ and a set of partial matrix products $\{L_j\}$, to be reused at later points of the method, at a computational cost of $2N\chi^3$. One can also proceed in reverse, generating $\{R_j\}$.

B. Contraction of the local estimator

Here we discuss the efficient computation of the local estimator of the Lindbladian, $\mathcal{L}_{\text{loc}}(\boldsymbol{x}) = \frac{\langle \boldsymbol{x}|\mathcal{L}|\rho\rangle}{\langle \boldsymbol{x}|\rho\rangle}$, for Lindbladian and density operators in MPO form. An arbitrary Liouville-space operator l can be put into MPO form:

$$l = \sum_{\{u_i\},\{v_i\}} \sum_{\{\beta_i\}} B^{u_1 v_1}_{\beta_1\beta_2} \dots B^{u_N v_N}_{\beta_N\beta_1} |u_1 \dots u_N\rangle \langle v_1 \dots v_N| \tag{S4}$$

One therefore obtains for the numerator:

$$\langle \boldsymbol{x}| l |\rho\rangle = \sum_{\{\alpha_i\},\{\beta_i\}} M^{x_1}_{(\beta_1\alpha_1)(\beta_2\alpha_2)} \dots M^{x_N}_{(\beta_N\alpha_N)(\beta_1\alpha_1)}, \tag{S5}$$

where $M^{x_i}_{(\beta_i\alpha_i)(\beta_{i+1}\alpha_{i+1})} := \sum_{v_i} B^{x_i v_i}_{\beta_i\beta_{i+1}} A^{v_i}_{\alpha_i\alpha_{i+1}}$. An important simplification occurs for quasi-local operators $l^{[n]}_j$, with explicit MPO form

$$l^{[n]}_j = \sum_{\{u_i\},\{v_i\}} \sum_{\{\beta_i\}} \delta^{u_1 v_1}_{\beta_1\beta_2} \dots \delta^{u_{j-1} v_{j-1}}_{\beta_{j-1}\beta_j} B^{u_j v_j}_{\beta_j\beta_{j+1}} \dots B^{u_{j+n-1} v_{j+n-1}}_{\beta_{j+n-1}\beta_{j+n}} \delta^{u_{j+n} v_{j+n}}_{\beta_{j+n}\beta_{j+n+1}} \dots \delta^{u_N v_N}_{\beta_N\beta_1} |u_1 \dots u_N\rangle \langle v_1 \dots v_N| , \tag{S6}$$

for which the contracted numerator in the local estimator can be written as (suppressing virtual indices)

$$\langle \boldsymbol{x}| l^{[n]}_j |\rho\rangle = A^{x_1} \dots A^{x_{j-1}} M^{x_j} \dots M^{x_{j+n-1}} A^{x_{j+n}} \dots A^{x_N} \tag{S7}$$

$$= L_{j-1} M^{x_j} \dots M^{x_{j+n-1}} R_{j+n}. \tag{S8}$$

Since $\boldsymbol{x}$ is a sample drawn during a sequential Metropolis sweep, either of the partial matrix products $\{L_j\}$ and $\{R_j\}$ have already been computed and stored to memory. As such, they can be recalled to reduce the total number of contractions necessary in the computation of the numerator. For the n-local Lindbladian $\mathcal{L} = \sum_{j=1}^{N} l_j^{[n]}$ we therefore obtain

$$\mathcal{L}_{\mathrm{loc}}(\boldsymbol{x}) = \langle \boldsymbol{x}|\rho\rangle^{-1} \sum_{j=1}^{N} L_{j-1} M^{x_j} \dots M^{x_{j+n-1}} R_{j+n}. \tag{S9}$$

Another critical simplification occurs for the diagonal part of the Lindbladian, for which all tensor contractions vanish. To see this, we rewrite the local estimator as

$$\mathcal{L}_{\mathrm{loc}}(\boldsymbol{x}) = \frac{\langle \boldsymbol{x}| \mathcal{L} |\rho\rangle}{\langle \boldsymbol{x}|\rho\rangle} = \sum_{\{\boldsymbol{y}\}} \langle \boldsymbol{x}| \mathcal{L} |\boldsymbol{y}\rangle \frac{\langle \boldsymbol{y}|\rho\rangle}{\langle \boldsymbol{x}|\rho\rangle}, \tag{S10}$$

where the ratio of probability amplitudes cancels out for the diagonal part of $\mathcal{L}$. The contraction procedures described above significantly reduce the computational cost of computing the local estimator and log-derivative gradient for most Lindbladians of interest, and especially for periodic lattices with a period $D < N$, as compared to introducing an explicit summation over auxiliary configuration $\{\boldsymbol{y}\}$ in Eq. (S10), a necessity in other VMC algorithms. The computational cost of computing the numerator in Eq. (S9) for N (translationally-symmetric) operators $\{l_j^{[n]}\}_{j=1}^{N}$ is $2N\chi^3$ (assuming $\{M\}$, L_{j-1}, and R_{j+1} are known, and excluding the cost of contracting the $\{M\}$ matrices with each other, which would depend on the specific bond dimensions of $\{M\}$ and the period D). This should be contrasted with the cost of computing

$$\sum_{j=1}^{N} \langle \boldsymbol{x}| l_j^{[n]} |\rho\rangle = \sum_{j=1}^{N} \sum_{\{\boldsymbol{y}\}} \langle \boldsymbol{x}| l_j^{[n]} |\boldsymbol{y}\rangle \langle \boldsymbol{y}|\rho\rangle = \sum_{j=1}^{N} \sum_{\{\boldsymbol{y}\}} \langle \boldsymbol{x}| l_j^{[n]} |\boldsymbol{y}\rangle L_{j-1} A^{y_j} \dots A^{y_{j+n-1}} R_{j+n}, \tag{S11}$$

which is $d^{2n}N(n+1)\chi^3$, explicitly scaled by an additional factor of d^{2n}. Admittedly, the former approach additionally requires the computation and contraction of the $\{M\}$ tensors, which we have omitted from the cost-analysis above, but which is nevertheless far cheaper for sufficiently-local Lindbladian operators with small period D (for $n = 1$, this cost is only $Dd^4\chi^2$, while for $n = 2$, it is $D(d^4\chi^3 + d^8\chi^2)$).

C. Computation of log-derivative operator

The other essential quantity in the computation of the metric tensor and variational forces is the log-derivative operator. Fortunately, an efficient computation of the operator is yet again afforded by the $\{L\}$ and $\{R\}$ matrix products. As the most general case, we consider a periodic MPO with period $D \leq N$ (possibly aperiodic for $D = N$) and assign an index r with $1 \leq r \leq D$ to the variational parameter a_{uv}^{rs}. Defining $\bar{j} := \mathrm{mod}(j-1, D) + 1$, one obtains,

$$\frac{\partial}{\partial a_{uv}^{rs}} \langle \boldsymbol{x}|\rho\rangle = \frac{\partial}{\partial a_{uv}^{rs}} \sum_{\{\alpha_i\}} A^{x_1}_{\alpha_1\alpha_2} A^{x_2}_{\alpha_2\alpha_3} \dots A^{x_N}_{\alpha_N\alpha_1} \tag{S12}$$

$$= \sum_{\{a_i\}} \delta_{r\bar{1}}\delta_{sx_1}\delta_{u\alpha_1}\delta_{v\alpha_2} A^{x_2}_{\alpha_2\alpha_3} \dots A^{x_N}_{\alpha_N\alpha_1} + A^{x_1}_{\alpha_1\alpha_2}\delta_{r\bar{2}}\delta_{sx_2}\delta_{u\alpha_2}\delta_{v\alpha_3} \dots A^{x_N}_{\alpha_N\alpha_1} + \dots \tag{S13}$$

$$= \sum_{j=1}^{N} \delta_{r\bar{j}}\delta_{sx_j} \left[R_{j+1}L_{j-1}\right]_{vu}. \tag{S14}$$

Hence,

$$\Delta_{uv}^{rs}(\boldsymbol{x}) = \langle \boldsymbol{x}|\rho\rangle^{-1} \sum_{j=1}^{N} \delta_{r\bar{j}}\delta_{sx_j} \left[R_{j+1}L_{j-1}\right]_{vu}. \tag{S15}$$

The above has a worst-case computational cost of $N\chi^3$ (assuming $\langle \boldsymbol{x}|\rho\rangle$, $\{L\}$, and $\{R\}$ are known).

D. Algorithm summary

We summarize the key steps of our algorithm in Fig. S1, where we also sketch how to efficiently parallelize the computations. We regularize the metric tensor by a combination of a diagonal shift ϵ_{shift} and the S-regularization scheme of [2] with soft cutoff ϵ_{SNR}. When integrating the equations of motion, we either use a fixed step-sized forward-Euler integrator or a second order adaptive Heun integrator of [2] with tolerance ϵ_{tol}. After the tensor elements have been updated, they are renormalized to ensure $\operatorname{tr}\rho = 1$.

For two-dimensional translationally-invariant latices, we wrap the MPO around all sites of the lattices row-by-row (with periodic boundary conditions imposed in both dimensions), defining the row as the unit-cell of the lattice, and mapping the two-dimensional problem onto a one-dimensional one, with the nearest-neighbor interactions between rows becoming effective long-ranged interactions. This is worth contrasting with other variational MPO approaches for two-dimensional lattices, where cylindrical boundary conditions are used [3].

E. Computational cost

Below we summarize the computational cost of a single iteration of the t-VMC+MPO algorithm for N_{MC} Monte Carlo samples with a fixed step-size first-order Euler integration without regularization:

- $2(N-1)\chi^3 N_{\text{MC}}$ due to the computation of the $\{L\}$ and $\{R\}$ matrix products.
- $2N\chi^3 N_{\text{MC}}$ due to single sequential Metropolis sweep.
- $2N\chi^3 N_{\text{MC}}$ due to contraction of the local estimator of a Lindbladian.
- $2D^2d^4\chi^4 N_{\text{MC}} + D^3d^6\chi^6$ due to computation and inversion of the metric tensor.

Therefore, the total computational cost for a Lindbladian with N n-local terms has an asymptotic scaling of $O(N\chi^3 N_{\text{MC}} + D^2d^4\chi^4 N_{\text{MC}} + D^3d^6\chi^6)$ (omitting an n- and D-dependent term for the computation and contraction of the $\{M\}$ tensors in the contraction of the local estimator)

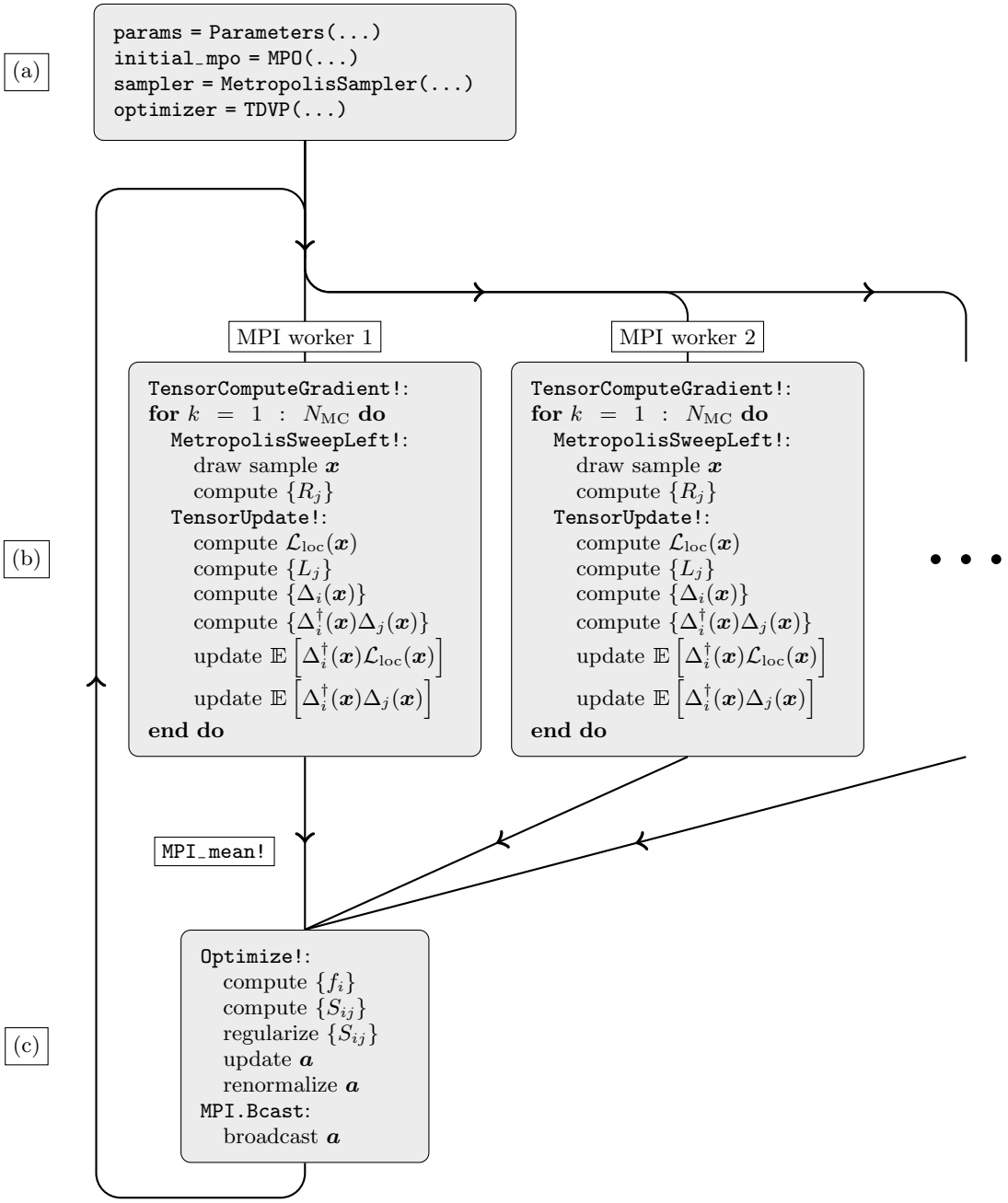

FIG. S1. **Flowchart of the essential elements of a single iteration of the t-VMC+MPO algorithm with first-order forward-Euler integration, referencing the names of functions called in our Julia implementation.** After (a) specifying the parameter values, the Metropolis sampler, the initial MPO, and the optimizer, (b) the core part of the overall computation can be split into separate MPI processes to be reduced before (c) updating the tensor elements. The (b)-(c) loop is then repeated for a chosen number of time steps.

SUPPLEMENTARY NOTE 2. ADDITIONAL CONVERGENCE TESTS

A. Overview

In this section we provide extensive convergence studies of our approach for six distinct models of dissipative spin chains:

1. Transverse-field Ising model with short-ranged interactions.

2. Transverse-field Ising model with weak long-ranged competing interactions.

3. Transverse-field Ising model with strong long-ranged competing interactions.

4. Transverse-field Ising model with super-long-ranged competing interactions.

5. XYZ model with short-ranged interactions.

6. XYZ model with long-ranged competing interactions.

In each model, the incoherent dissipation is induced by a one-local spin-loss Lindblad jump operators $\Gamma_k = \frac{\sqrt{\gamma}}{2}(\sigma_k^x - i\sigma_k^y)$ for $k = 1, \ldots, N$ with $\gamma = 1$ throughout, and all simulations start from the same initial condition $\langle \sigma^y \rangle = -1$. In addition, each model is considered for short ($N = 10$) and long ($N = 50$ or $N = 200$) chains, with the former being also treatable via exact integration of the Lindblad master equation, permitting direct comparison with exact dynamics. The exact dynamics for short chains are obtained with the help of the *QuantumOptics.jl* package [4]. For each variant of each model, we test the convergence of our algorithm with respect to five key hyperparameters:

1. MPO density operator bond dimension χ.

2. Number of Monte Carlo samples per iteration N_{MC}.

3. Second-order adaptive step-sizing tolerance parameter ϵ_{tol}.

4. Diagonal shift metric regularization parameter $\epsilon_{\mathrm{shift}}$.

5. Signal-to-noise metric regularization parameter ϵ_{SNR}.

For every considered hyperparameter values, we plot the non-equilibrium dynamics of the polarizations and connected 2-point correlation functions at 1, 2, and 3-site separation in each spatial direction, for a total of 12 distinct plots. In addition, for short chains, we also provide:

1. Complementary plots of the absolute errors over exact results, for another 12 distinct plots.

2. The evolution of the Rényi-2 entropy for the full density operator.

3. The smallest eigenvalue of the variational density matrix.

4. Schmidt singular values for a single, representative simulation.

5. A time-analysis for each simulation, where we plot the total number of iterations for each simulation and the average time per iteration (with error bars representing the standard deviation in iteration time over all iterations in each simulation).

In grand total, we provide 60 distinct figures below.

Each simulation was run for a maximum of 48 hours on 10 MPI processes each. As such, some of the most demanding calculations, particularly with very small adaptive step-size tolerances, did not complete within this timeframe.

B. Hamiltonians and parameters

The two Hamiltonians considered in this convergence analysis are:

1. Transverse-field Ising model:

$$H = \sum_n J_n \sum_{i,j} d_{ij}^{-\alpha_n} \sigma_i^z \sigma_j^z + h \sum_i \sigma_i^x, \tag{S16}$$

For Figs. 2-11 (short-range), $J = 0.5$, $\alpha = \infty$, $h = 1$.
For Figs. 12-21 (weak long-range), $J_1 = 0.5$, $\alpha_1 = 3$, $J_2 = -1.0$, $\alpha_2 = 6$, $h = 1$.
For Figs. 22-31 (strong long-range), $J_1 = 1.0$, $\alpha_1 = 3$, $J_2 = -2.0$, $\alpha_2 = 6$, $h = 1$.
For Figs. 12-21 (super-long-range), $J_1 = 0.5$, $\alpha_1 = 2$, $J_2 = -1.0$, $\alpha_2 = 4$, $h = 1$.

2. XYZ model:

$$H = \sum_n \sum_{\beta=\{x,y,z\}} J_n^\beta \sum_{i,j} d_{ij}^{-\alpha_n} \sigma_i^\beta \sigma_j^\beta + h \sum_i \sigma_i^z. \tag{S17}$$

For Figs. 42-51 (short-range), $\boldsymbol{J} = (0.6, -0.5, 0.4)$, $\alpha = \infty$, $h = 0.5$.
For Figs. 52-61 (long-range), $\boldsymbol{J}_1 = (0.6, -0.5, 0.4)$, $\alpha_1 = 3$, $\boldsymbol{J}_2 = (-0.9, 1.0, -1.1)$, $\alpha_2 = 6$, $h = 0.5$.

The interactions strengths are not renormalized.

C. Auxiliary hyperparameters

Besides the five key hyperparameters tested in this section, our results rely of a number of other minor hyperparameters. Those include:

1. Number of Monte Carlo sweeps in between samples: set to 5. A single sweep was found sufficient to give rise to virtually uncorrelated samples [1], but additional sweeps can be performed at very little added computational cost.

2. Number of burn-in Monte Carlo sweeps: set to 5.

3. Initial step size during adaptive step-sizing evolution: set to 10^{-8}. Must be initially set to a small number; it is increased to an appropriate size automatically.

4. Maximum allowed step size: set to 0.1. Improves resolution of the trajectories at larger tolerances.

D. Insights and recommendations

1. Convergence is improved for larger bond dimensions, larger number of samples, and smaller tolerance, although all come at a cost of more expensive computations.

2. Convergence is optimal for regularization parameters at around $\epsilon = 10^{-8}$ to $\epsilon = 10^{-10}$.

3. A larger interaction strength requires a larger bond dimension, number of samples, or step-size tolerance for convergence.

4. Longer-ranged interactions require a larger bond dimension, number of samples, or step-size tolerance for convergence.

5. Convergence does not seem to be adversely affected when the size of the system is increased, but becomes more expensive.

6. Smallest eigenvalue of the reduced density matrix for $N = 10$ is strictly non-negative in all simulations for $N = 10$, demonstrating that positive semi-definiteness of the ansatz is maintained throughout every simulation.

7. Step size decreases with decreasing ϵ_{shift}, but doesn't change with ϵ_{SNR}.

On the basis of the above observation, we recommend the following baseline hyperparameter values for the types of models studied in this work, which are to be refined for the specific problem at hand and desired accuracy:

1. $N_{\text{MC}} = 5000$

2. $\epsilon_{\text{tol}} = 0.01$

3. $\epsilon_{\text{shift}} = 10^{-8}$ (may be less if N_{MC} is sufficiently large and vice versa)

4. $\epsilon_{\text{SNR}} = 10^{-8}$ (may be less if N_{MC} is sufficiently large and vice versa)

The appropriate bond dimension must be determined empirically, depending on the desired accuracy.

E. Panel descriptions, $N = 10$

Panels (1a)-(6d): variational dynamics of magnetization and pair correlation functions obtained with t-VMC+MPO and compared with exact results; Columns (a) – magnetizations $\{\langle\sigma^\beta\rangle(t)\}_{\beta=\{x,y,z\}}$, (b) - nearest-neighbour correlation functions $\{[\langle\sigma_i^\beta\sigma_{i+1}^\beta\rangle - \langle\sigma_i^\beta\rangle\langle\sigma_{i+1}^\beta\rangle](t)\}_{\beta=\{x,y,z\}}$, (c) – next-nearest-neighbour correlation functions $\{[\langle\sigma_i^\beta\sigma_{i+2}^\beta\rangle - \langle\sigma_i^\beta\rangle\langle\sigma_{i+2}^\beta\rangle](t)\}_{\beta=\{x,y,z\}}$, (d) – next-next-nearest-neighbour correlation functions $\{[\langle\sigma_i^\beta\sigma_{i+3}^\beta\rangle - \langle\sigma_i^\beta\rangle\langle\sigma_{i+3}^\beta\rangle](t)\}_{\beta=\{x,y,z\}}$; Rows (1) – above referenced magnetizations and correlation functions for $\beta = x$, (3) – $\beta = y$, (5) – $\beta = z$; Rows (2) – log plots of the absolute values of the difference of the variational and exact dynamics from row (1) above, (4) – as in row (2) but for results in row (3), (6) – as in row (2) but for results in row (5).

Panels (7a)-(7d): (7a) – variational dynamics for the Rényi-2 entropy $S_2(t)$, (7b) – value over time of the smallest eigenvalue of the variational density matrix, (7c) – Schmidt singular values over time for a single simulation, (7d) – total number of t-VMC+MPO iterations recorded during respective simulations (red) and average time in seconds for a single iteration with standard deviation shown as error bars (blue).

For parameter and hyperparameter values used, see Tables S2 or S3 at the end of this document.

F. Panel descriptions, $N = 50$ and $N = 200$

Variational dynamics of magnetization and pair correlation functions obtained with t-VMC+MPO; Columns (a) – magnetizations $\{\langle\sigma^\beta\rangle(t)\}_{\beta=\{x,y,z\}}$, (b) - nearest-neighbour correlation functions $\{[\langle\sigma_i^\beta\sigma_{i+1}^\beta\rangle - \langle\sigma_i^\beta\rangle\langle\sigma_{i+1}^\beta\rangle](t)\}_{\beta=\{x,y,z\}}$, (c) – next-nearest-neighbour correlation functions $\{[\langle\sigma_i^\beta\sigma_{i+2}^\beta\rangle - \langle\sigma_i^\beta\rangle\langle\sigma_{i+2}^\beta\rangle](t)\}_{\beta=\{x,y,z\}}$, (d) – next-next-nearest-neighbour correlation functions $\{[\langle\sigma_i^\beta\sigma_{i+3}^\beta\rangle - \langle\sigma_i^\beta\rangle\langle\sigma_{i+3}^\beta\rangle](t)\}_{\beta=\{x,y,z\}}$; Rows (1) – above referenced magnetizations and correlation functions for $\beta = x$, (2) – $\beta = y$, (3) – $\beta = z$.

For parameter and hyperparameter values used, see Tables S2 or S3 at the end of this document.

G. Transverse-field Ising model with short-range interactions, $N = 10$

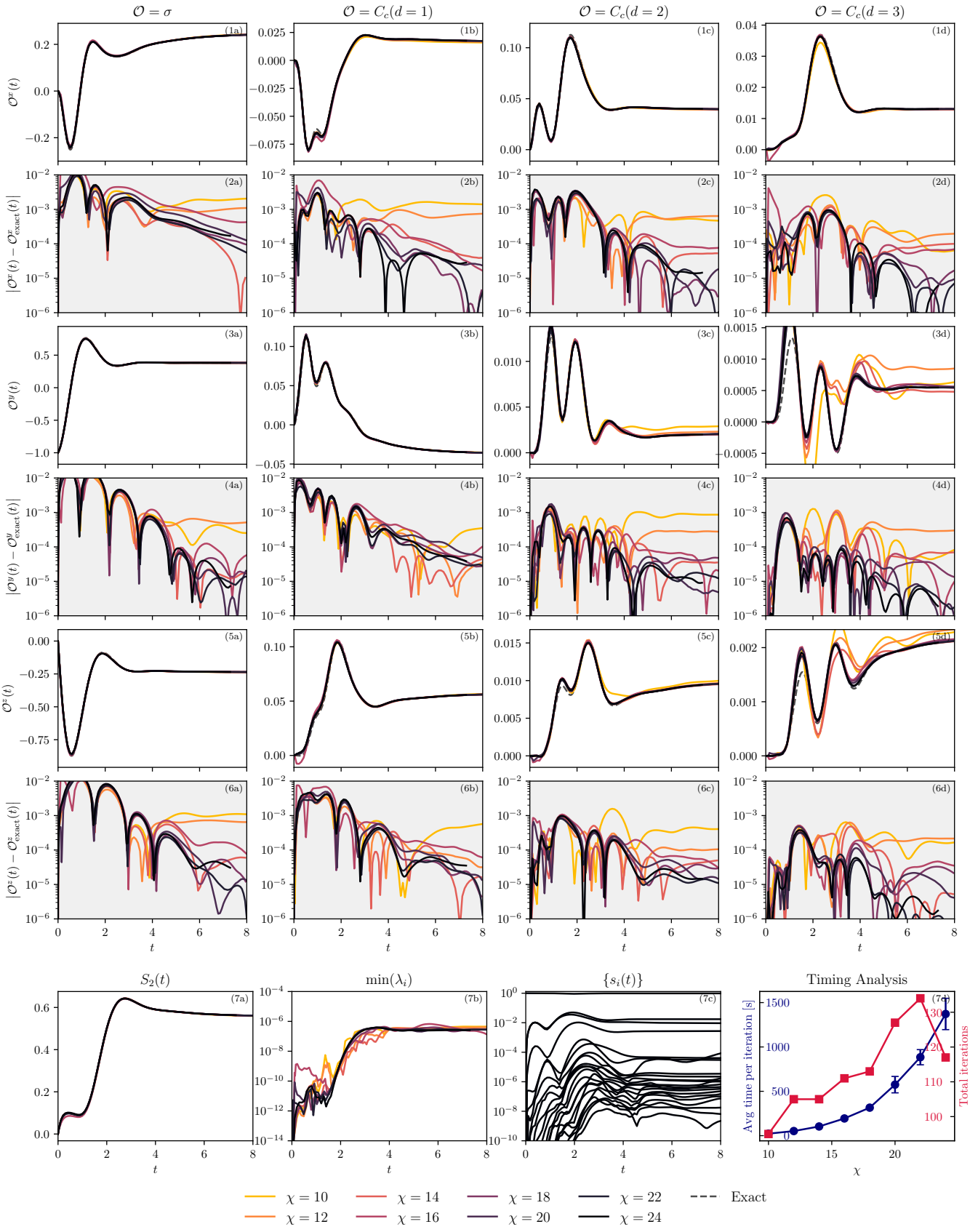

FIG. S2. **Convergence with χ. Transverse-field Ising model with short-range interactions interactions, $N = 10$.** For panel descriptions, see Supplementary Note 2 E.

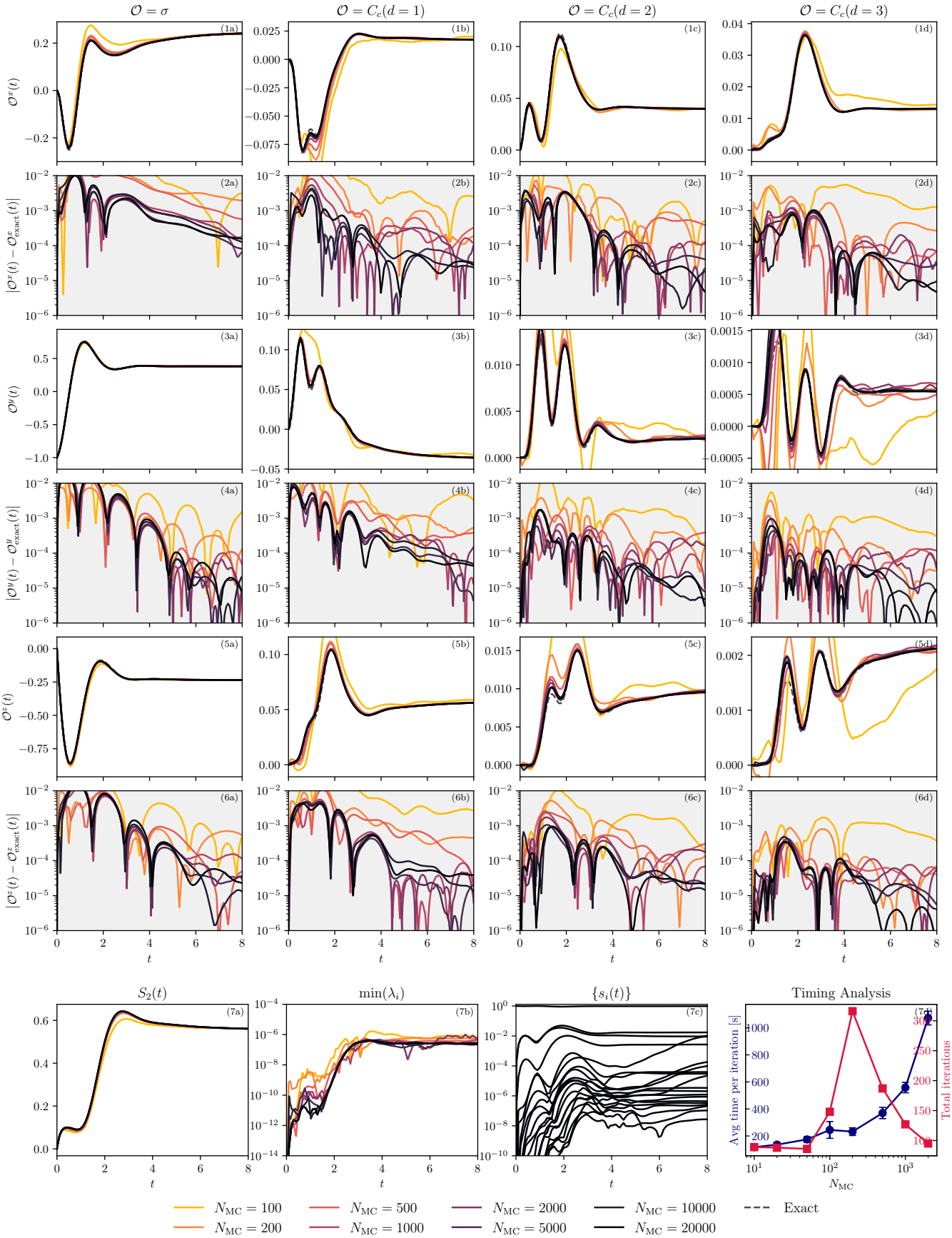

FIG. S3. **Convergence with N_{MC}. Transverse-field Ising model with short-range interactions, $N = 10$.** For panel descriptions, see Supplementary Note 2 E.

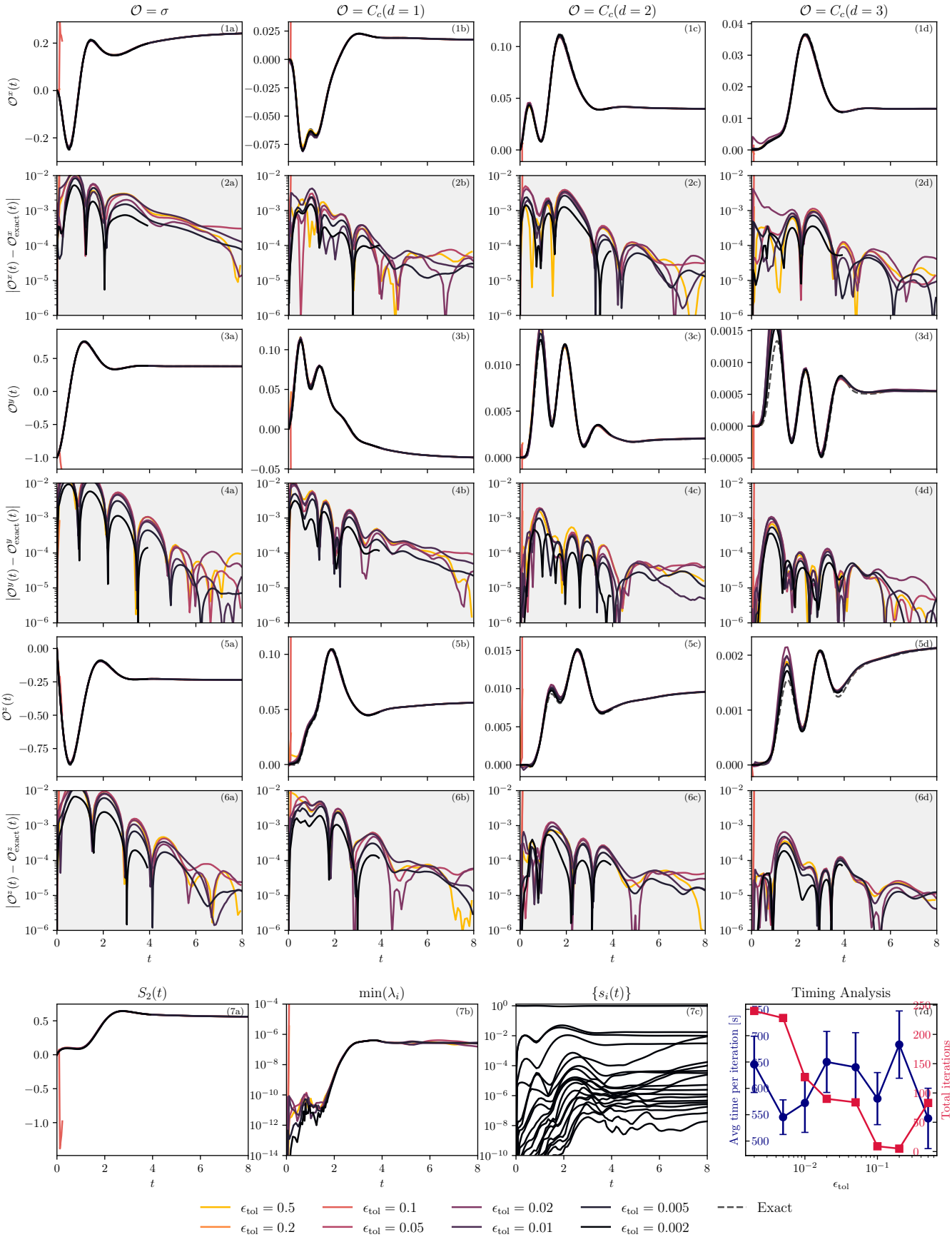

FIG. S4. **Convergence with ϵ_{tol}. Transverse-field Ising model with short-range interactions, $N = 10$.** For panel descriptions, see Supplementary Note 2 E.

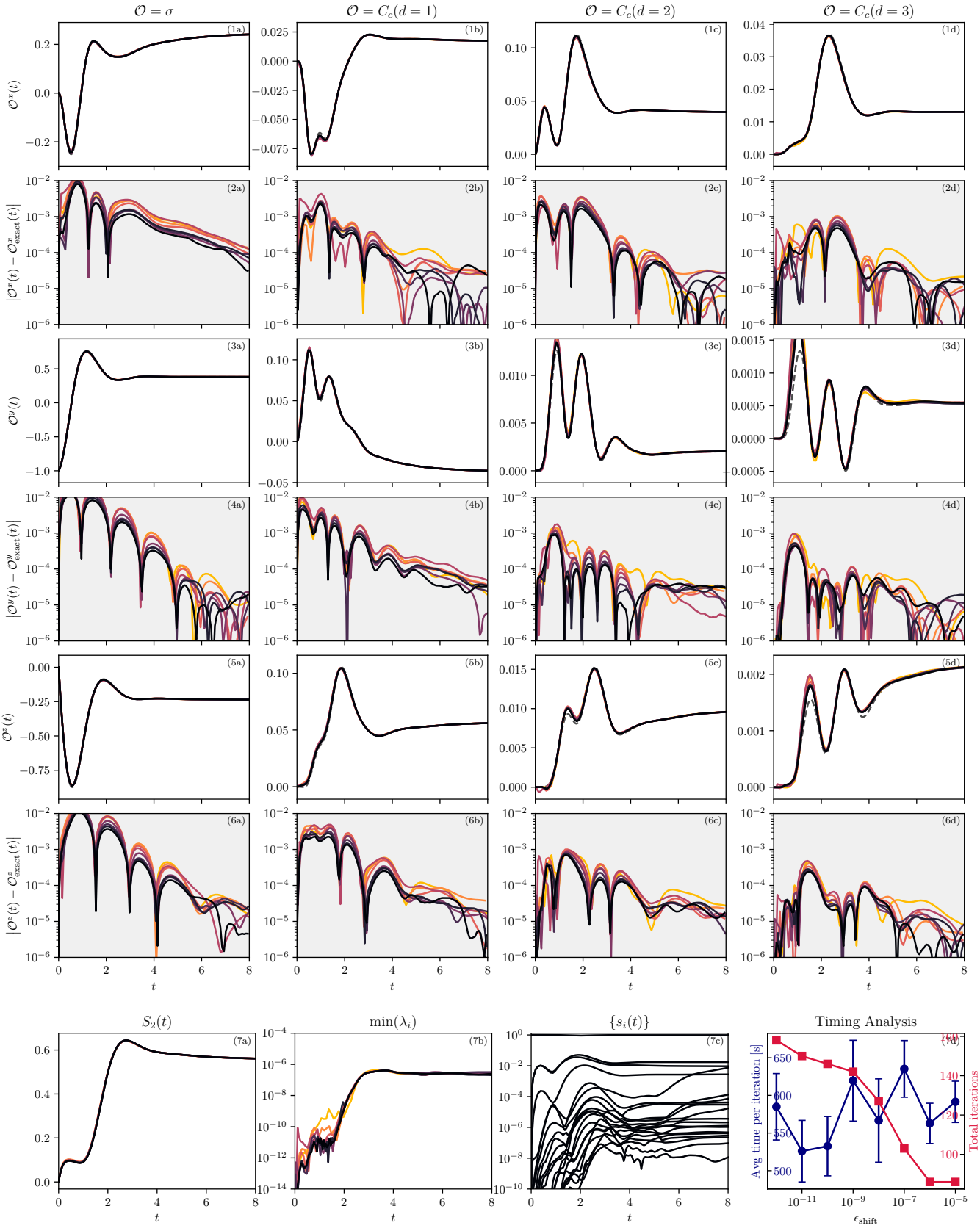

FIG. S5. **Convergence with ϵ_{shift}. Transverse-field Ising model with short-range interactions,** $N = 10$**.** For panel descriptions, see Supplementary Note 2 E.

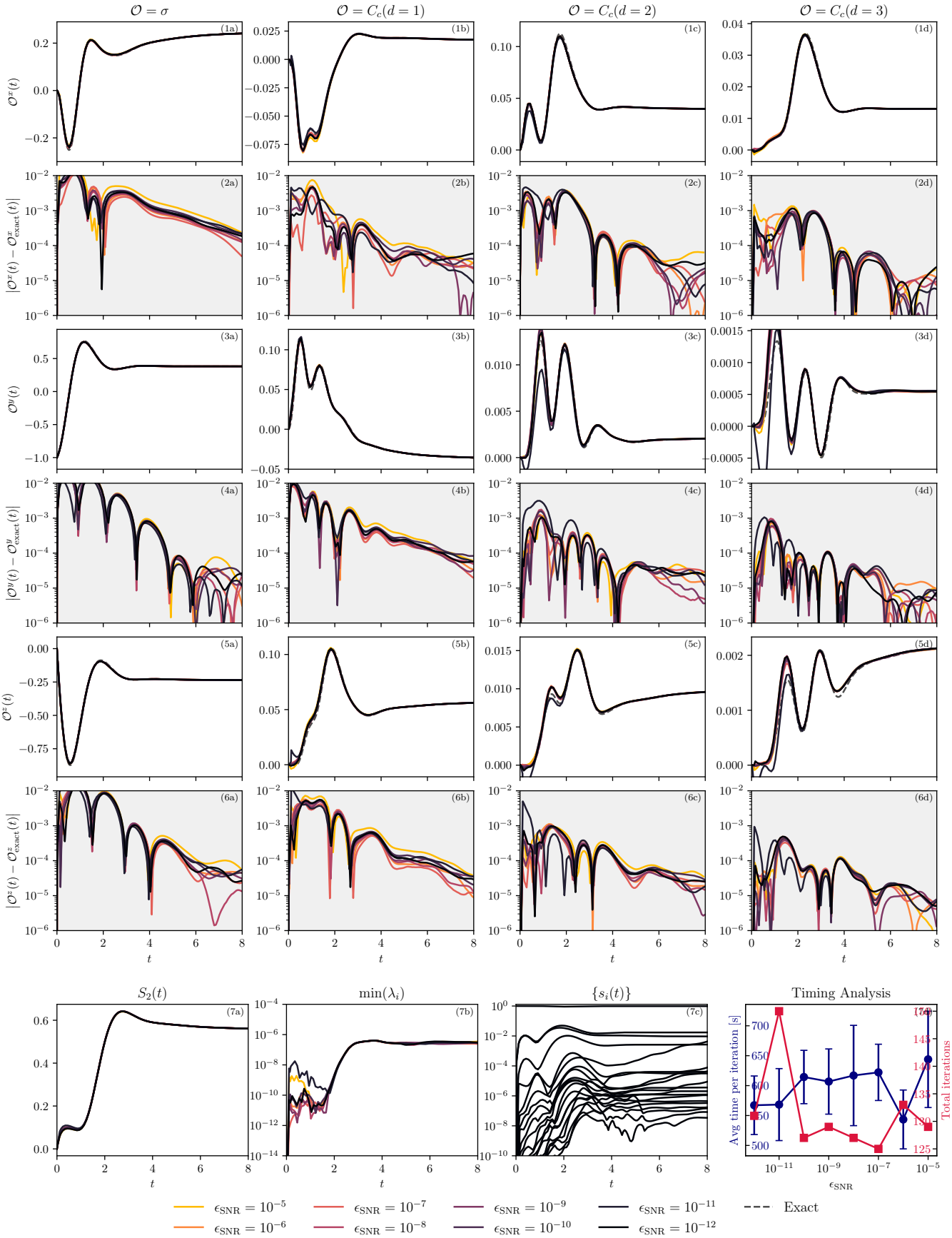

FIG. S6. **Convergence with ϵ_{SNR}. Transverse-field Ising model with short-range interactions,** $N = 10$**.** For panel descriptions, see Supplementary Note 2 E.

H. Transverse-field Ising model with short-range interactions, $N = 200$

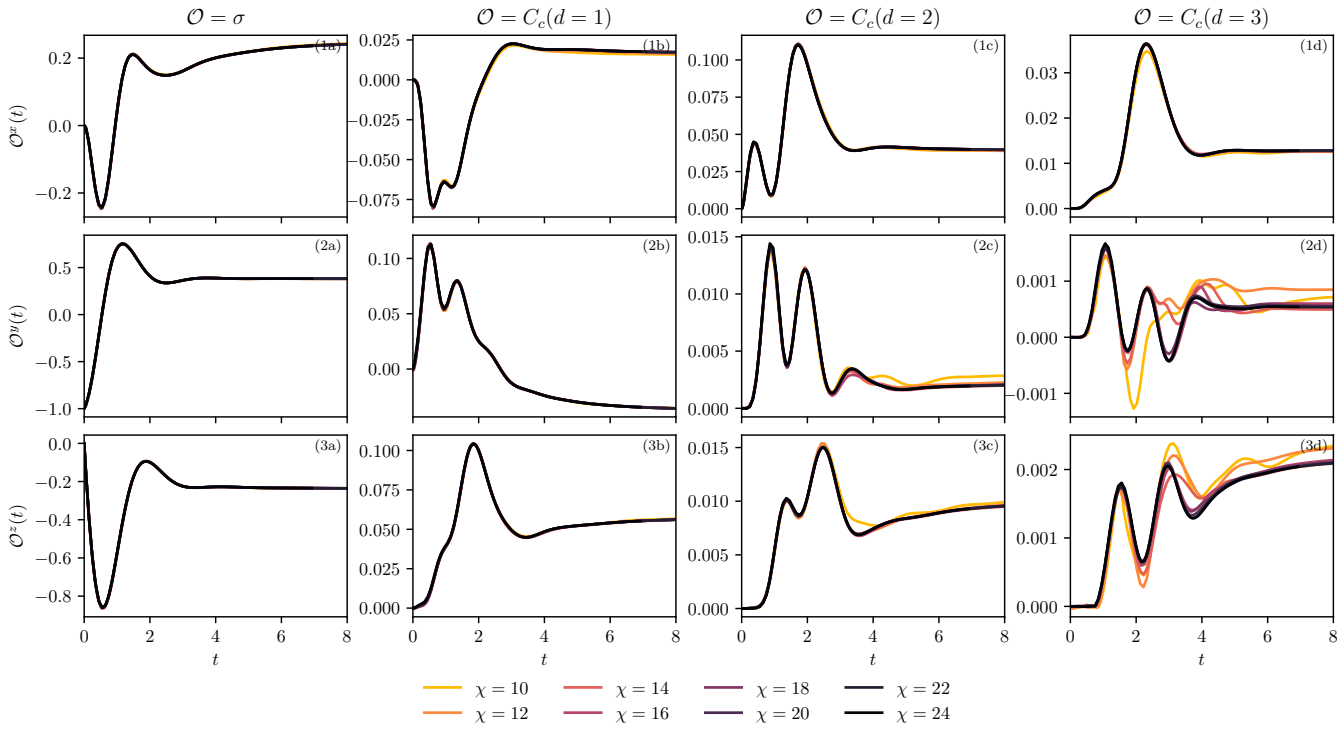

FIG. S7. **Convergence with χ. Transverse-field Ising model with short-range interactions interactions, $N = 200$.** For panel descriptions, see Supplementary Note 2 F.

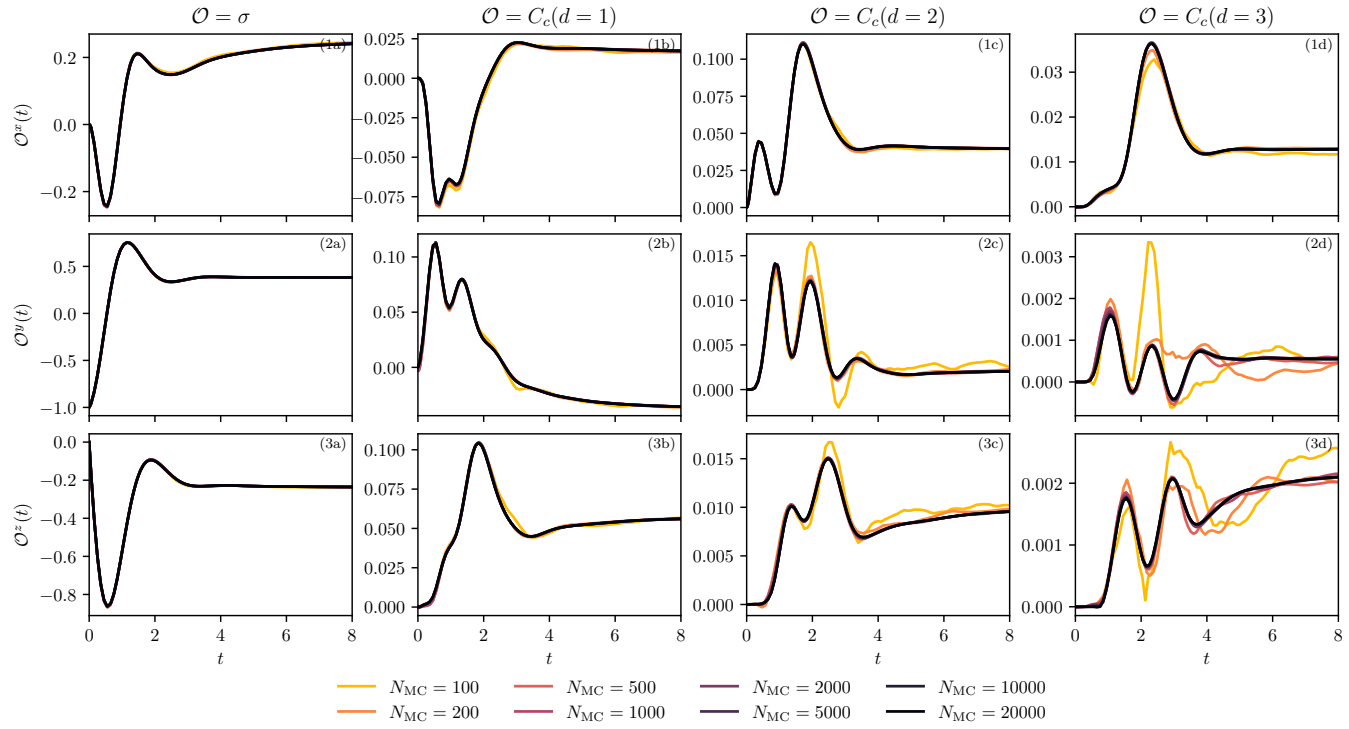

FIG. S8. **Convergence with N_{MC}. Transverse-field Ising model with short-range interactions,** $N = 200$**.** For panel descriptions, see Supplementary Note 2 F.

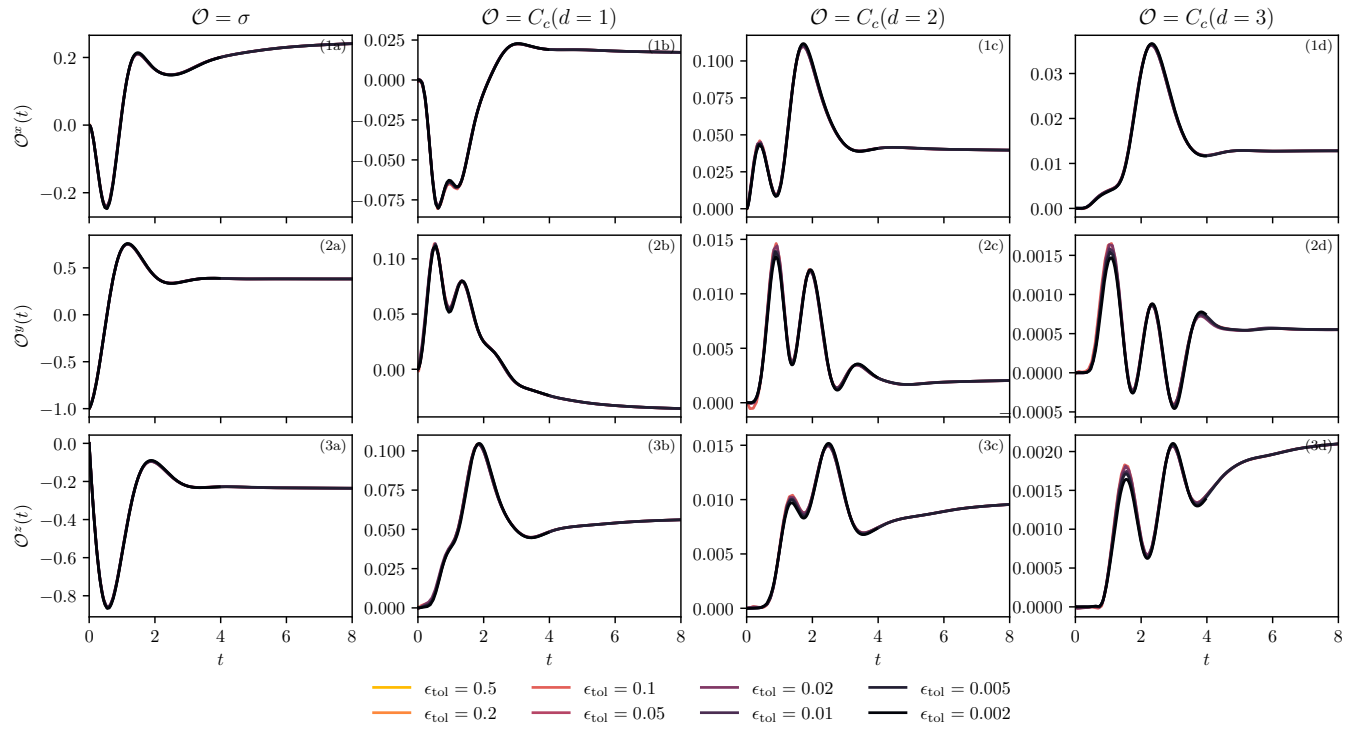

FIG. S9. **Convergence with ϵ_{tol}. Transverse-field Ising model with short-range interactions,** $N = 200$**.** For panel descriptions, see Supplementary Note 2 F.

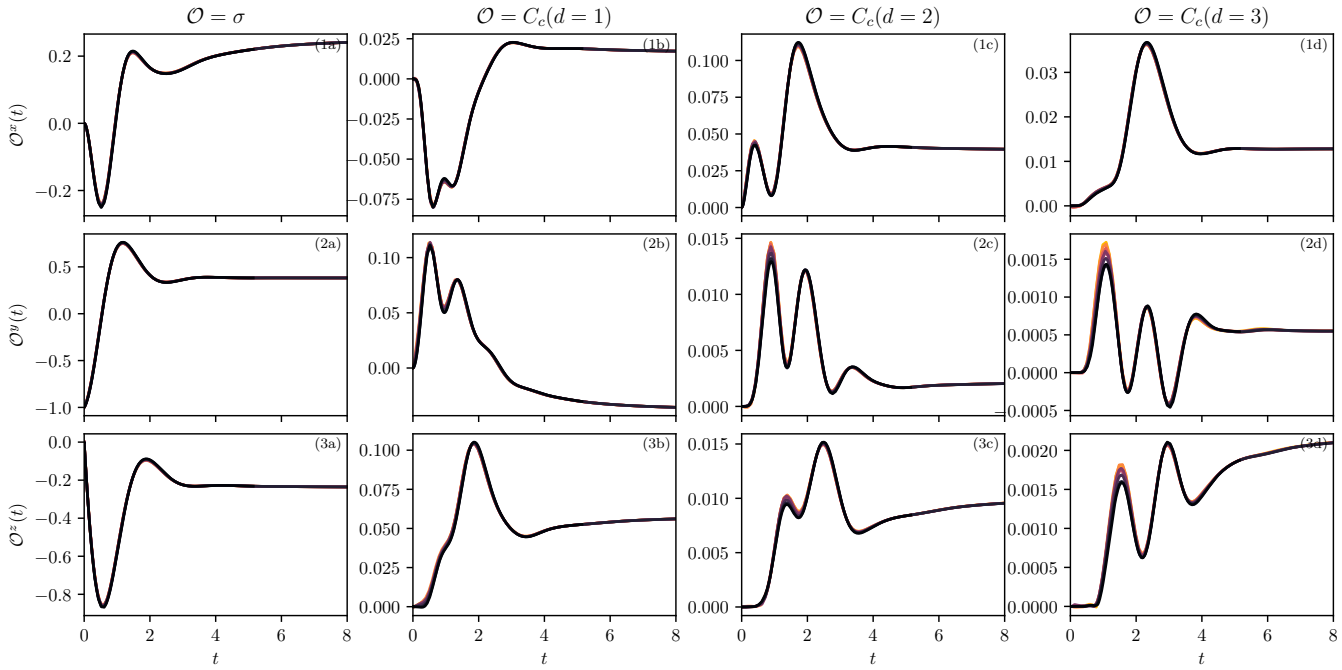

FIG. S10. **Convergence with ϵ_{shift}. Transverse-field Ising model with short-range interactions,** $N = 200$**.** For panel descriptions, see Supplementary Note 2 F.

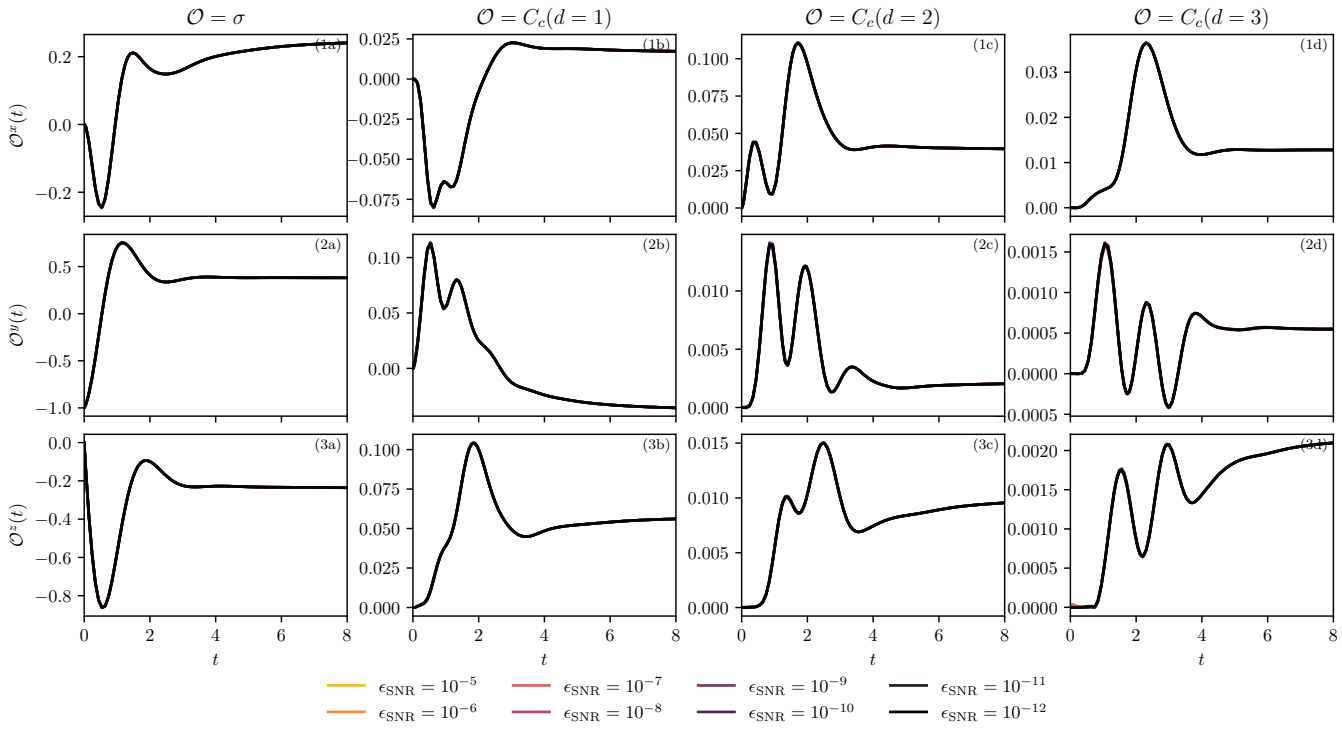

FIG. S11. **Convergence with ϵ_{SNR}. Transverse-field Ising model with short-range interactions,** $N = 200$**.** For panel descriptions, see Supplementary Note 2 F.

I. Transverse-field Ising model with weak long-range competing interactions, $N = 10$

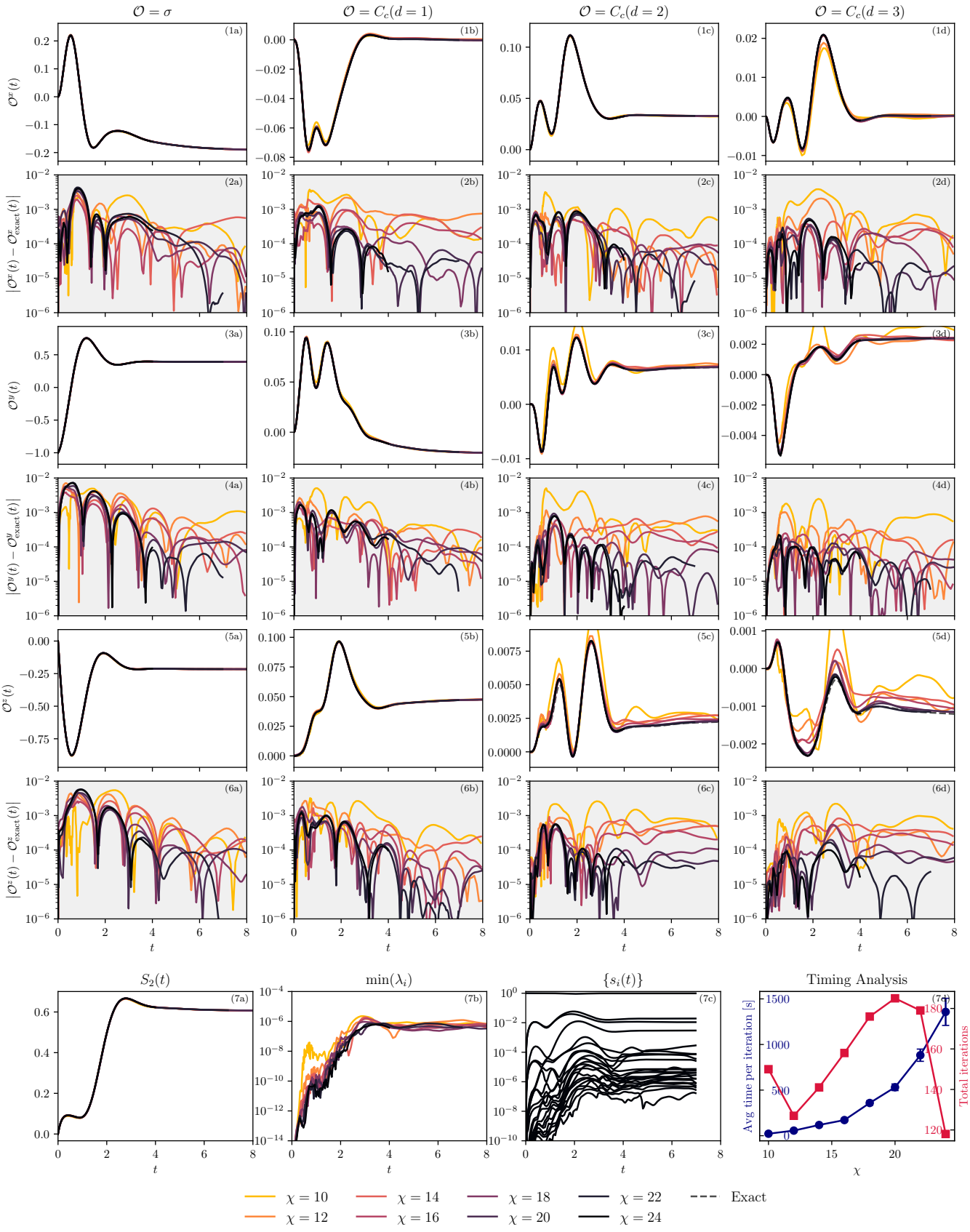

FIG. S12. **Convergence with χ. Transverse-field Ising model with weak long-range competing interactions, $N = 10$.** For panel descriptions, see Supplementary Note 2 E.

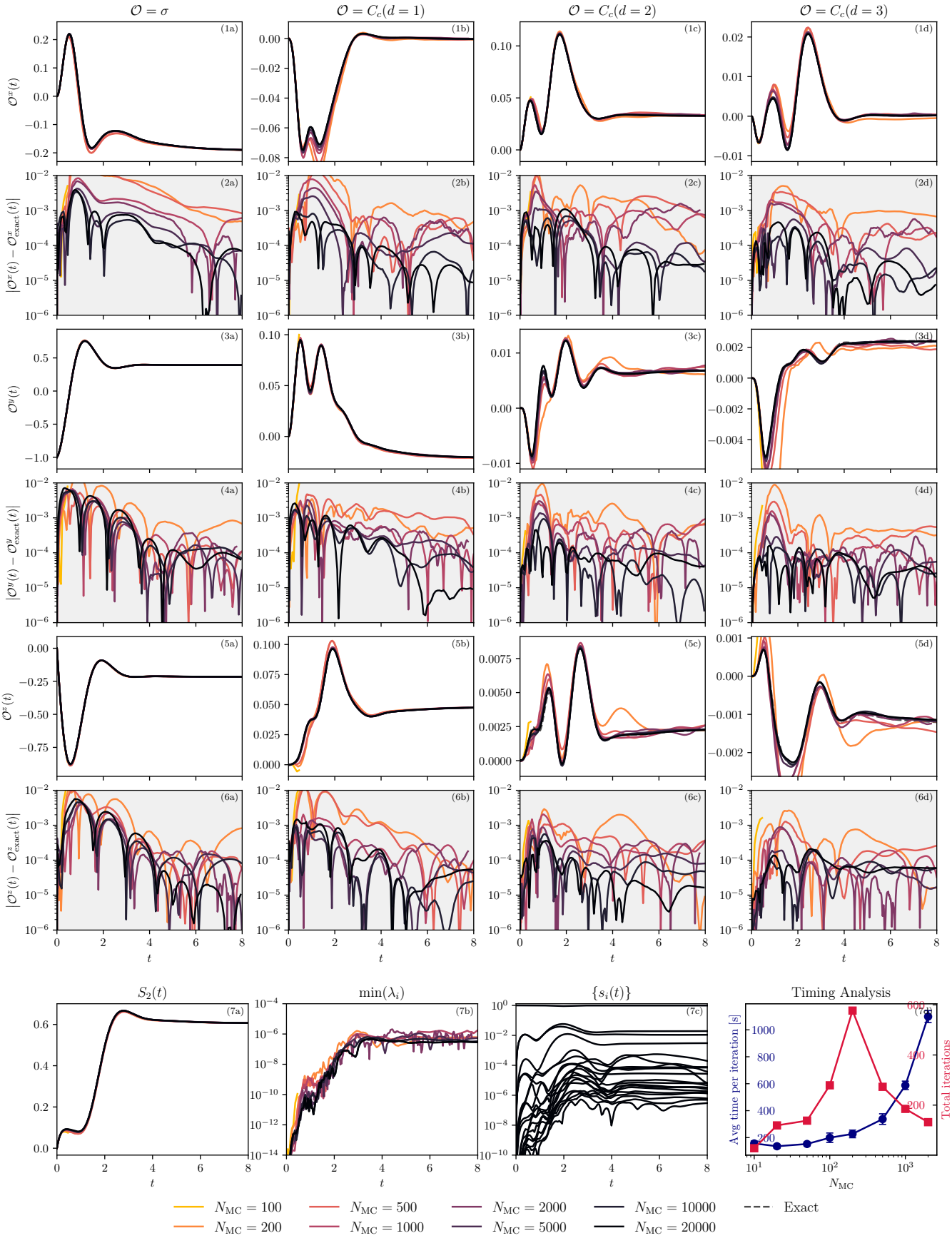

FIG. S13. **Convergence with N_{MC}. Transverse-field Ising model with weak long-range competing interactions, $N = 10$.** For panel descriptions, see Supplementary Note 2 E.

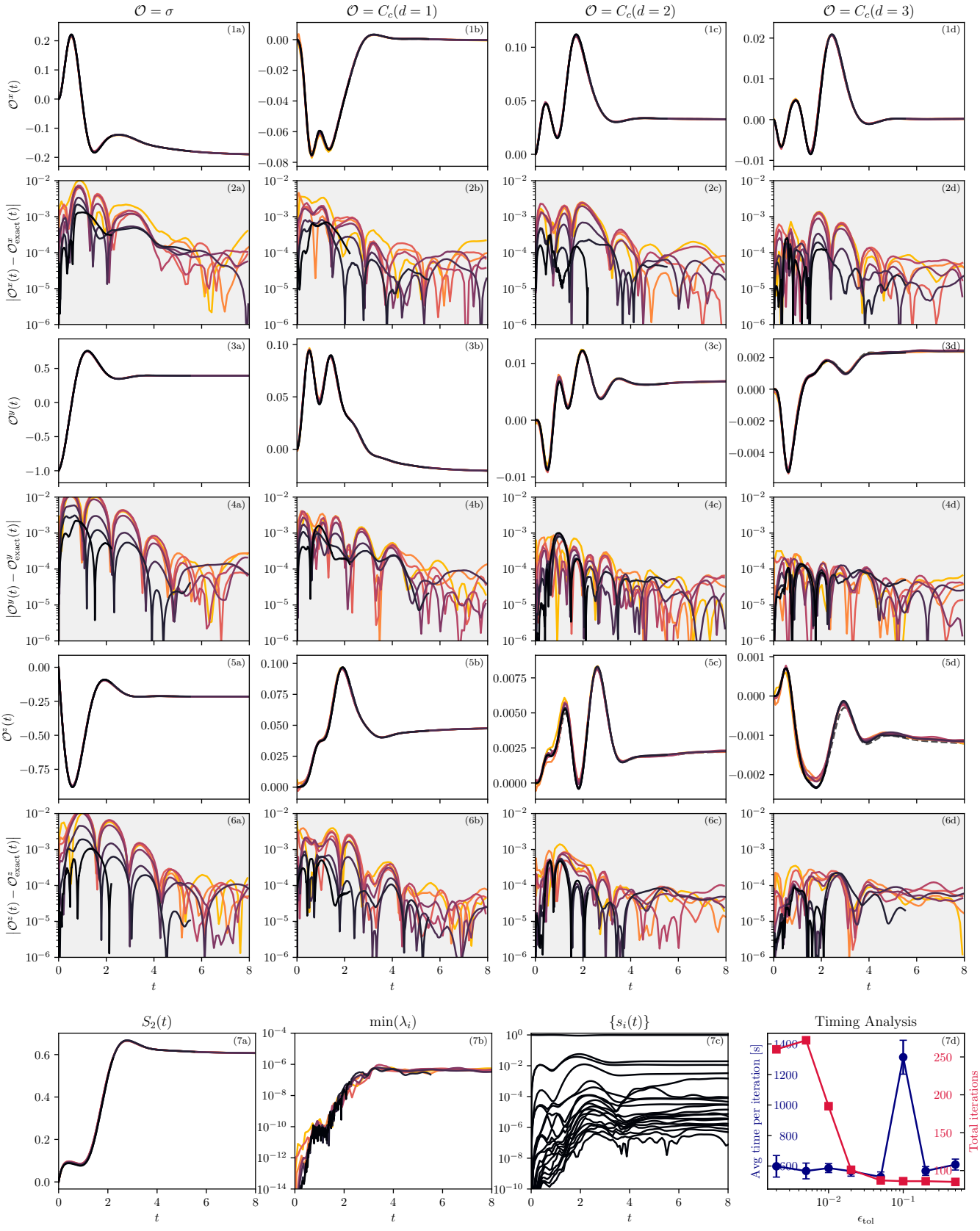

FIG. S14. **Convergence with ϵ_{tol}. Transverse-field Ising model with weak long-range competing interactions, $N = 10$.** For panel descriptions, see Supplementary Note 2 E.

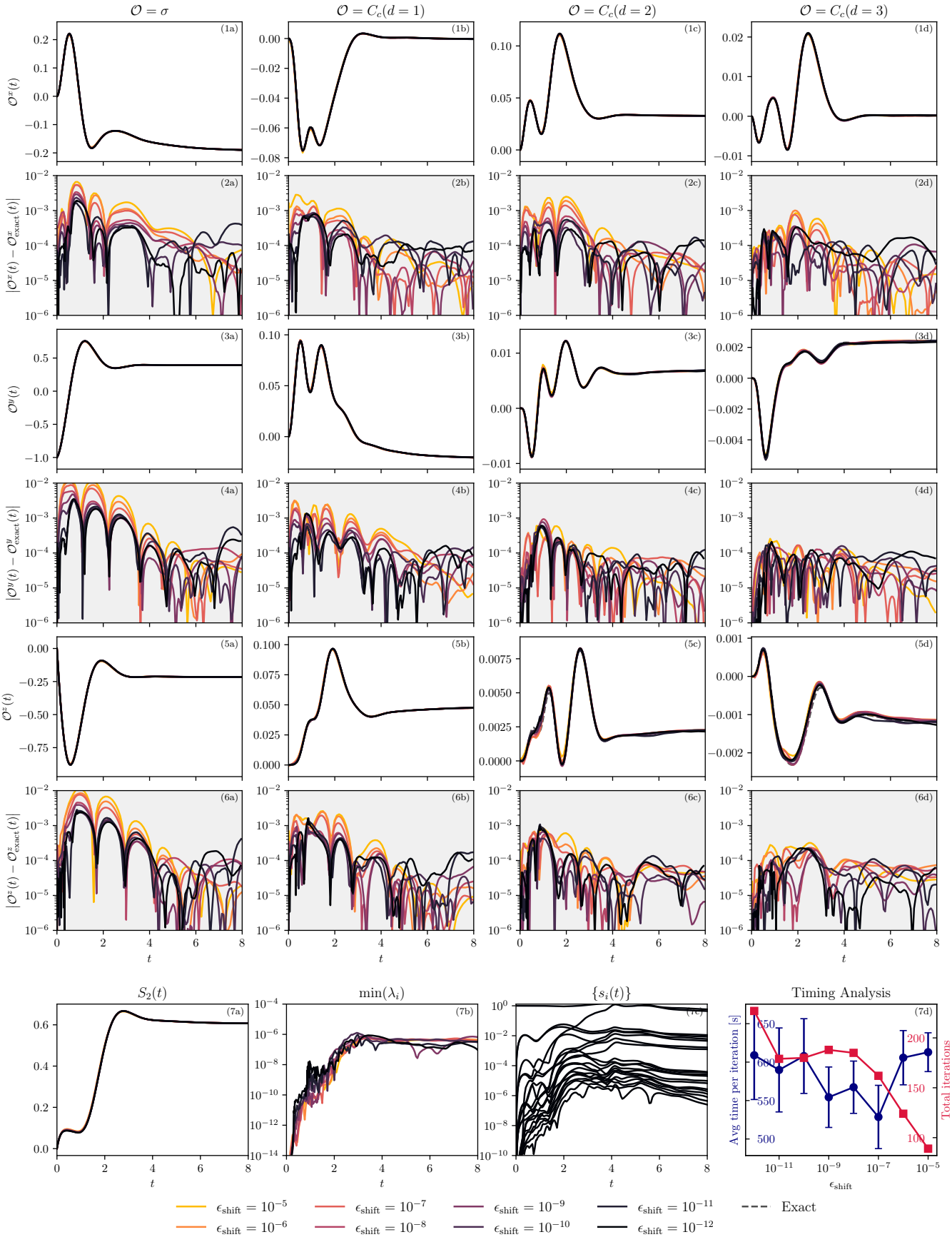

FIG. S15. **Convergence with ϵ_{shift}. Transverse-field Ising model with weak long-range competing interactions, $N = 10$.** For panel descriptions, see Supplementary Note 2 E.

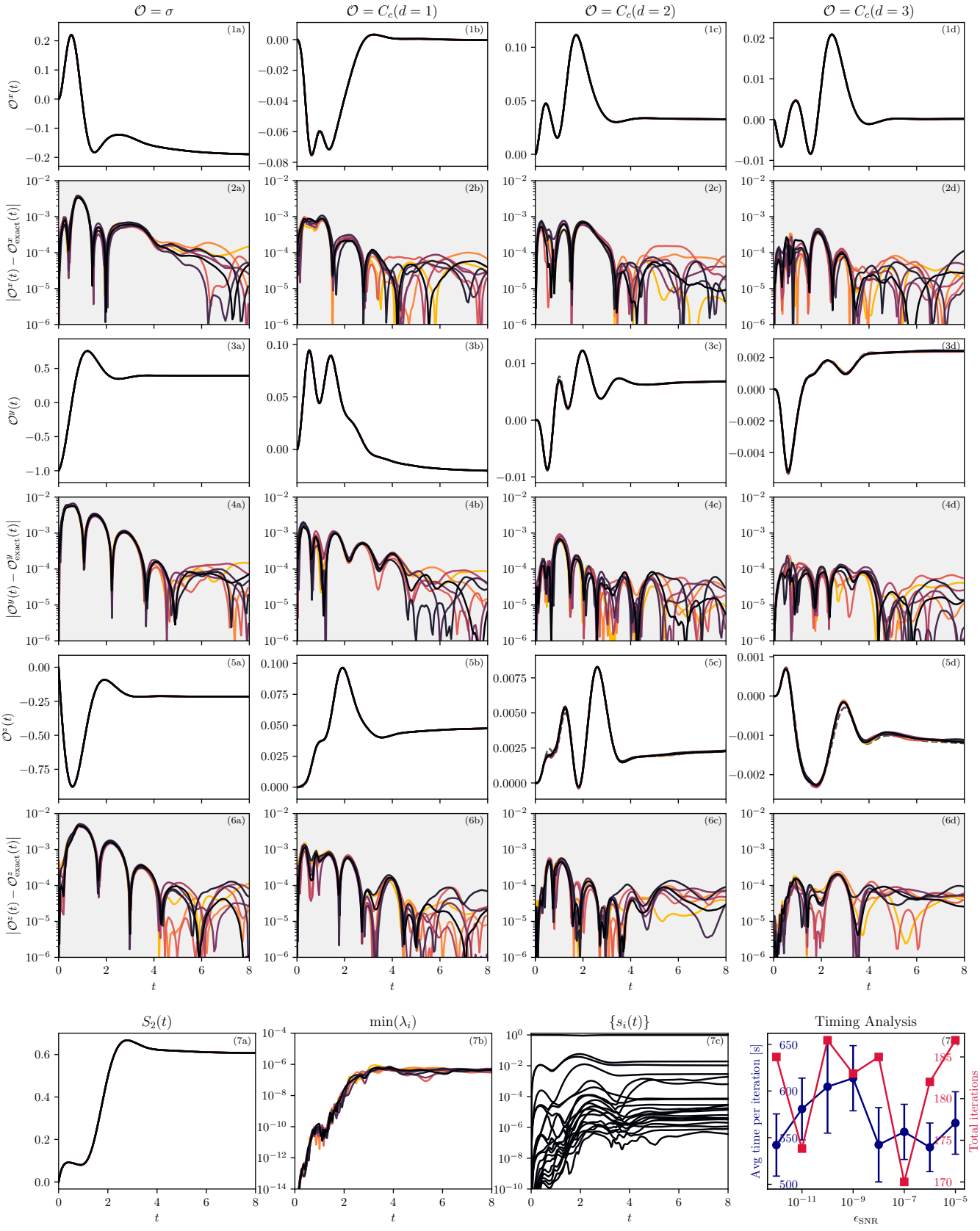

FIG. S16. **Convergence with ϵ_{SNR}. Transverse-field Ising model with weak long-range competing interactions, $N = 10$.** For panel descriptions, see Supplementary Note 2 E.

J. Transverse-field Ising model with weak long-range competing interactions, $N = 200$

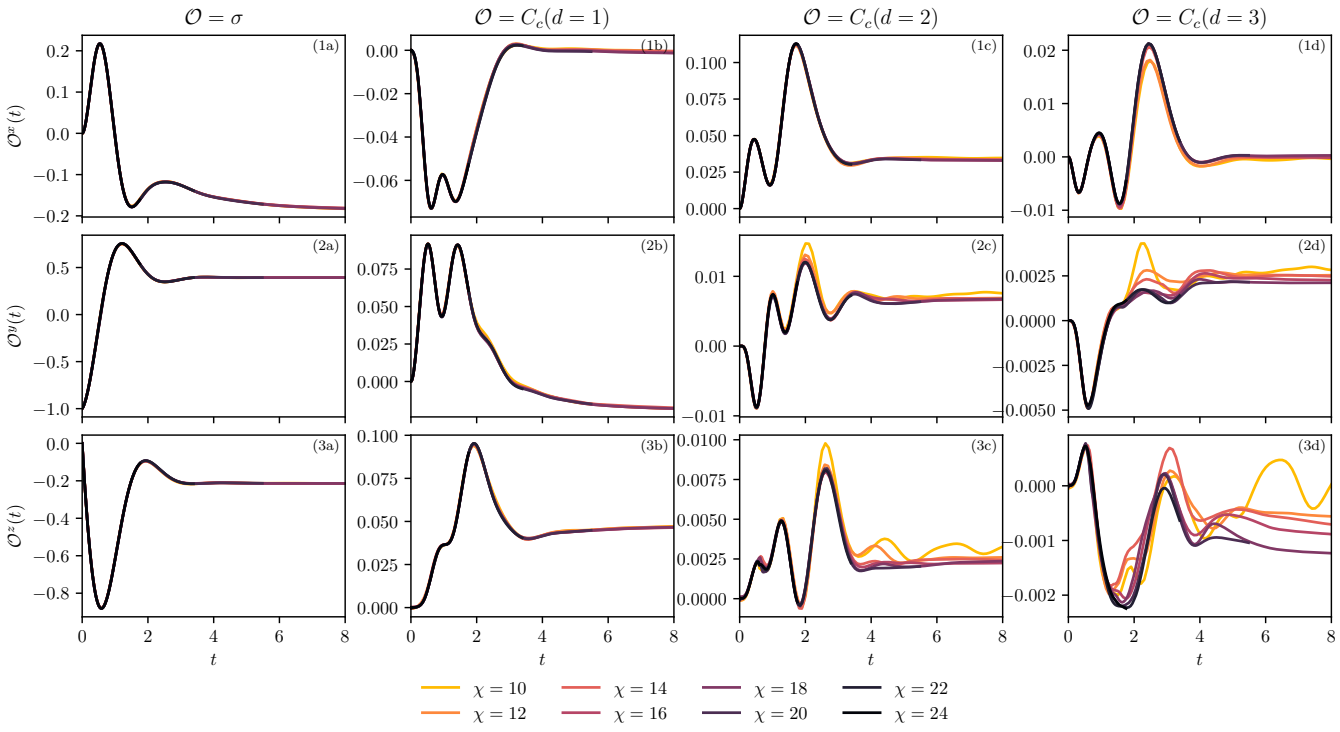

FIG. S17. **Convergence with χ. Transverse-field Ising model with weak long-range competing interactions, $N = 200$.** For panel descriptions, see Supplementary Note 2 F.

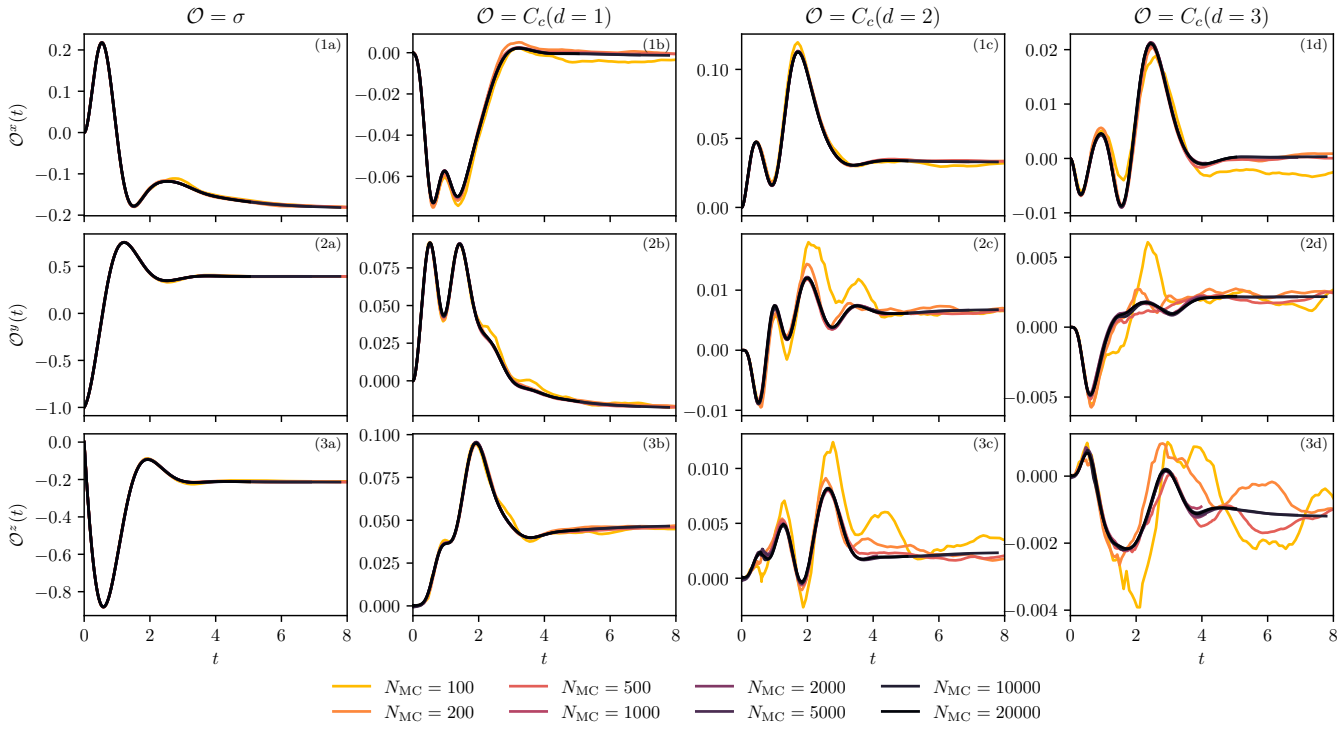

FIG. S18. **Convergence with N_{MC}. Transverse-field Ising model with weak long-range competing interactions, $N = 200$.** For panel descriptions, see Supplementary Note 2 F.

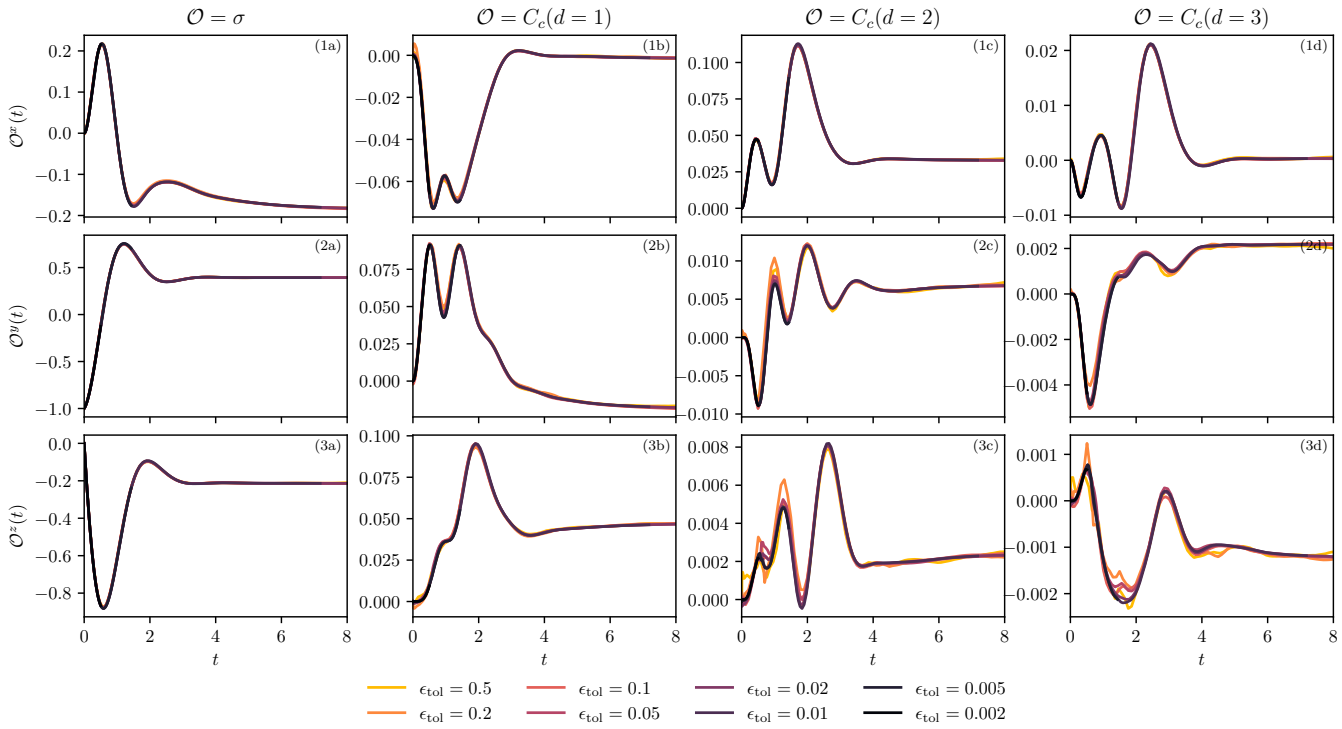

FIG. S19. **Convergence with $\epsilon_{\mathbf{tol}}$. Transverse-field Ising model with weak long-range competing interactions, $N = 200$.** For panel descriptions, see Supplementary Note 2 F.

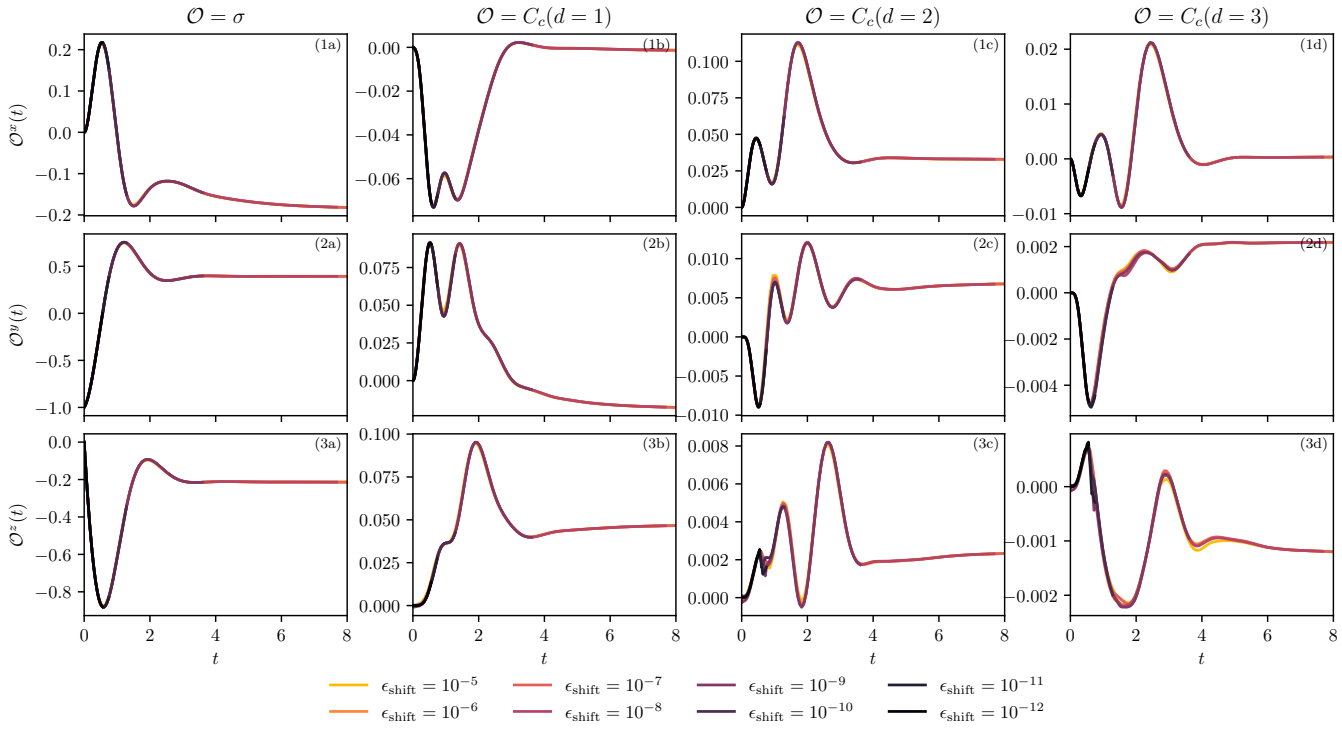

FIG. S20. **Convergence with ϵ_{shift}. Transverse-field Ising model with weak long-range competing interactions, $N = 200$.** For panel descriptions, see Supplementary Note 2 F.

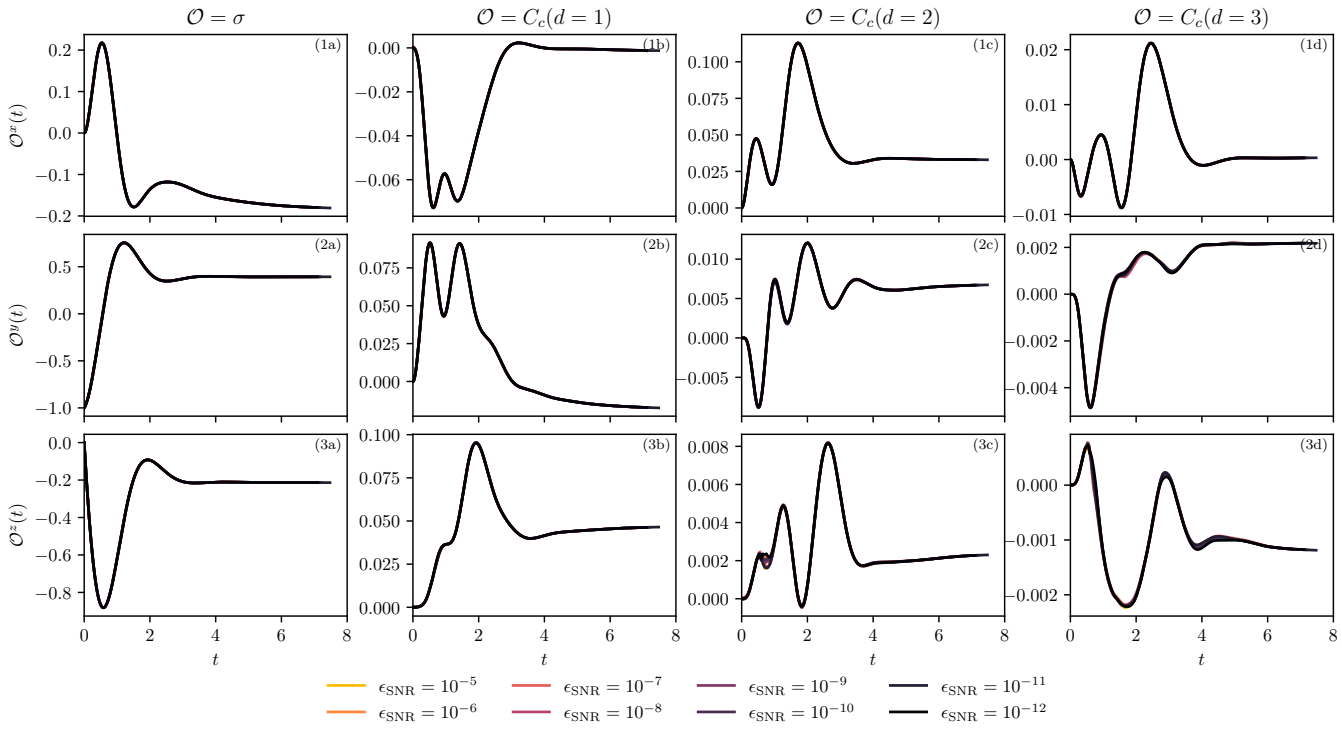

FIG. S21. **Convergence with ϵ_{SNR}. Transverse-field Ising model with weak long-range competing interactions, $N = 200$.** For panel descriptions, see Supplementary Note 2 F.

K. Transverse-field Ising model with strong long-range competing interactions, $N = 10$

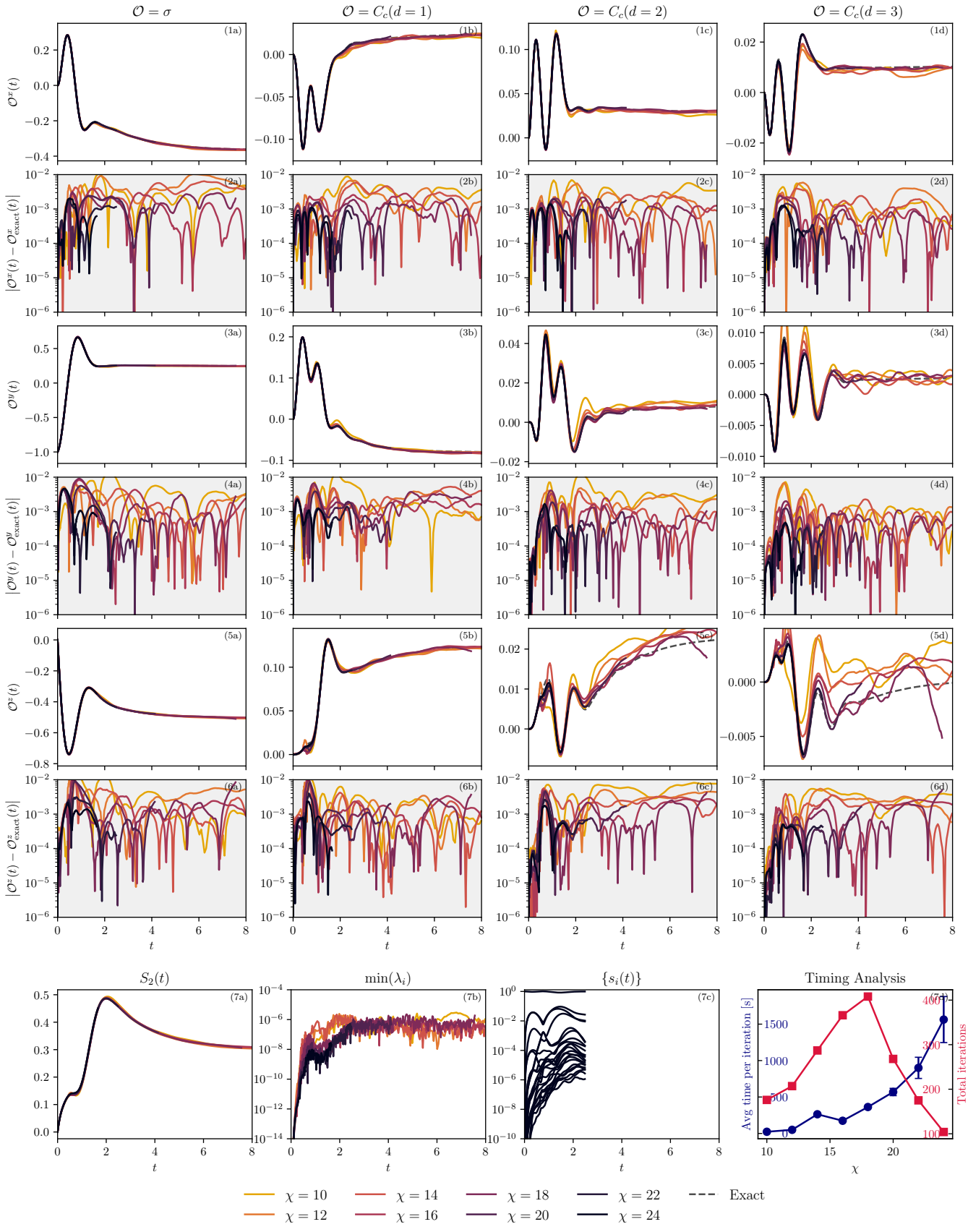

FIG. S22. **Convergence with χ. Transverse-field Ising model with strong long-range competing interactions, $N = 10$.** For panel descriptions, see Supplementary Note 2 E.

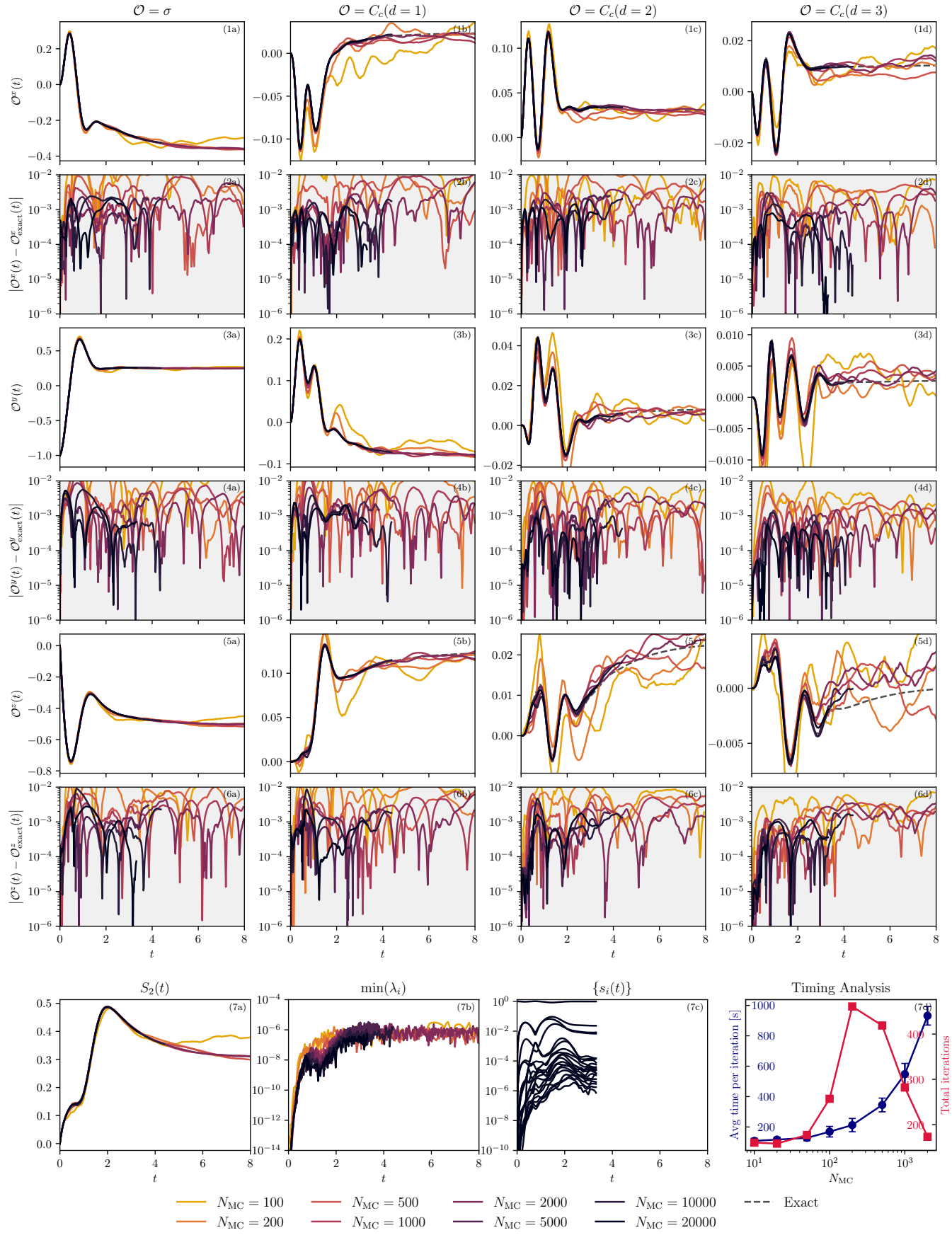

FIG. S23. **Convergence with N_{MC}. Transverse-field Ising model with strong long-range competing interactions, $N = 10$.** For panel descriptions, see Supplementary Note 2 E.

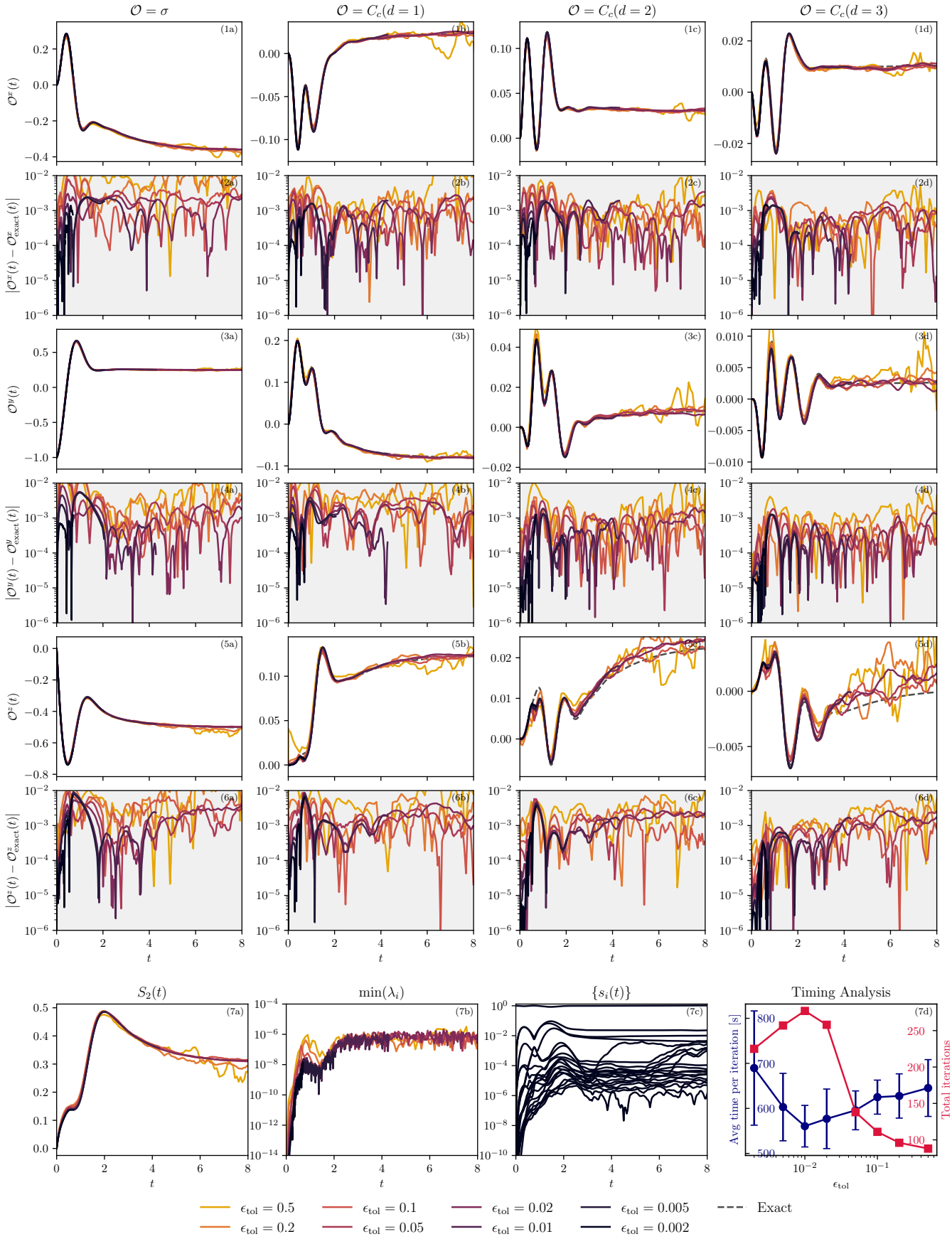

FIG. S24. **Convergence with ϵ_{tol}. Transverse-field Ising model with strong long-range competing interactions, $N = 10$.** For panel descriptions, see Supplementary Note 2 E.

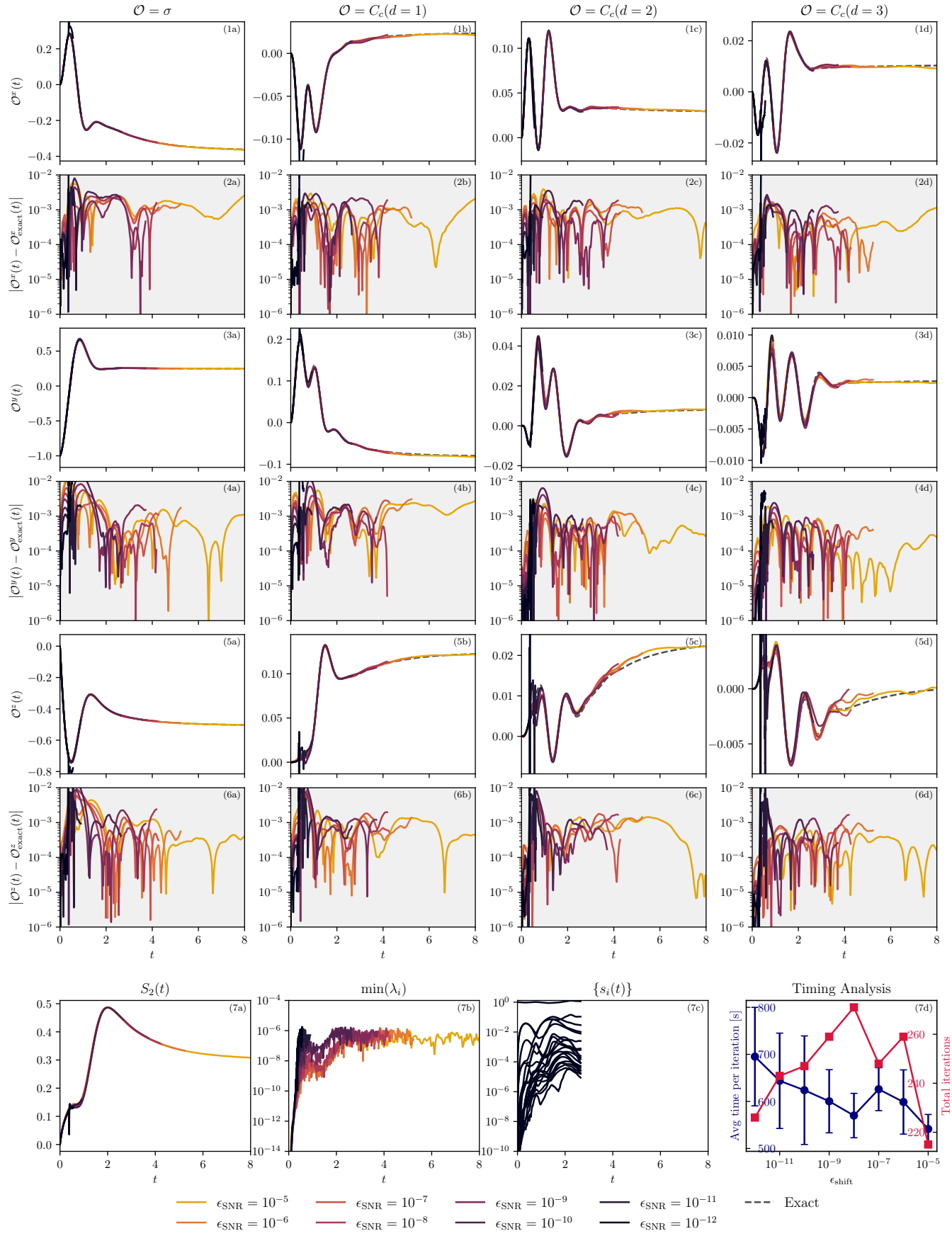

FIG. S25. **Convergence with ϵ_{shift}. Transverse-field Ising model with strong long-range competing interactions, $N = 10$.** For panel descriptions, see Supplementary Note 2 E.

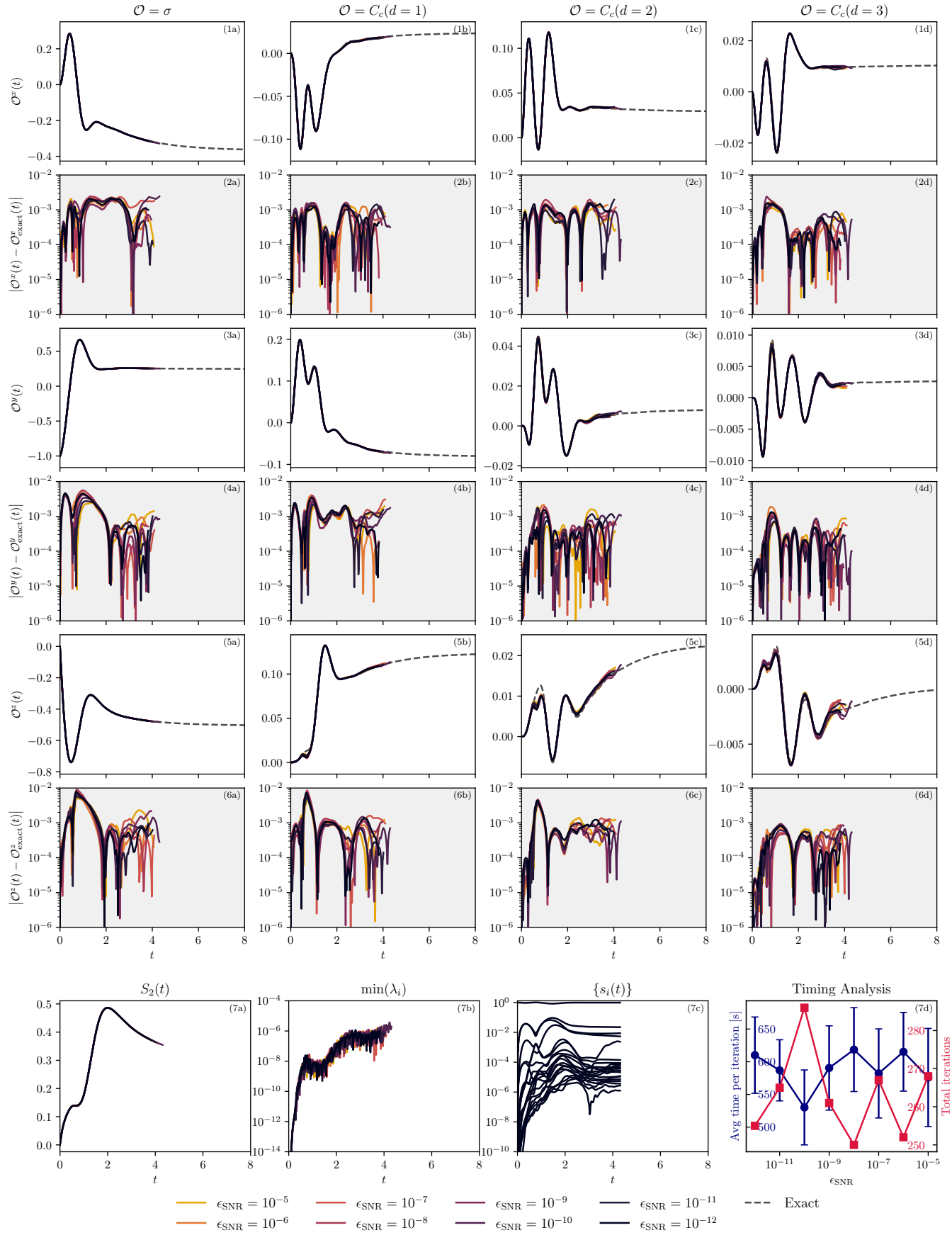

FIG. S26. **Convergence with ϵ_{SNR}. Transverse-field Ising model with strong long-range competing interactions, $N = 10$.** For panel descriptions, see Supplementary Note 2 E.

L. Transverse-field Ising model with strong long-range competing interactions, $N = 200$

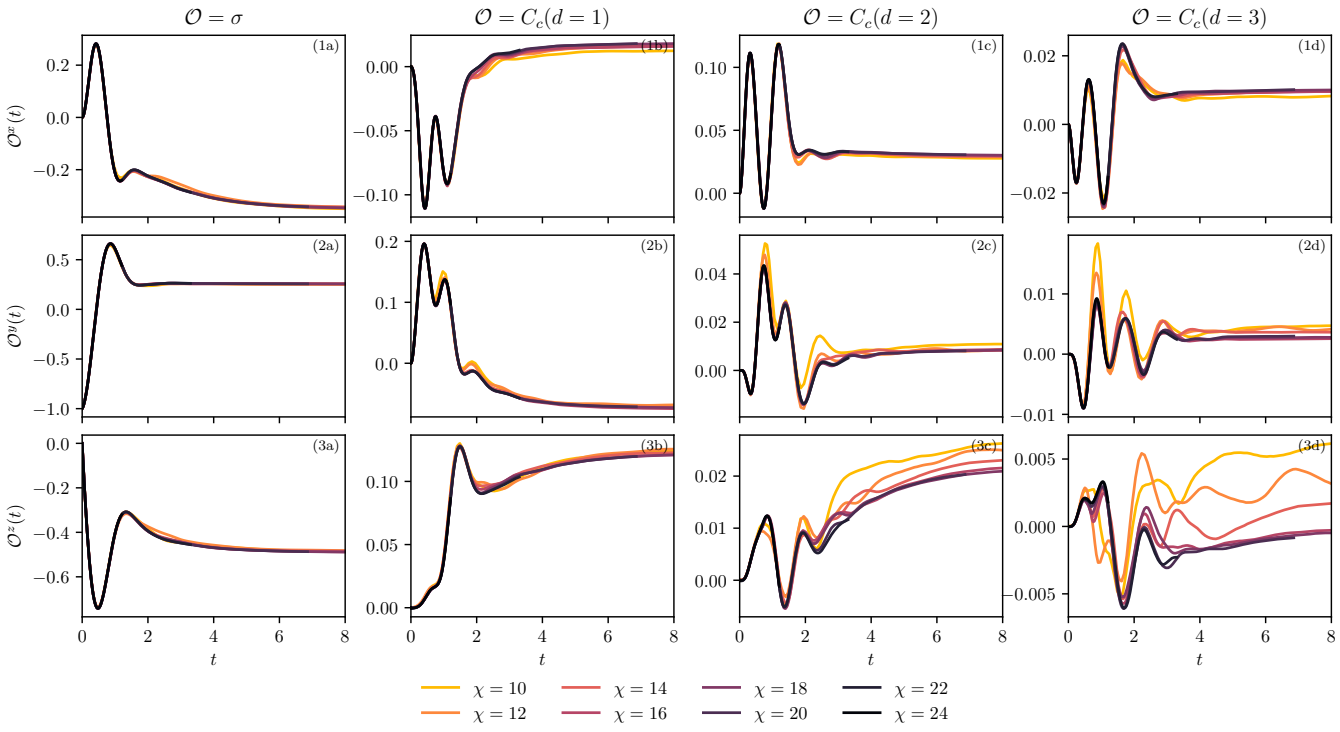

FIG. S27. **Convergence with χ. Transverse-field Ising model with strong long-range competing interactions, $N = 200$.** For panel descriptions, see Supplementary Note 2 F.

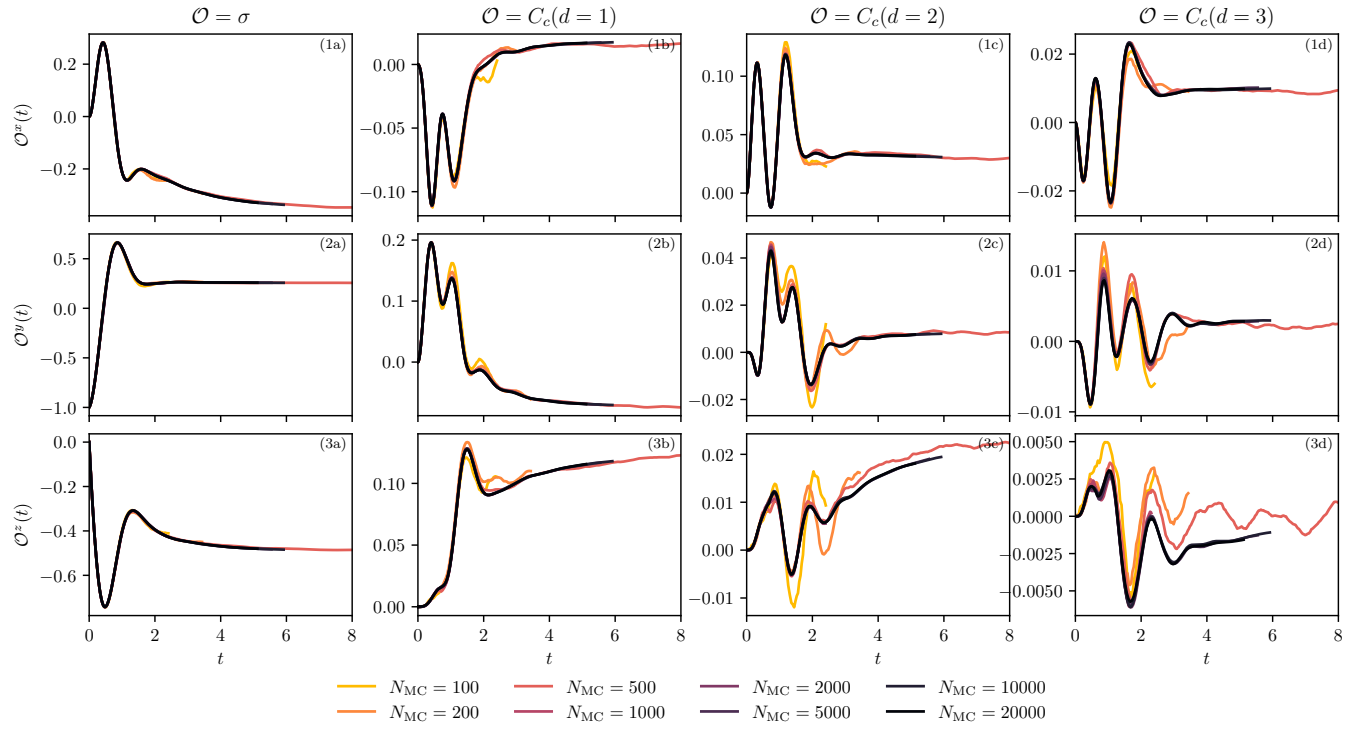

FIG. S28. **Convergence with N_{MC}. Transverse-field Ising model with strong long-range competing interactions, $N = 200$.** For panel descriptions, see Supplementary Note 2 F.

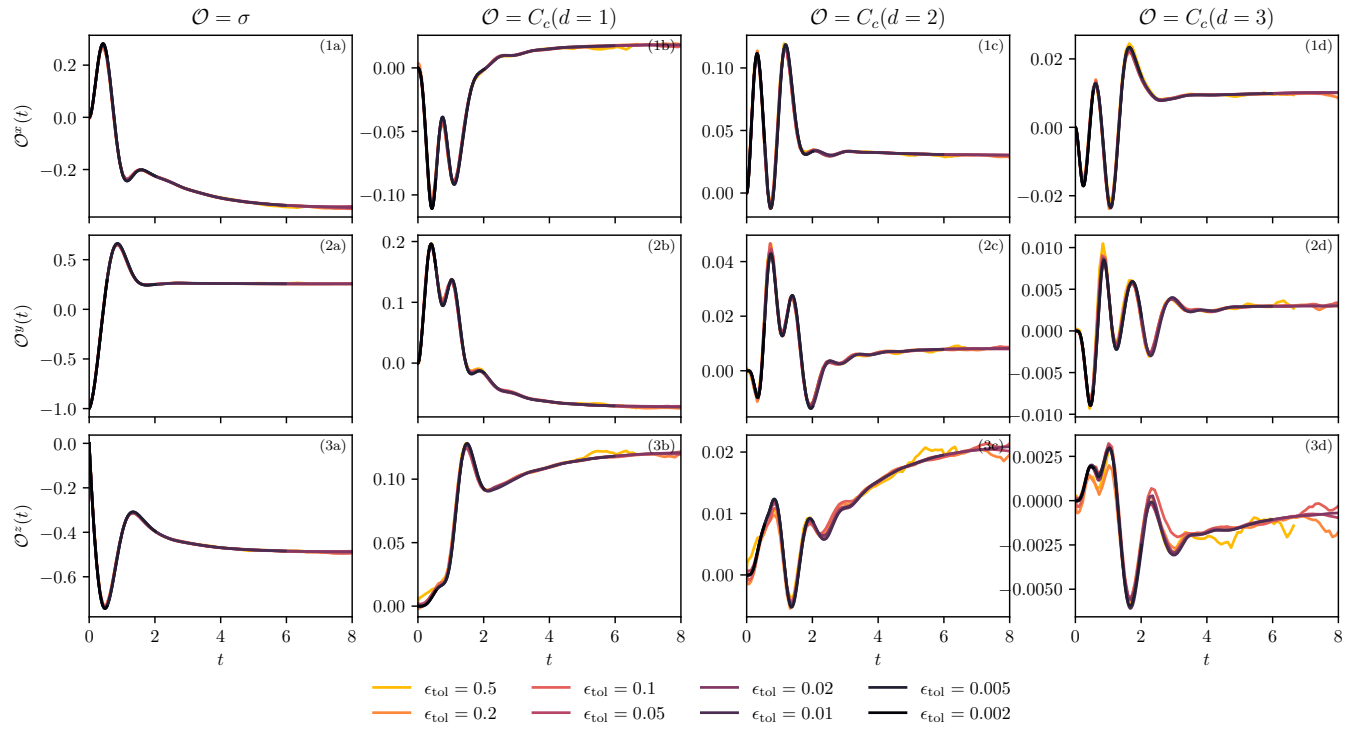

FIG. S29. **Convergence with ϵ_{tol}. Transverse-field Ising model with strong long-range competing interactions, $N = 200$.** For panel descriptions, see Supplementary Note 2 F.

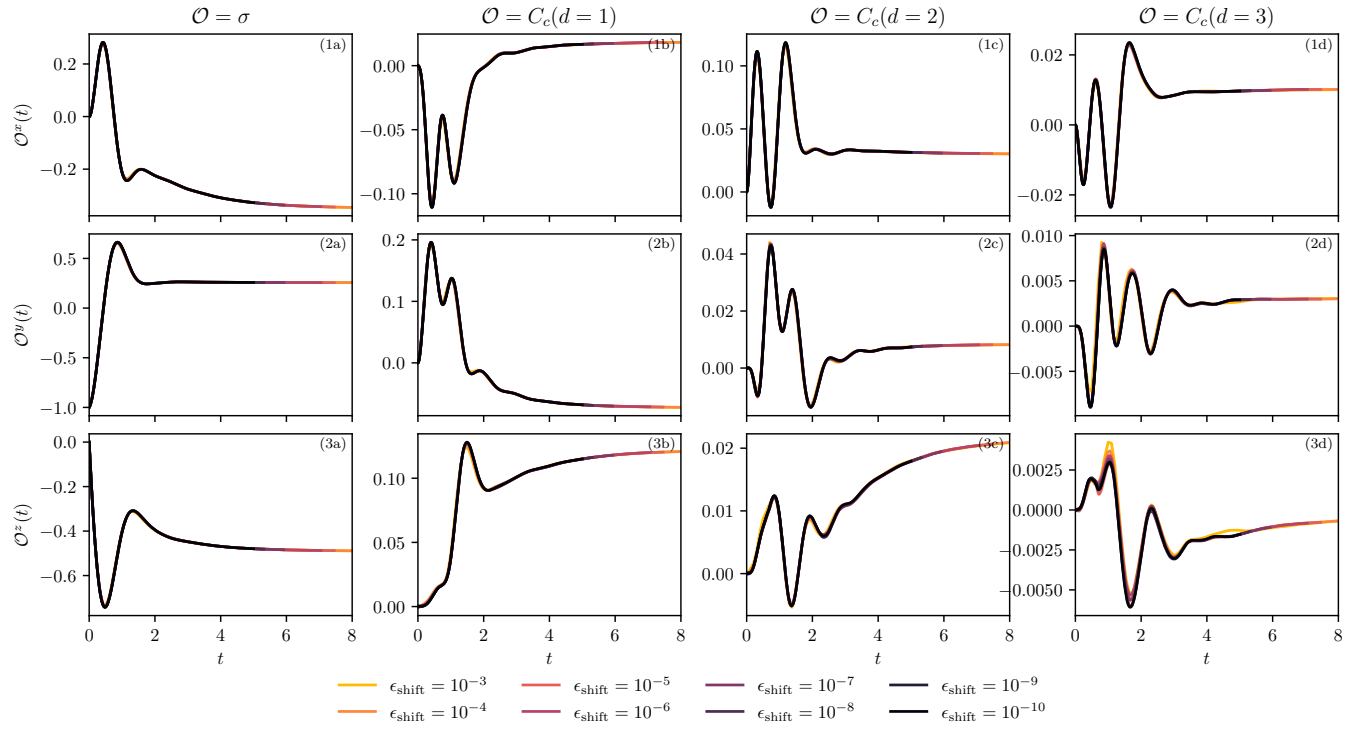

FIG. S30. **Convergence with ϵ_{shift}. Transverse-field Ising model with strong long-range competing interactions, $N = 200$.** For panel descriptions, see Supplementary Note 2 F.

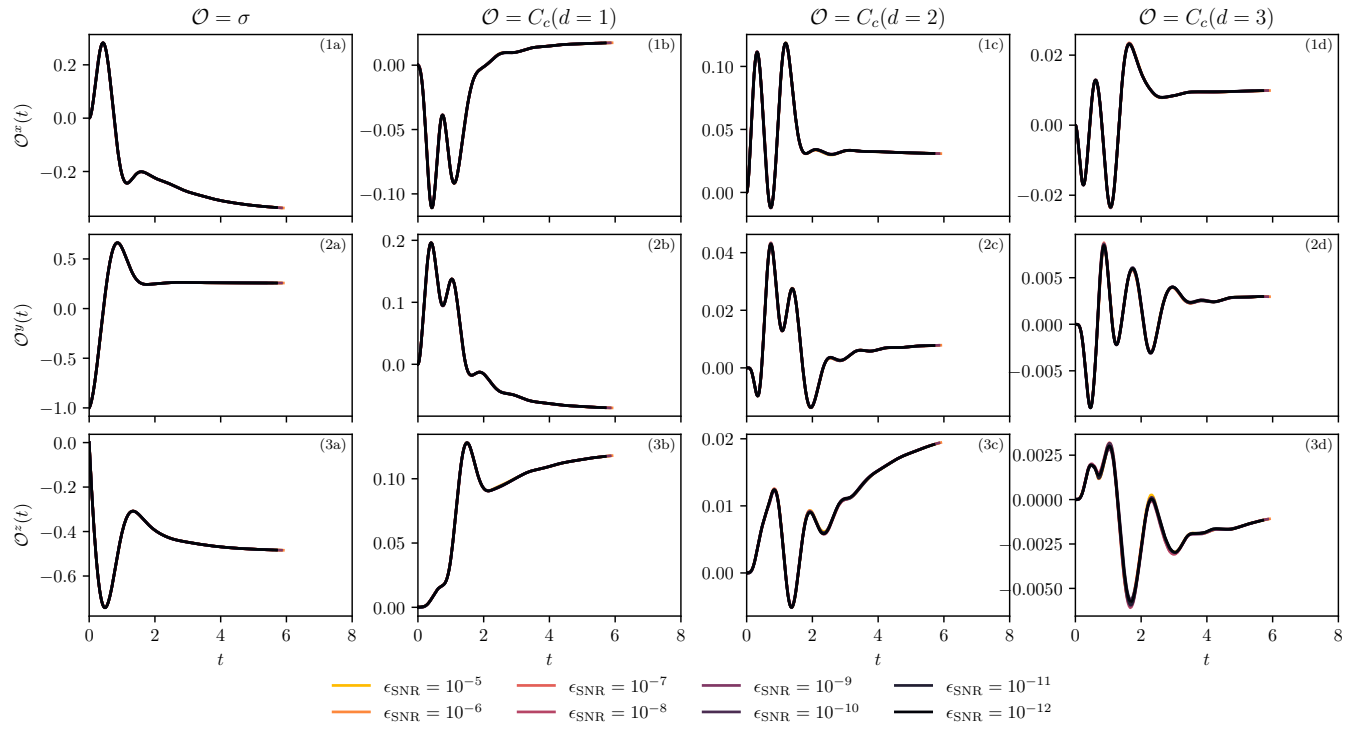

FIG. S31. **Convergence with ϵ_{SNR}. Transverse-field Ising model with strong long-range competing interactions, $N = 200$.** For panel descriptions, see Supplementary Note 2 F.

M. Transverse-field Ising model with super-long-range competing interactions, $N = 10$

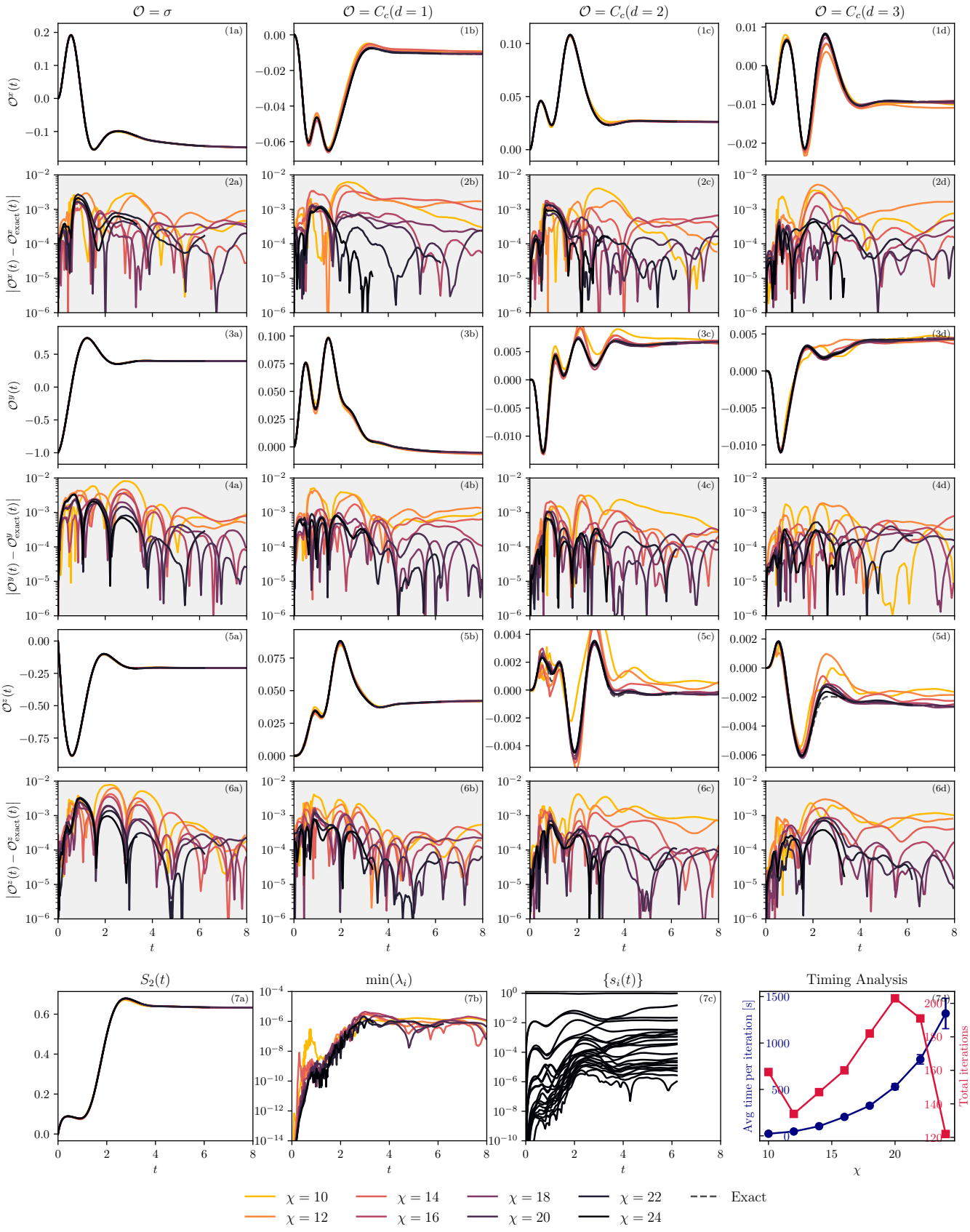

FIG. S32. **Convergence with χ. Transverse-field Ising model with super-long-range competing interactions, $N = 10$.** For panel descriptions, see Supplementary Note 2 E.

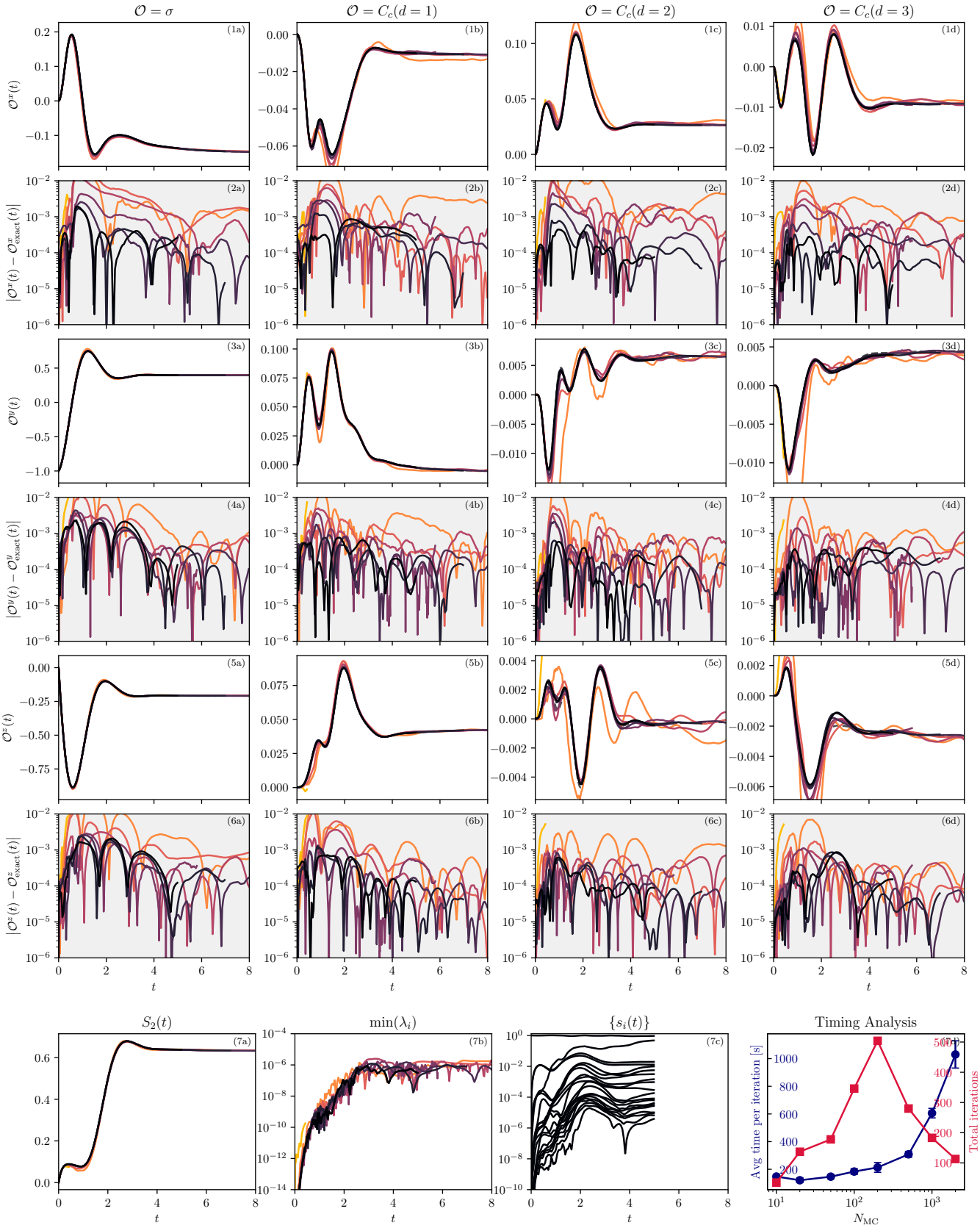

FIG. S33. **Convergence with N_{MC}. Transverse-field Ising model with super-long-range competing interactions, $N = 10$.** For panel descriptions, see Supplementary Note 2 E.

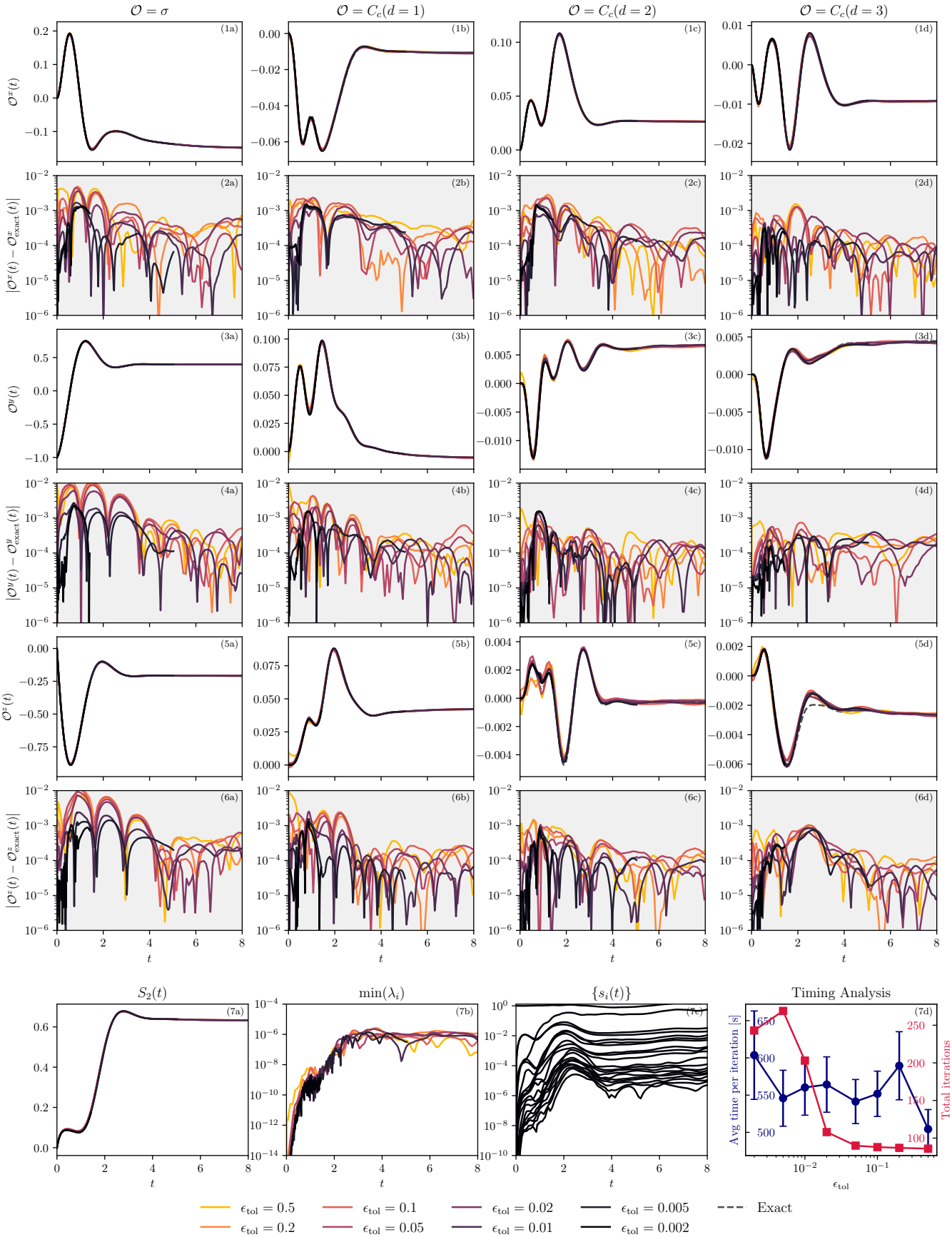

FIG. S34. **Convergence with ϵ_{tol}. Transverse-field Ising model with super-long-range competing interactions, $N = 10$.** For panel descriptions, see Supplementary Note 2 E.

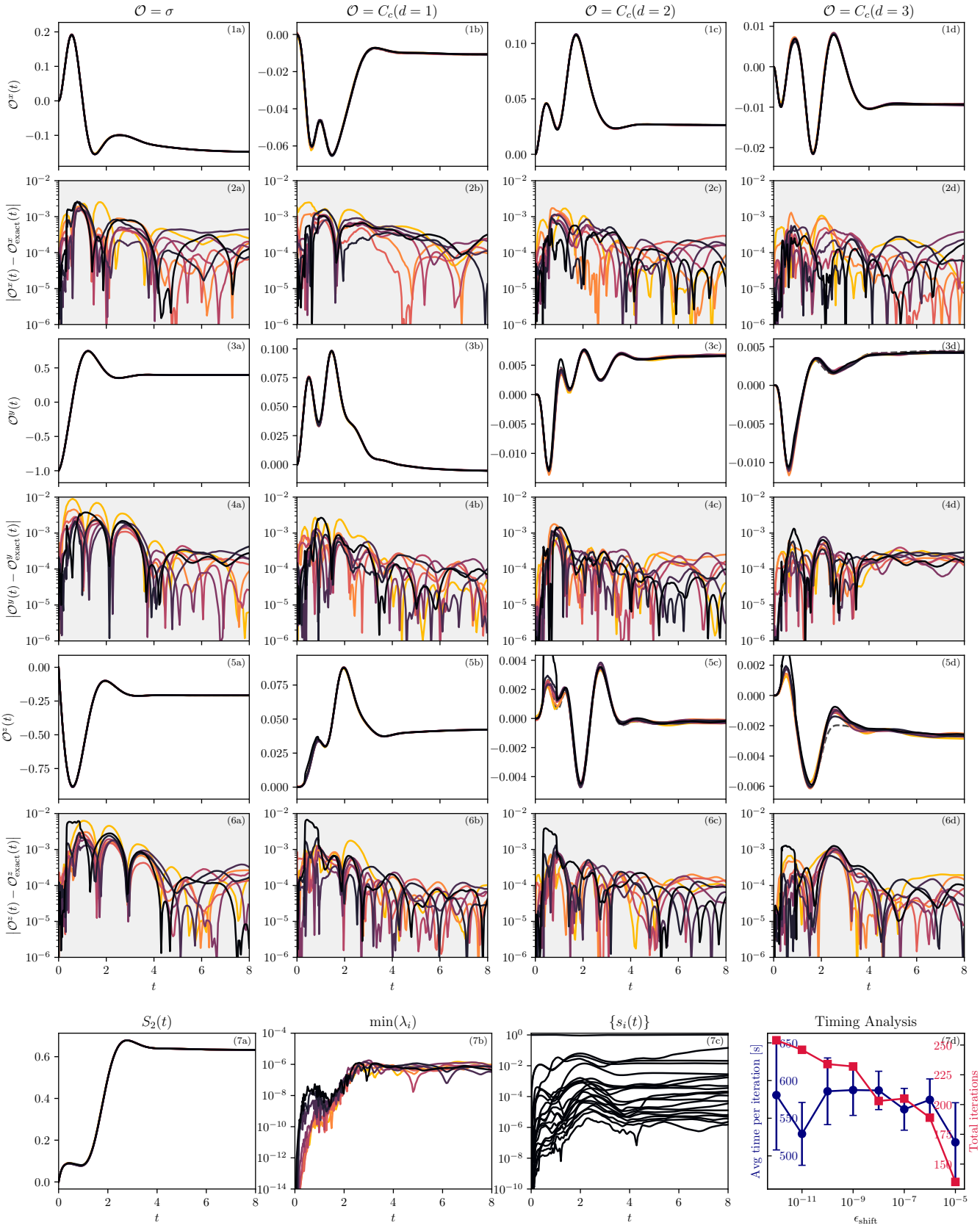

FIG. S35. **Convergence with ϵ_{shift}. Transverse-field Ising model with super-long-range competing interactions, $N = 10$.** For panel descriptions, see Supplementary Note 2 E.

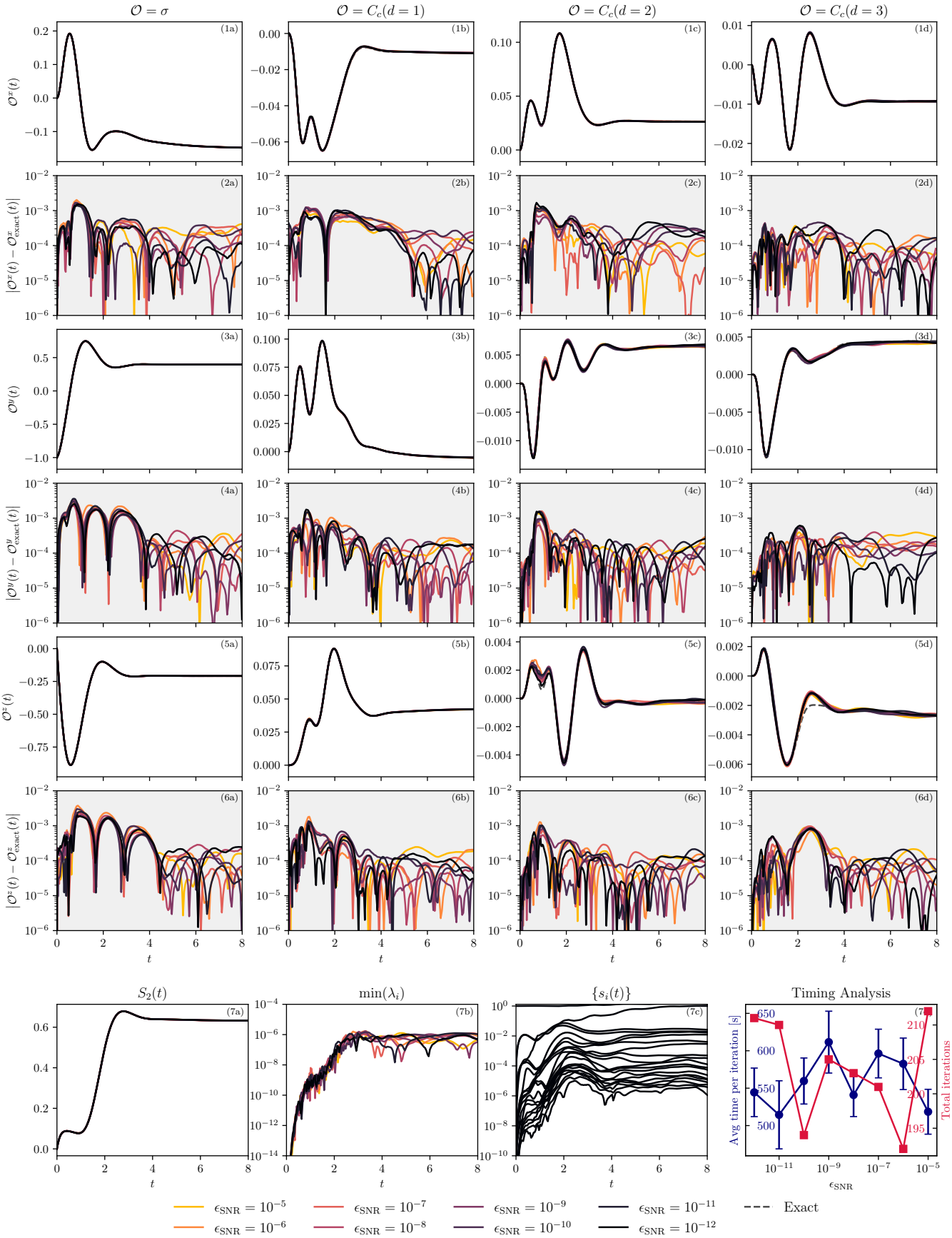

FIG. S36. **Convergence with ϵ_{SNR}. Transverse-field Ising model with super-long-range competing interactions, $N = 10$.** For panel descriptions, see Supplementary Note 2 E.

N. Transverse-field Ising model with super-long-range competing interactions, $N = 200$

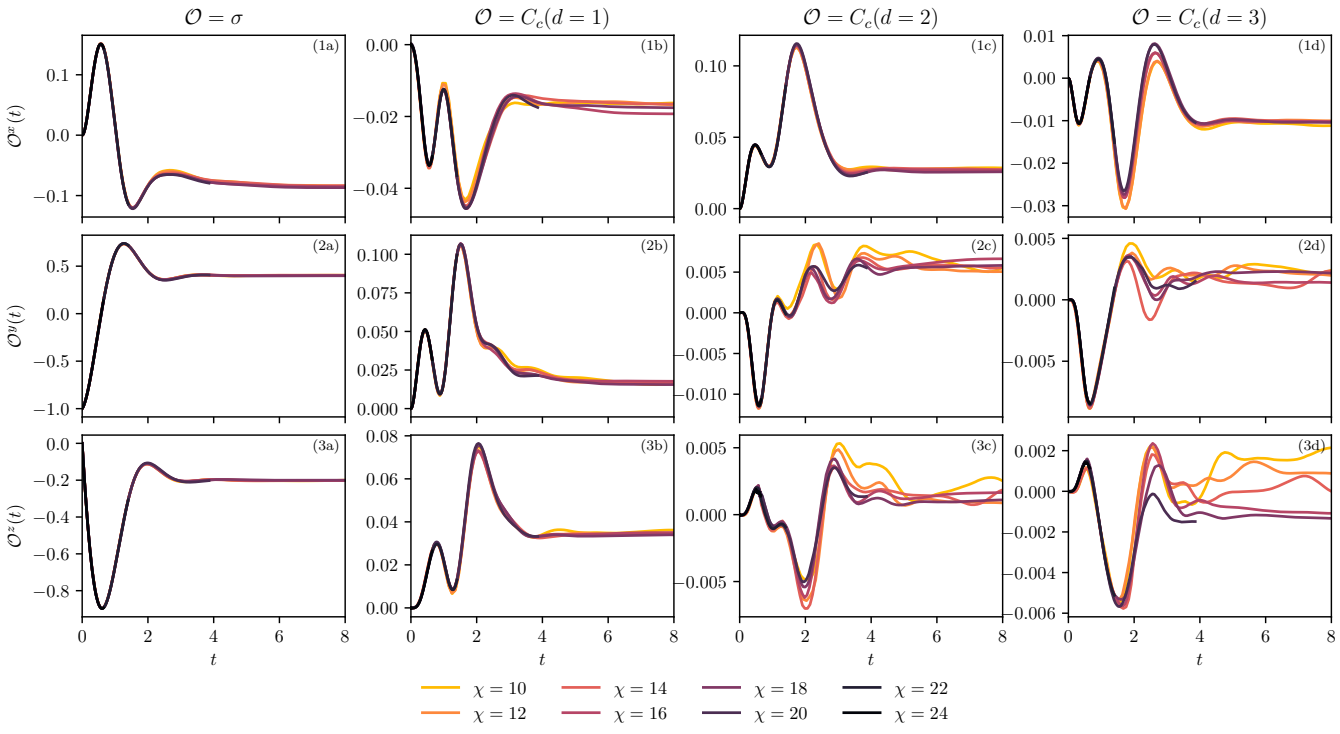

FIG. S37. **Convergence with χ. Transverse-field Ising model with super-long-range competing interactions, $N = 200$.** For panel descriptions, see Supplementary Note 2 F.

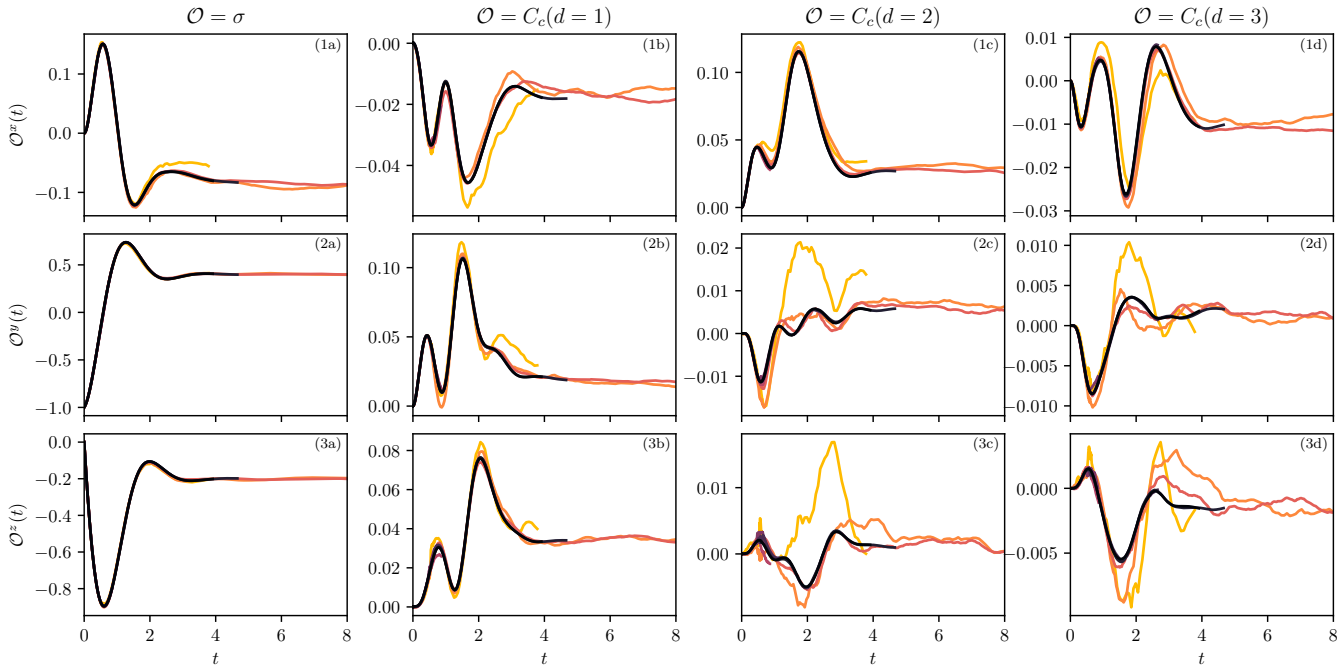

FIG. S38. **Convergence with N_{MC}. Transverse-field Ising model with super-long-range competing interactions, $N = 200$.** For panel descriptions, see Supplementary Note 2 F.

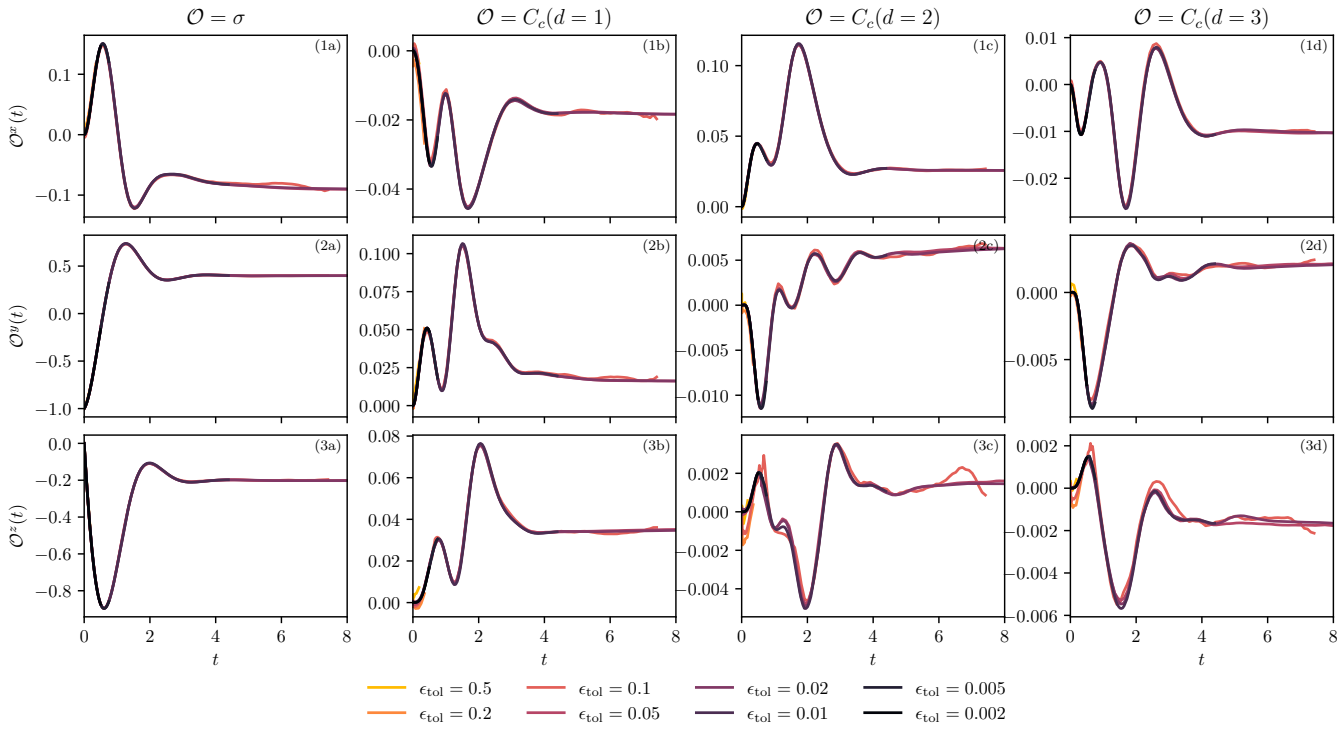

FIG. S39. **Convergence with ϵ_{tol}. Transverse-field Ising model with super-long-range competing interactions, $N = 200$.** For panel descriptions, see Supplementary Note 2 F.

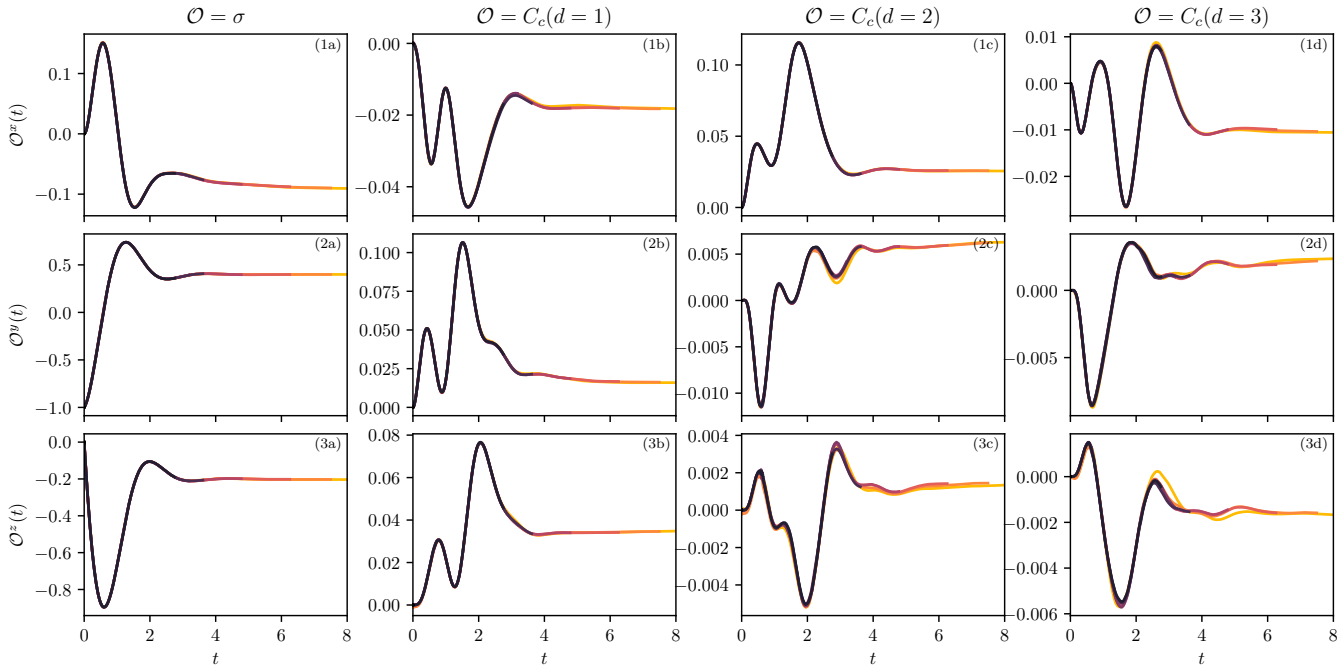

FIG. S40. **Convergence with ϵ_{shift}. Transverse-field Ising model with super-long-range competing interactions, $N = 200$.** For panel descriptions, see Supplementary Note 2 F.

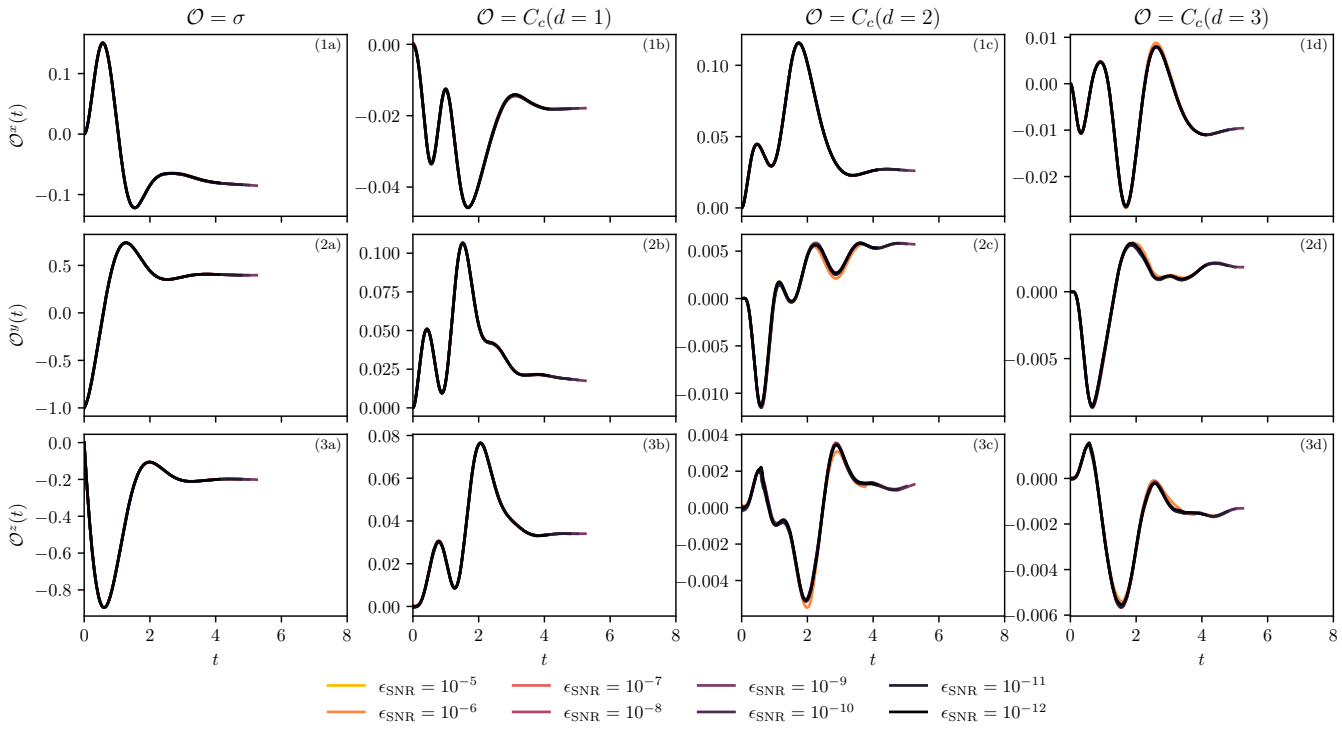

FIG. S41. **Convergence with ϵ_{SNR}. Transverse-field Ising model with super-long-range competing interactions, $N = 200$.** For panel descriptions, see Supplementary Note 2 F.

O. XYZ model with short-range interactions, $N = 10$

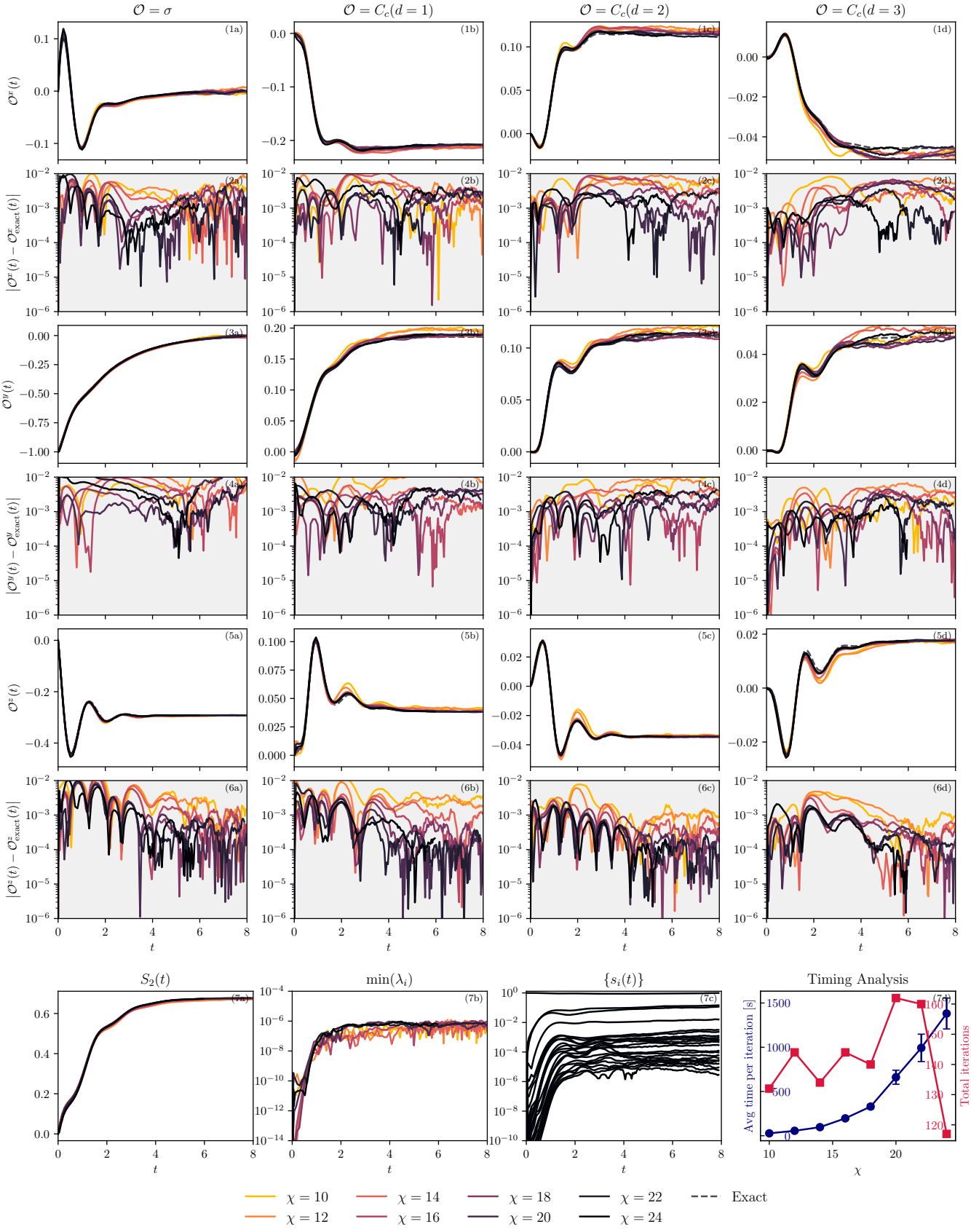

FIG. S42. **Convergence with χ. XYZ model with short-range interactions, $N = 10$.** For panel descriptions, see Supplementary Note 2 E.

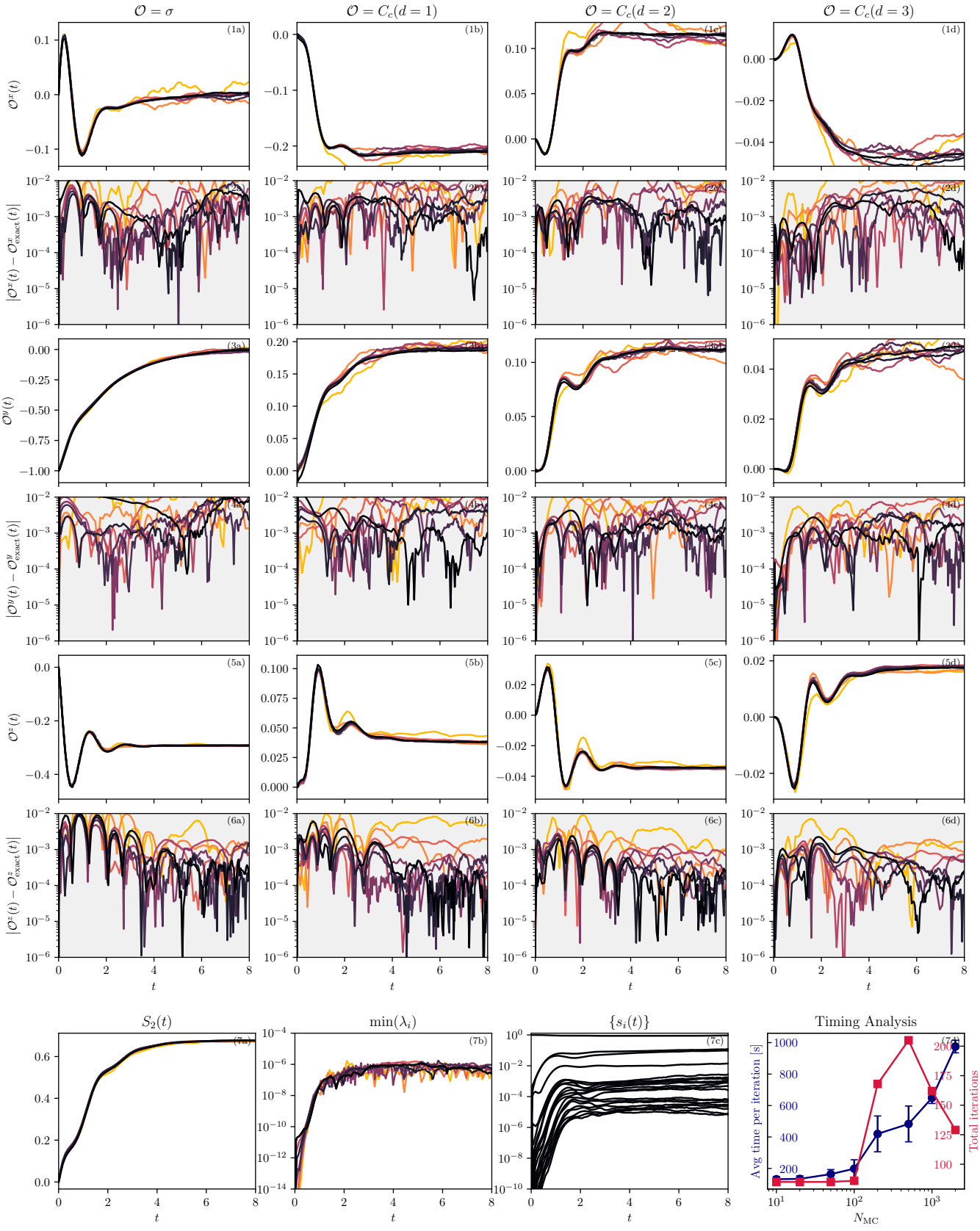

FIG. S43. **Convergence with N_{MC}. XYZ model with short-range interactions,** $N = 10$**.** For panel descriptions, see Supplementary Note 2 E.

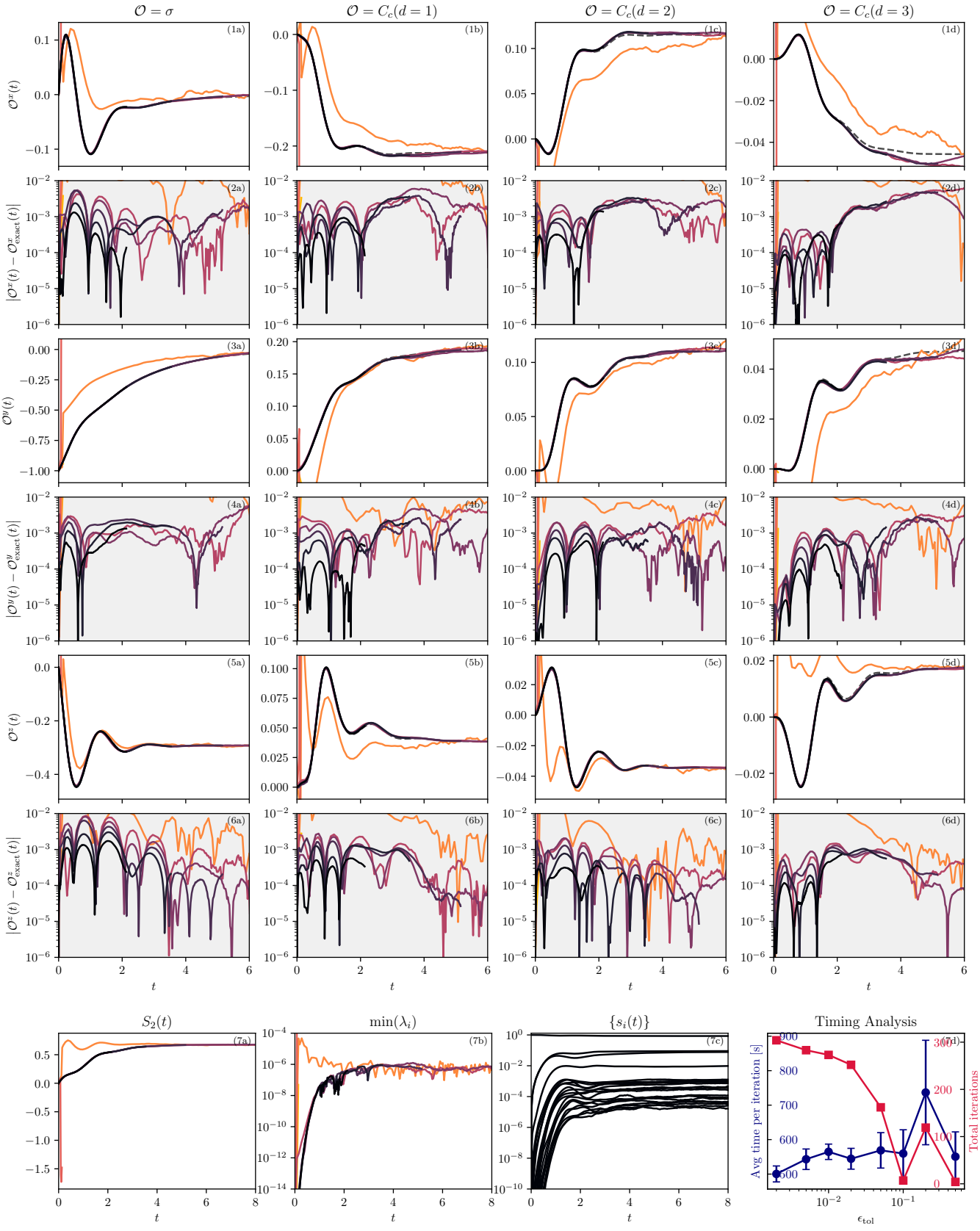

FIG. S44. **Convergence with ϵ_{tol}. XYZ model with short-range interactions, $N = 10$.** For panel descriptions, see Supplementary Note 2 E.

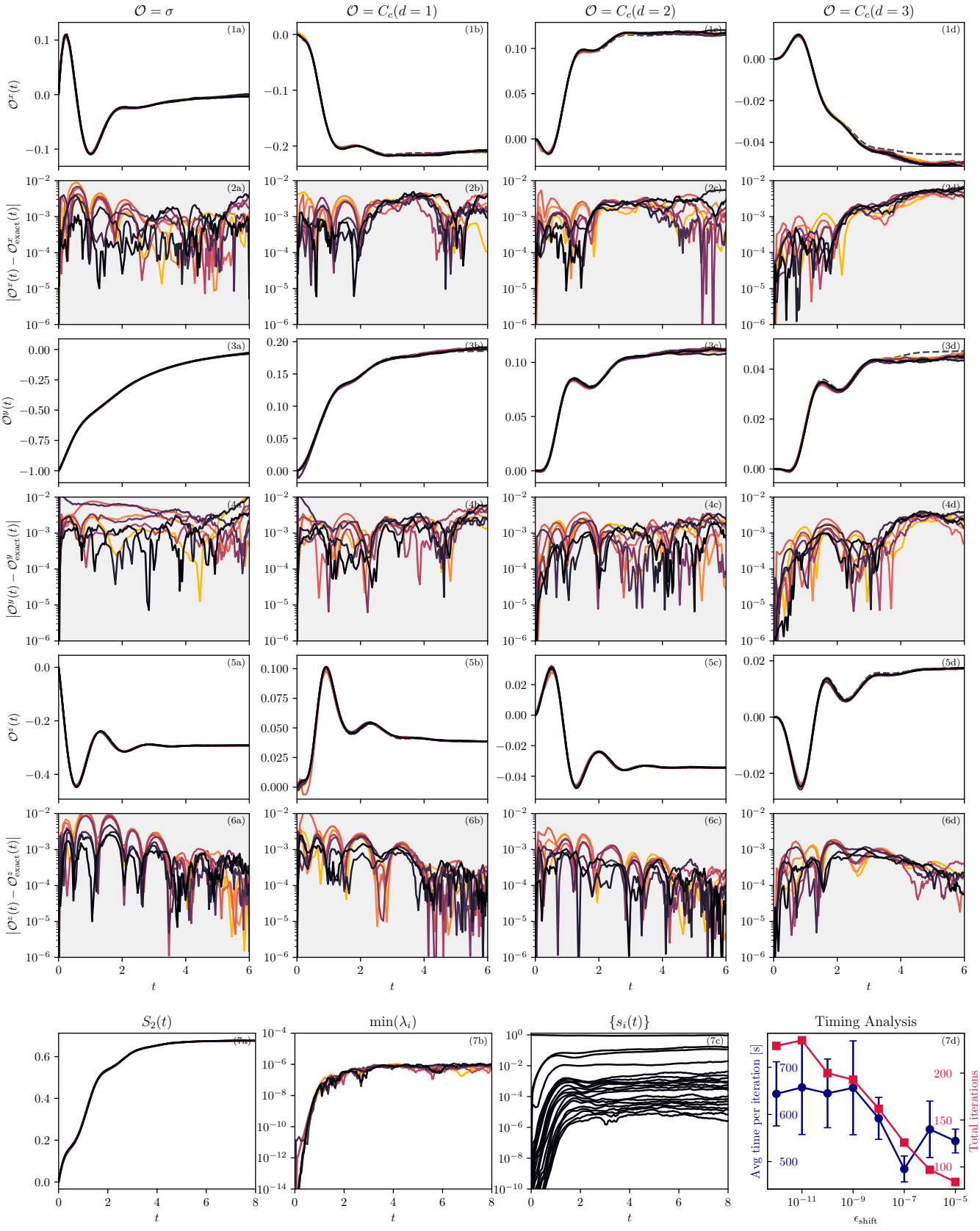

FIG. S45. **Convergence with ϵ_{shift}. XYZ model with short-range interactions,** $N = 10$**.** For panel descriptions, see Supplementary Note 2 E.

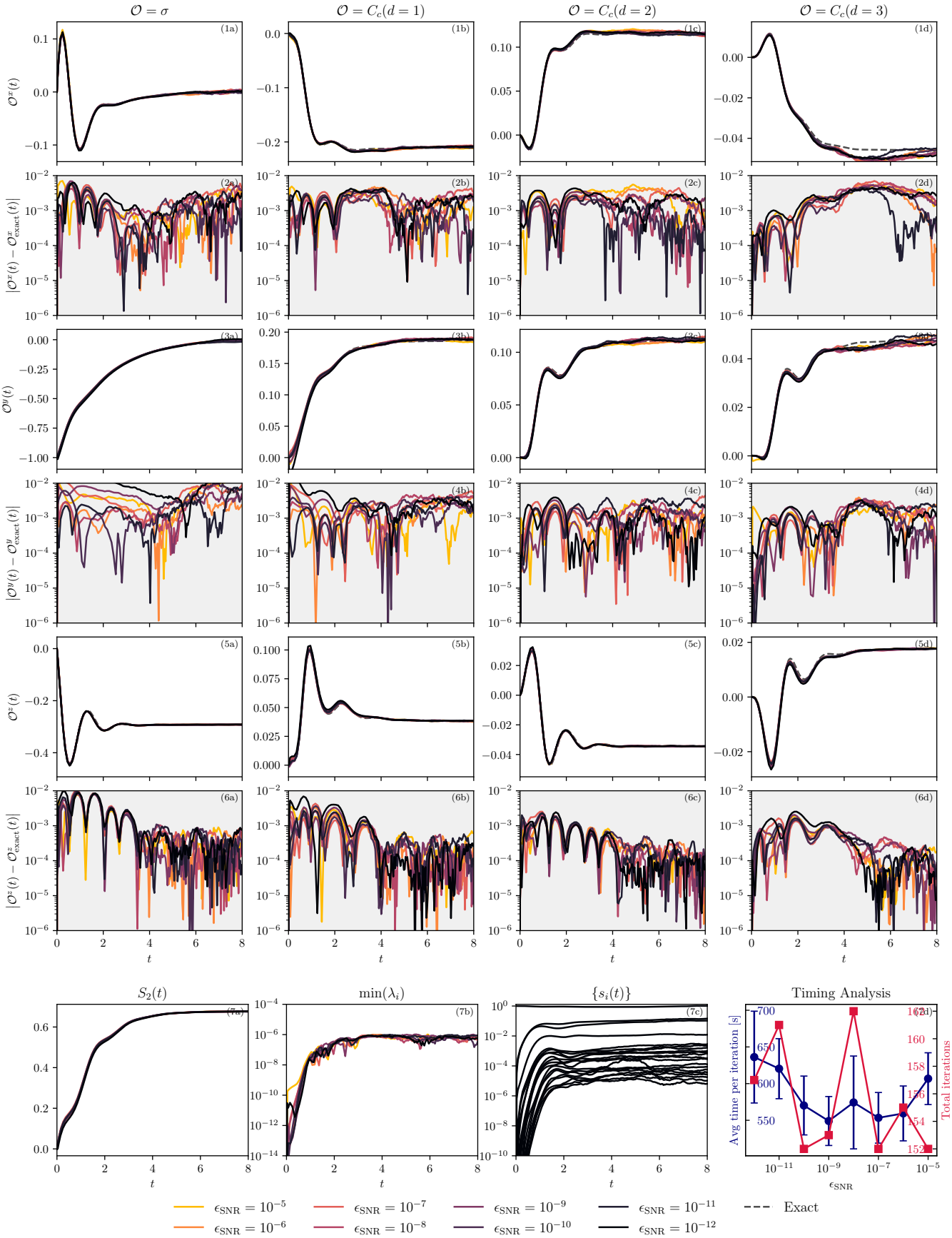

FIG. S46. **Convergence with ϵ_{SNR}. XYZ model with short-range interactions,** $N = 10$**.** For panel descriptions, see Supplementary Note 2 E.

P. XYZ model with short-range interactions, $N = 50$

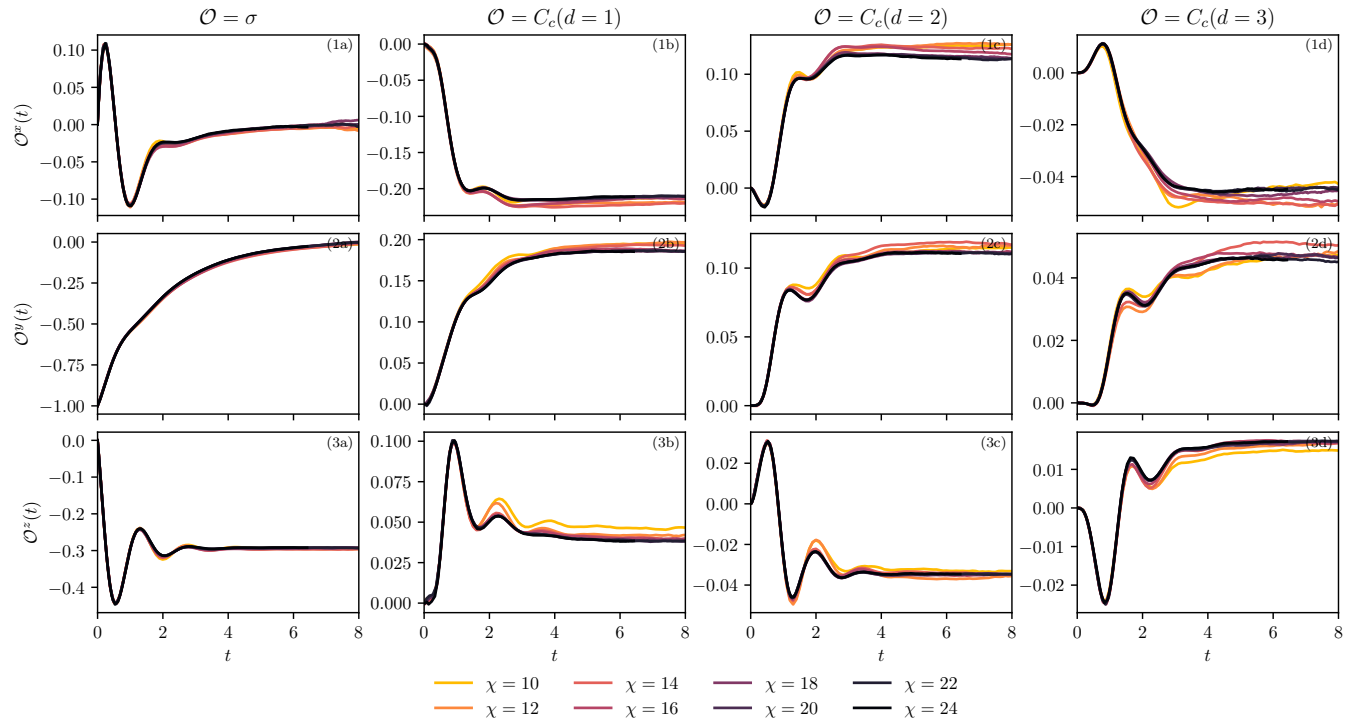

FIG. S47. **Convergence with χ. XYZ model with short-range interactions, $N = 50$.** For panel descriptions, see Supplementary Note 2 F.

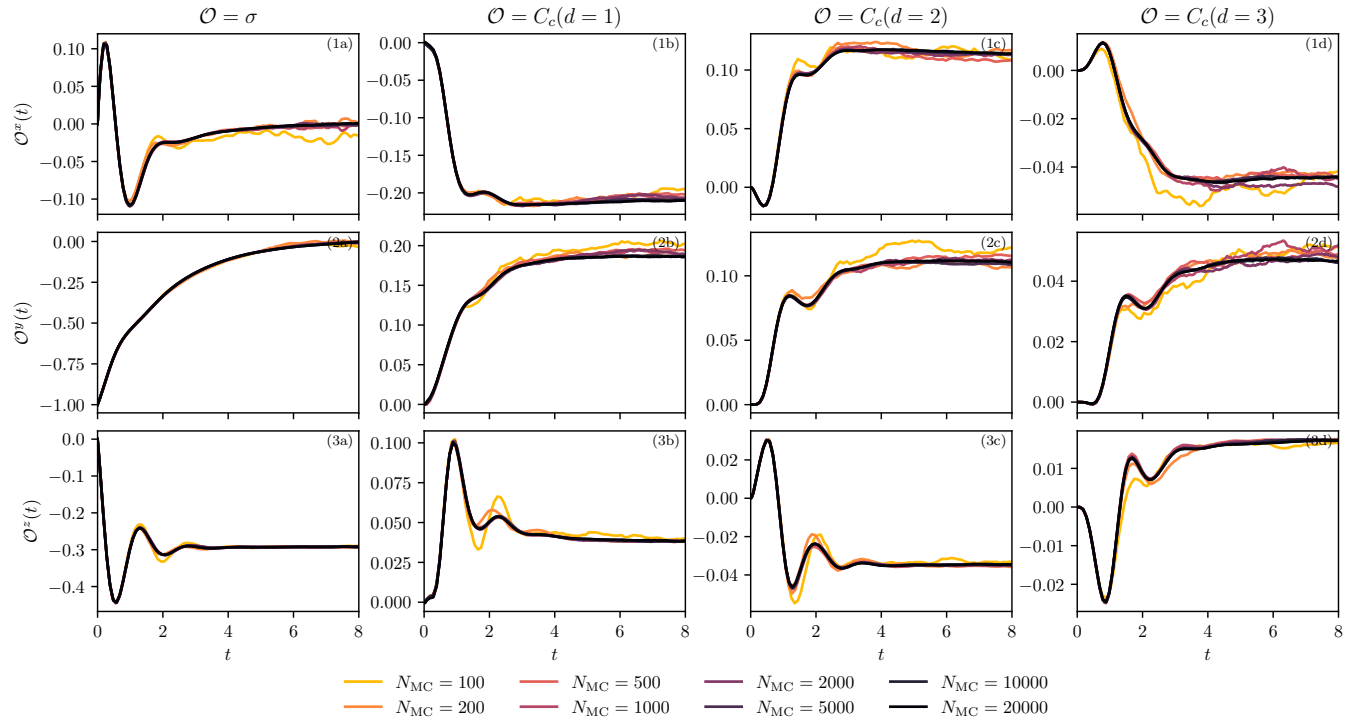

FIG. S48. **Convergence with N_{MC}. XYZ model with short-range interactions, $N = 50$.** For panel descriptions, see Supplementary Note 2 F.

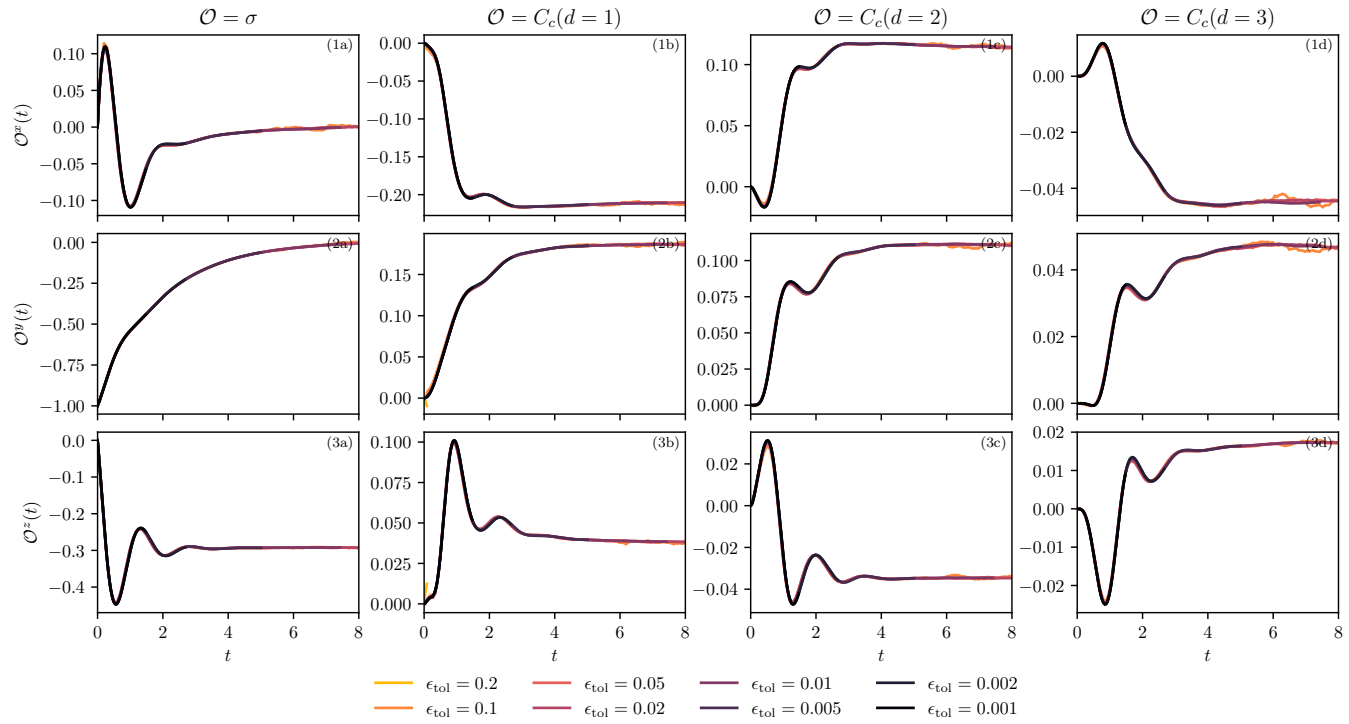

FIG. S49. **Convergence with ϵ_{tol}. XYZ model with short-range interactions, $N = 50$.** For panel descriptions, see Supplementary Note 2 F.

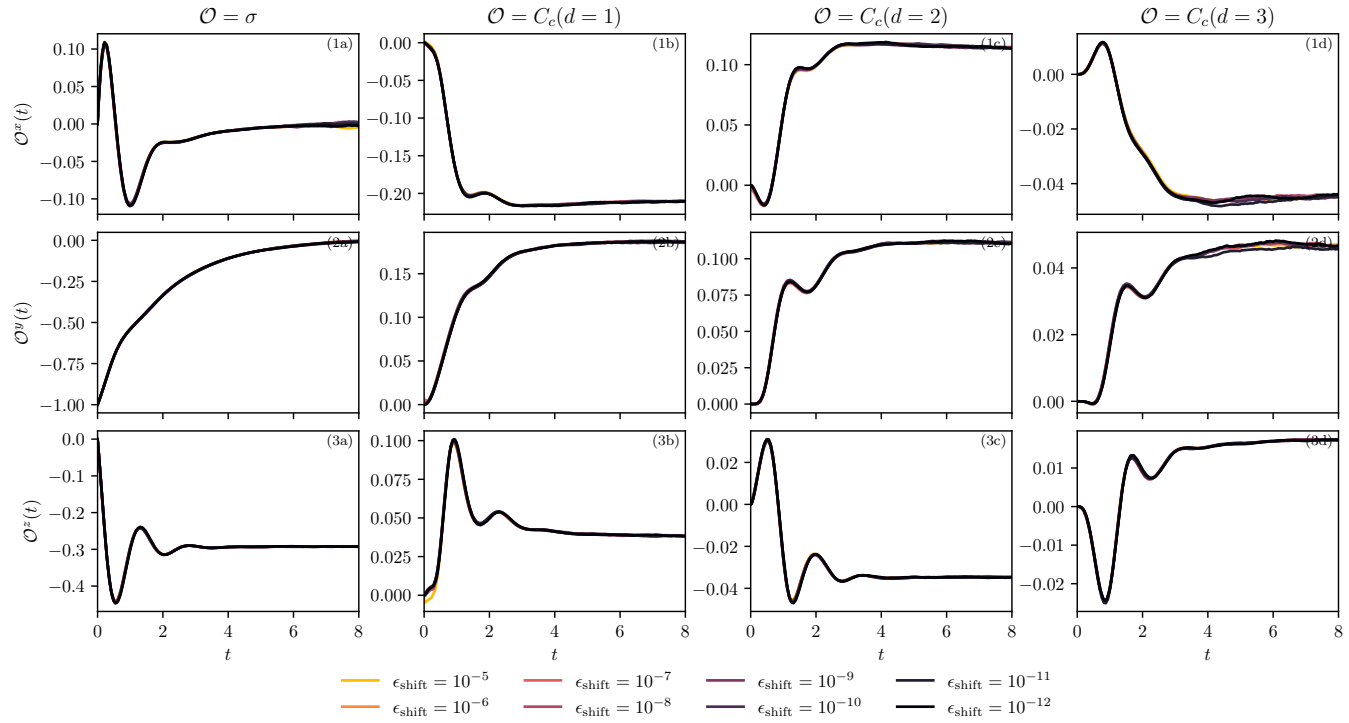

FIG. S50. **Convergence with ϵ_{shift}. XYZ model with short-range interactions,** $N = 50$**.** For panel descriptions, see Supplementary Note 2 F.

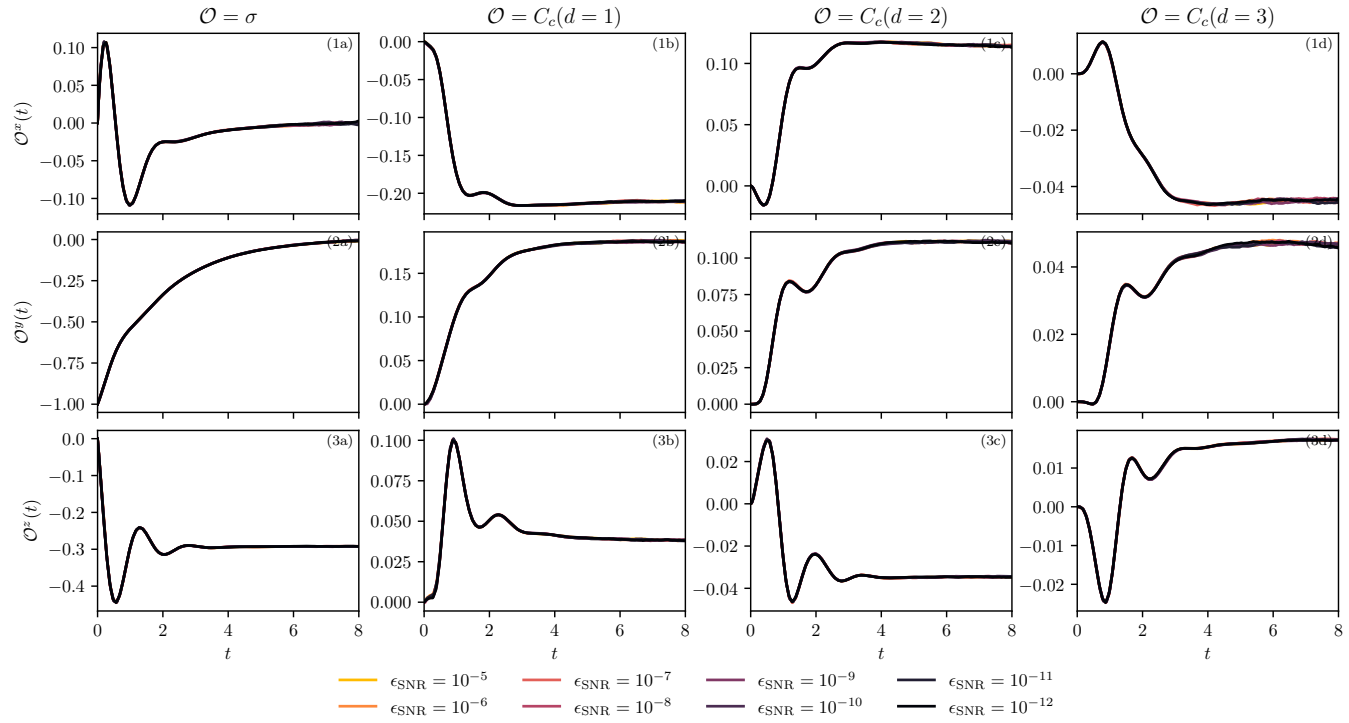

FIG. S51. **Convergence with ϵ_{SNR}. XYZ model with short-range interactions,** $N = 50$**.** For panel descriptions, see Supplementary Note 2 F.

Q. XYZ model with long-range competing interactions, $N = 10$

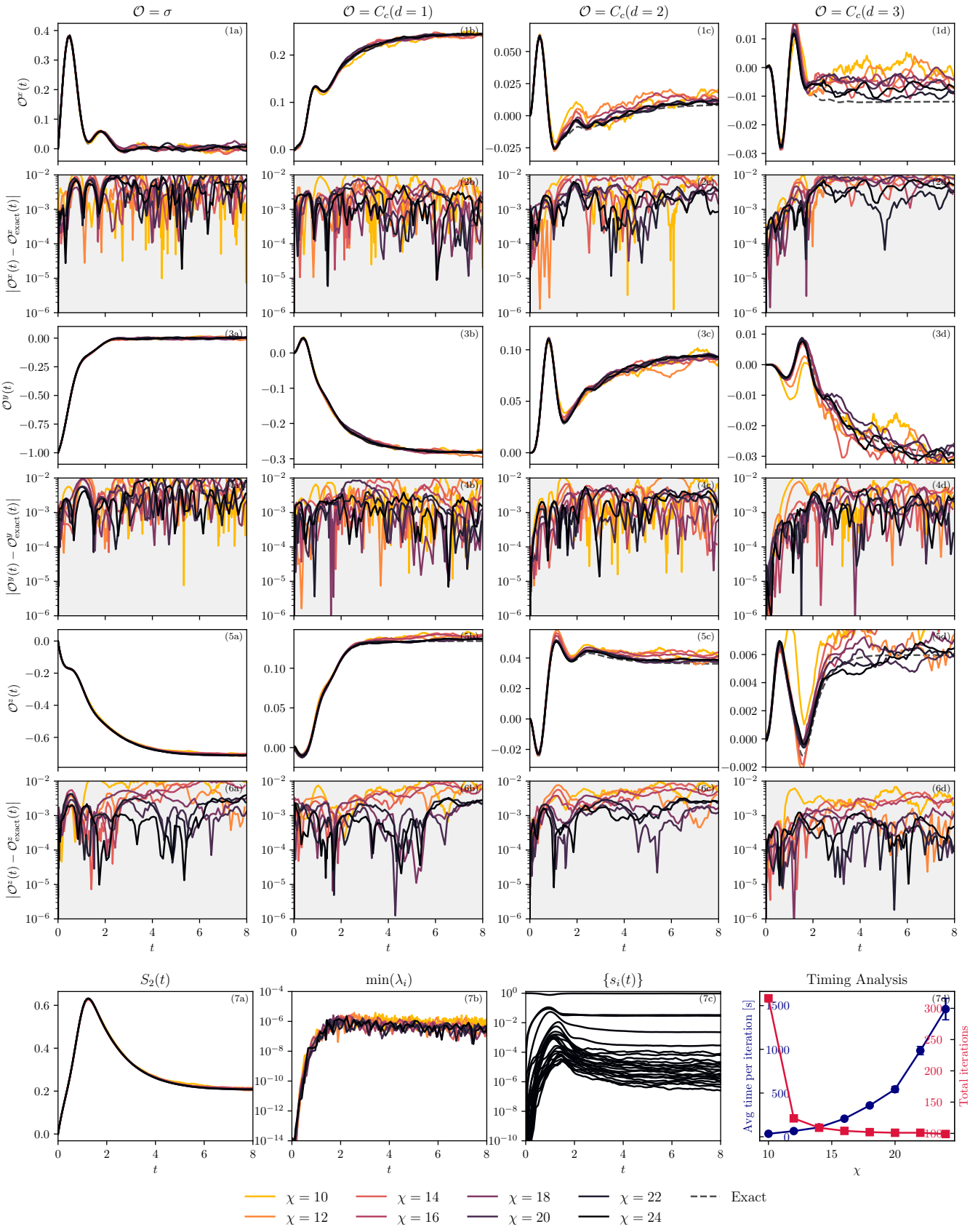

FIG. S52. **Convergence with χ. XYZ model with super-long-range competing interactions, $N = 10$.** For panel descriptions, see Supplementary Note 2 E.

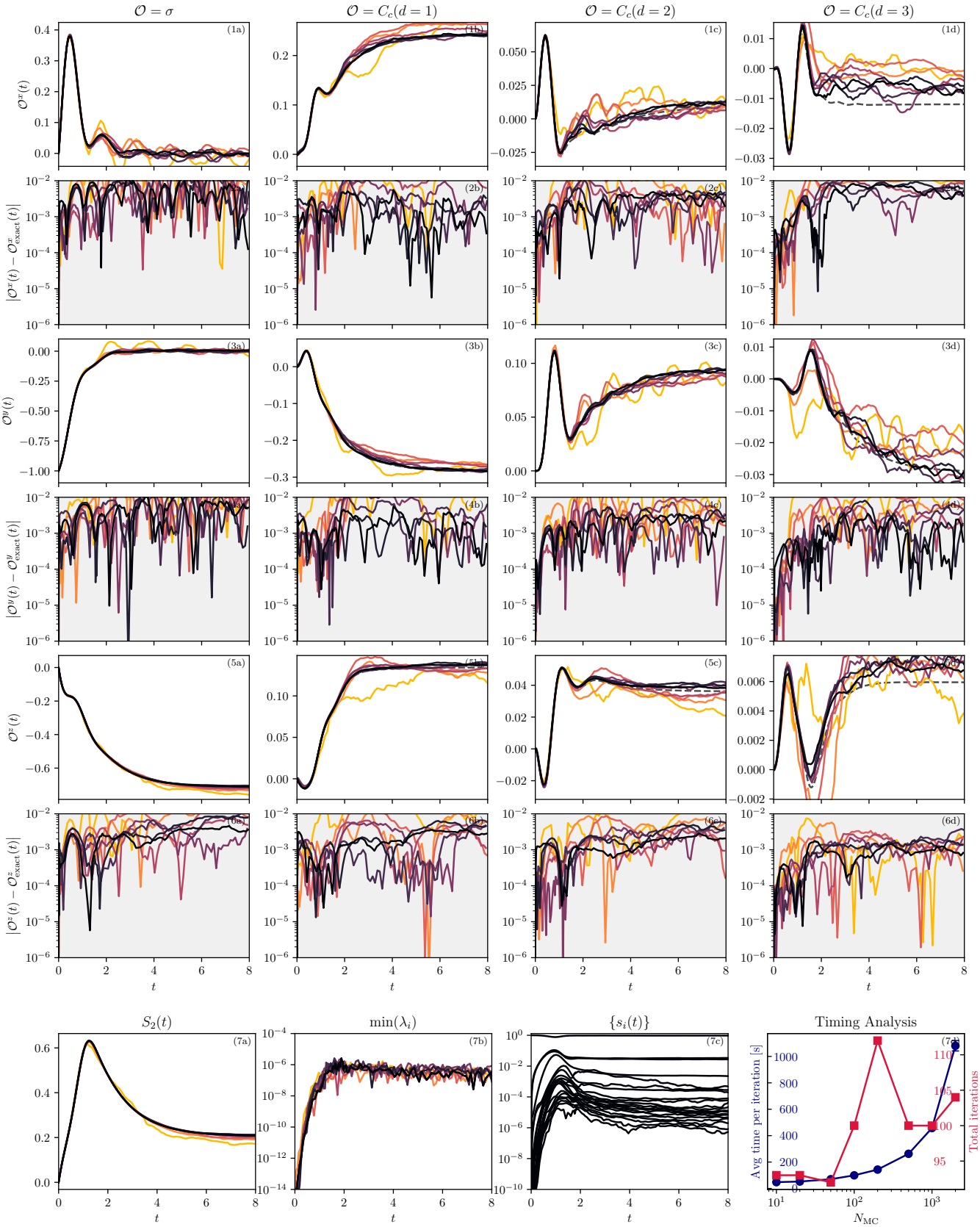

FIG. S53. **Convergence with N_{MC}. XYZ model with long-range competing interactions,** $N = 10$. For panel descriptions, see Supplementary Note 2 E.

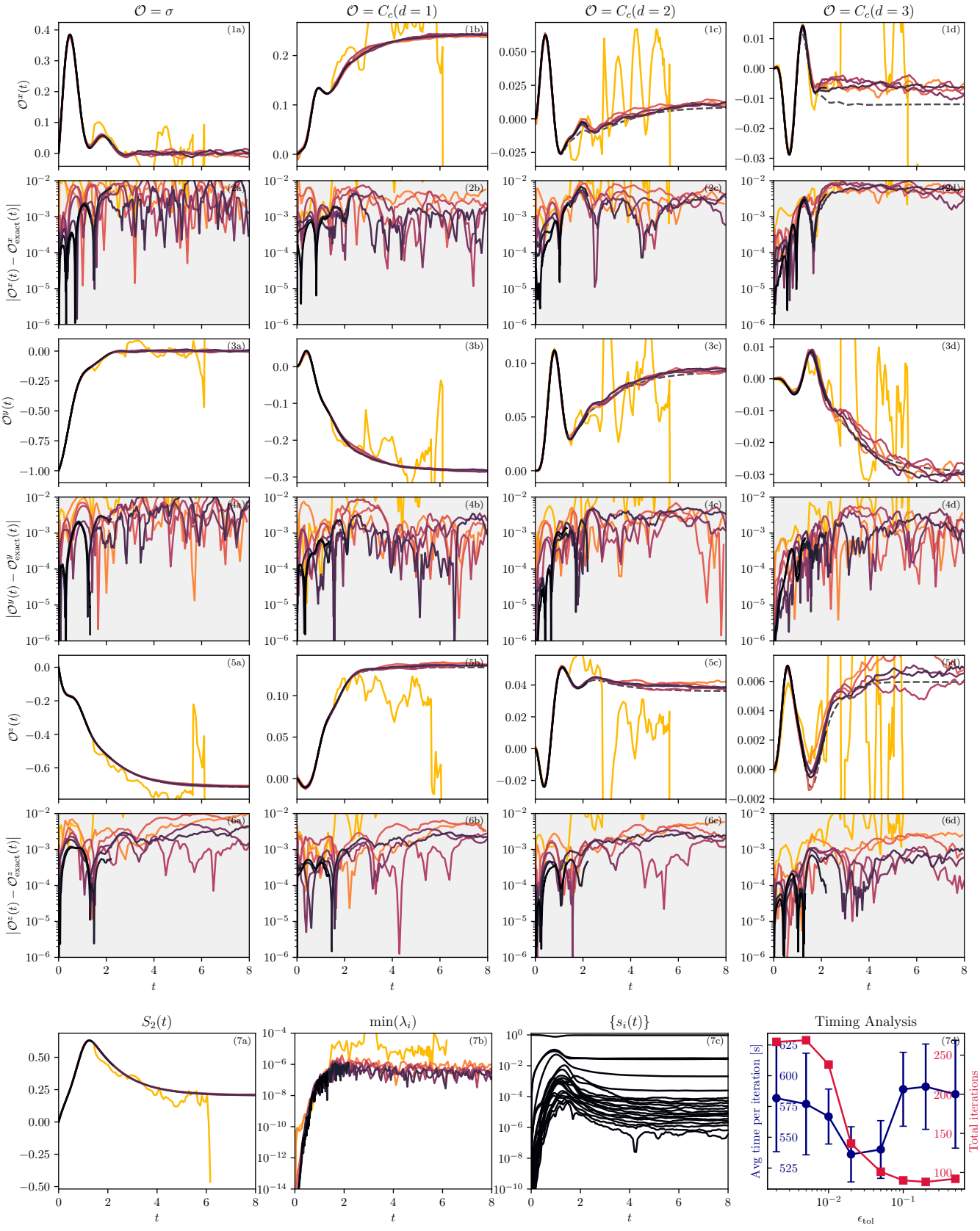

FIG. S54. **Convergence with ϵ_{tol}. XYZ model with long-range competing interactions, $N = 10$.** For panel descriptions, see Supplementary Note 2 E.

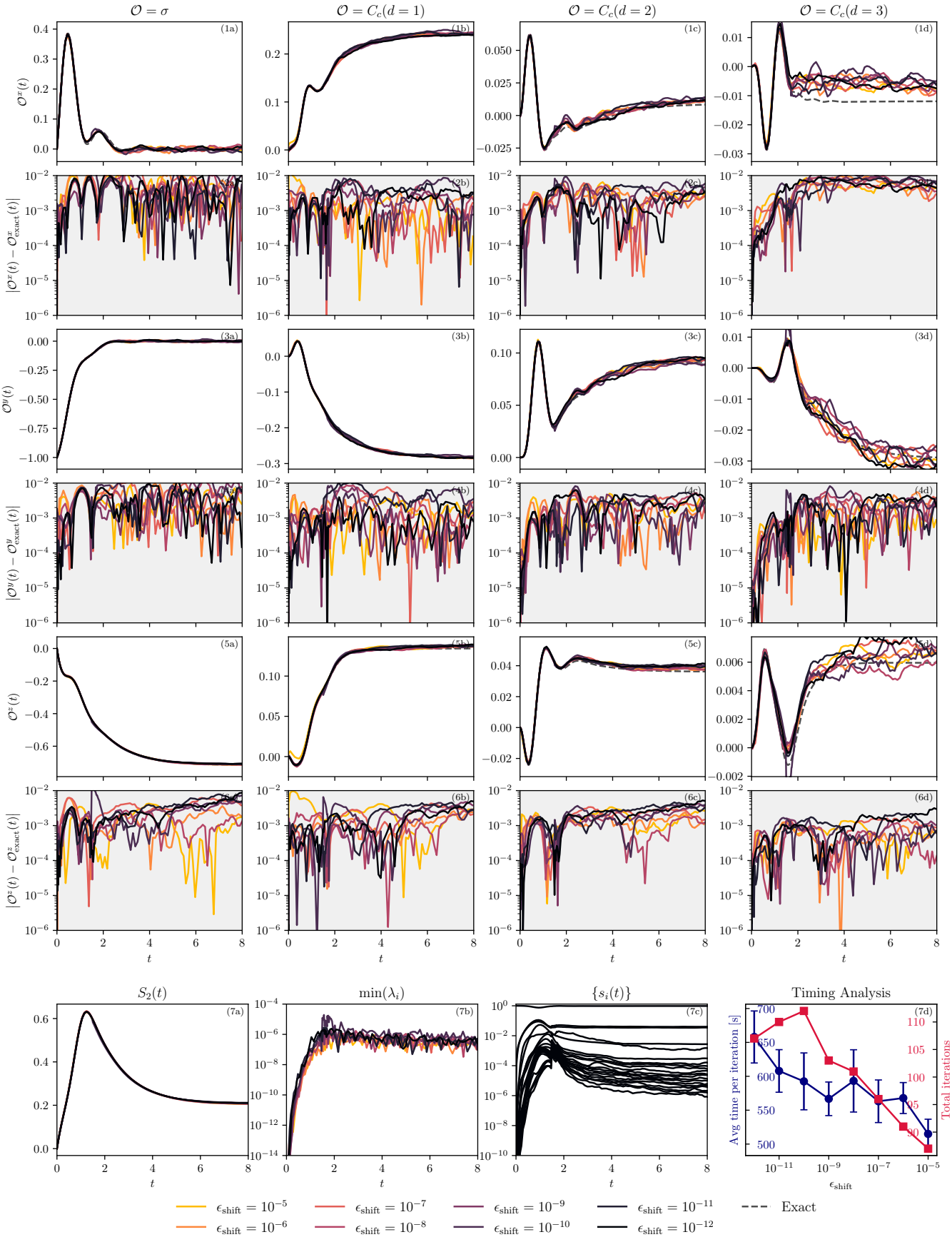

FIG. S55. **Convergence with ϵ_{shift}. XYZ model with long-range competing interactions,** $N = 10$**.** For panel descriptions, see Supplementary Note 2 E.

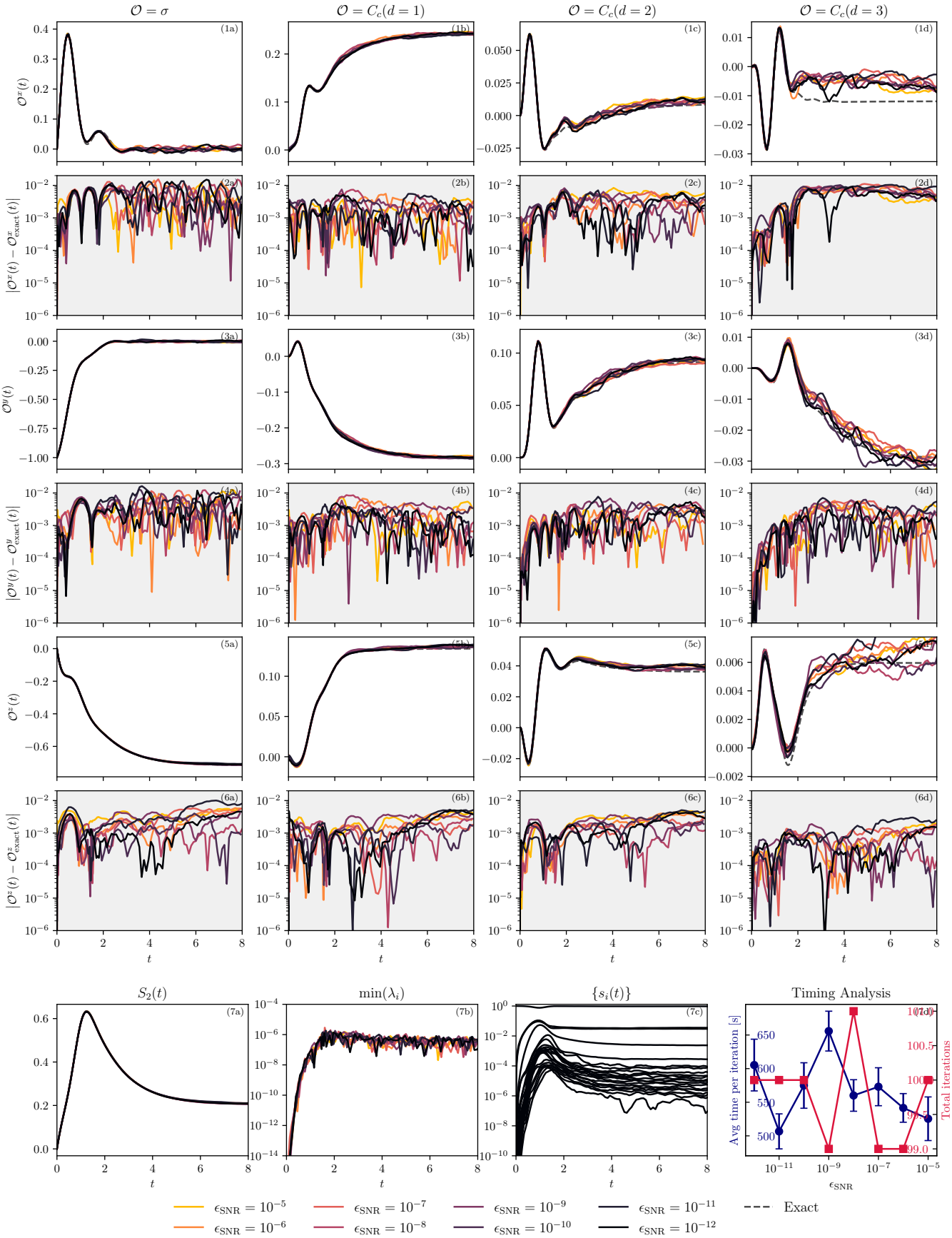

FIG. S56. **Convergence with ϵ_{SNR}. XYZ model with long-range competing interactions,** $N = 10$**.** For panel descriptions, see Supplementary Note 2 E.

R. XYZ model with long-range competing interactions, $N = 50$

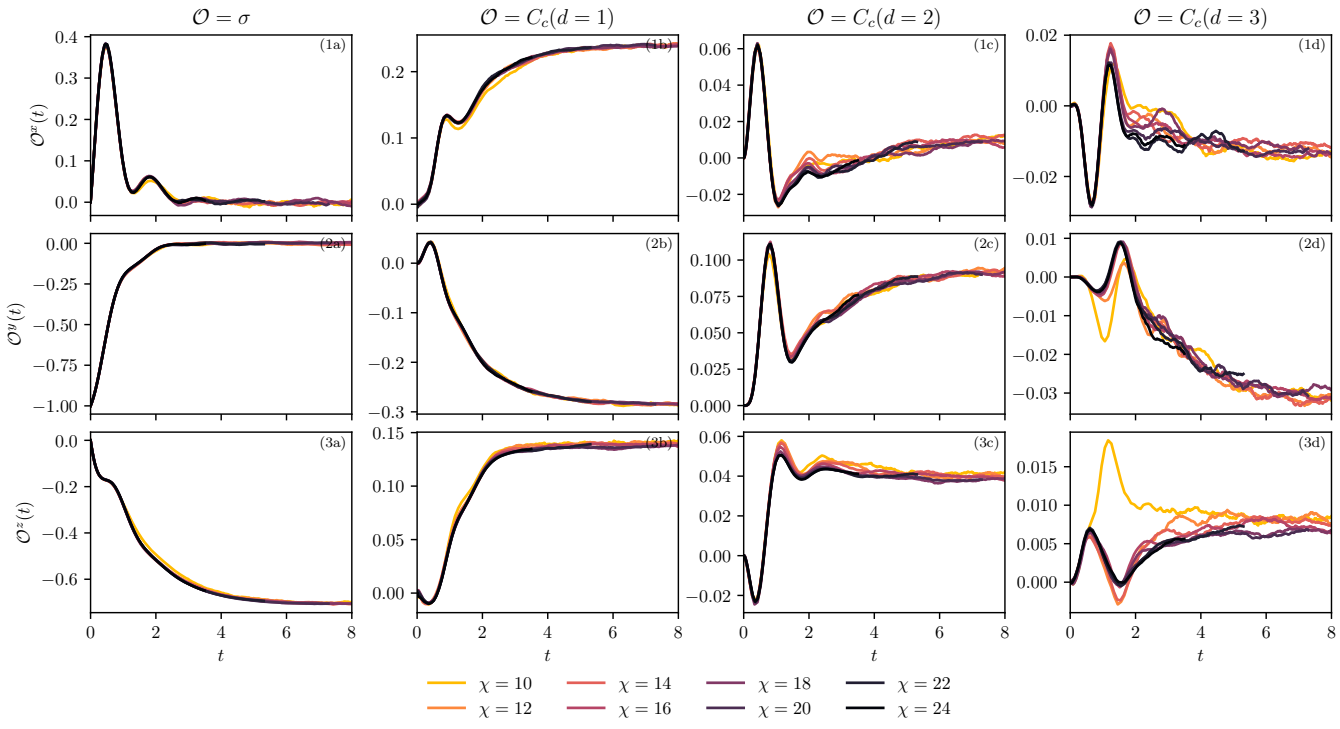

FIG. S57. **Convergence with χ. XYZ model with long-range competing interactions, $N = 50$.** For panel descriptions, see Supplementary Note 2 F.

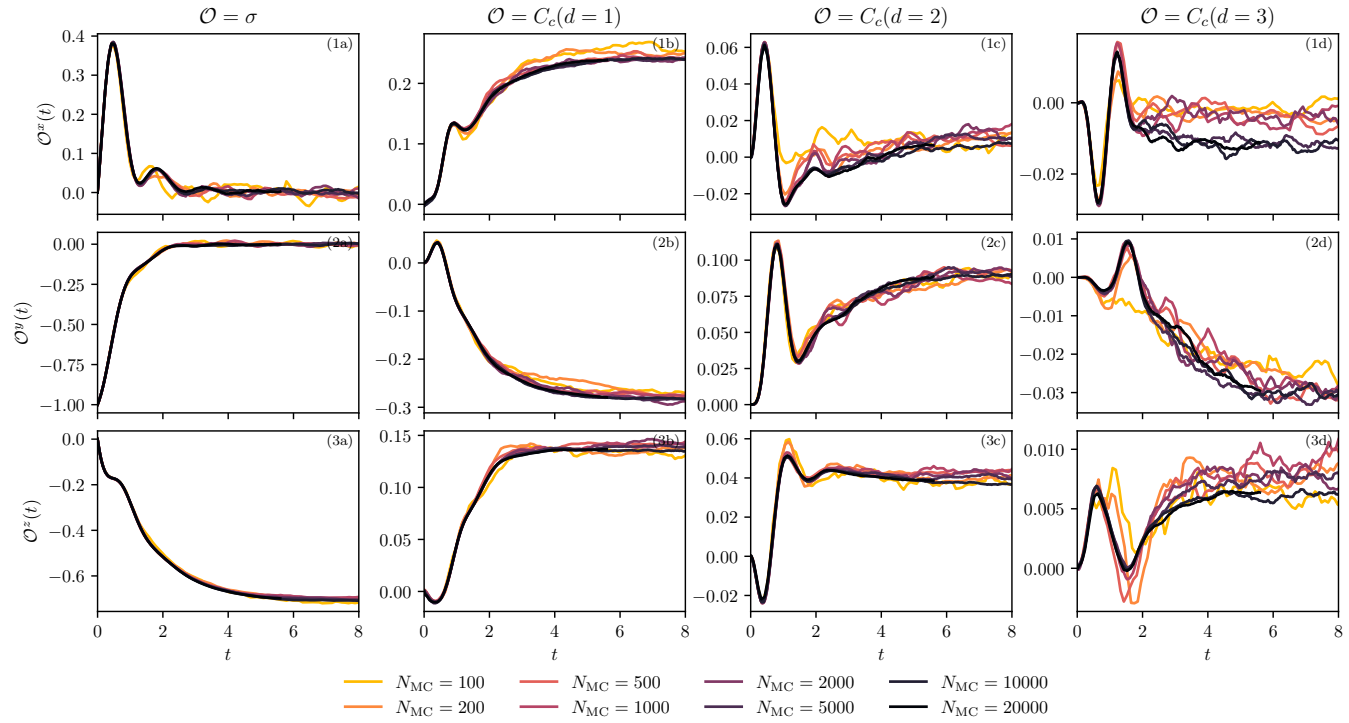

FIG. S58. **Convergence with N_{MC}. XYZ model with long-range competing interactions,** $N = 50$**.** For panel descriptions, see Supplementary Note 2 F.

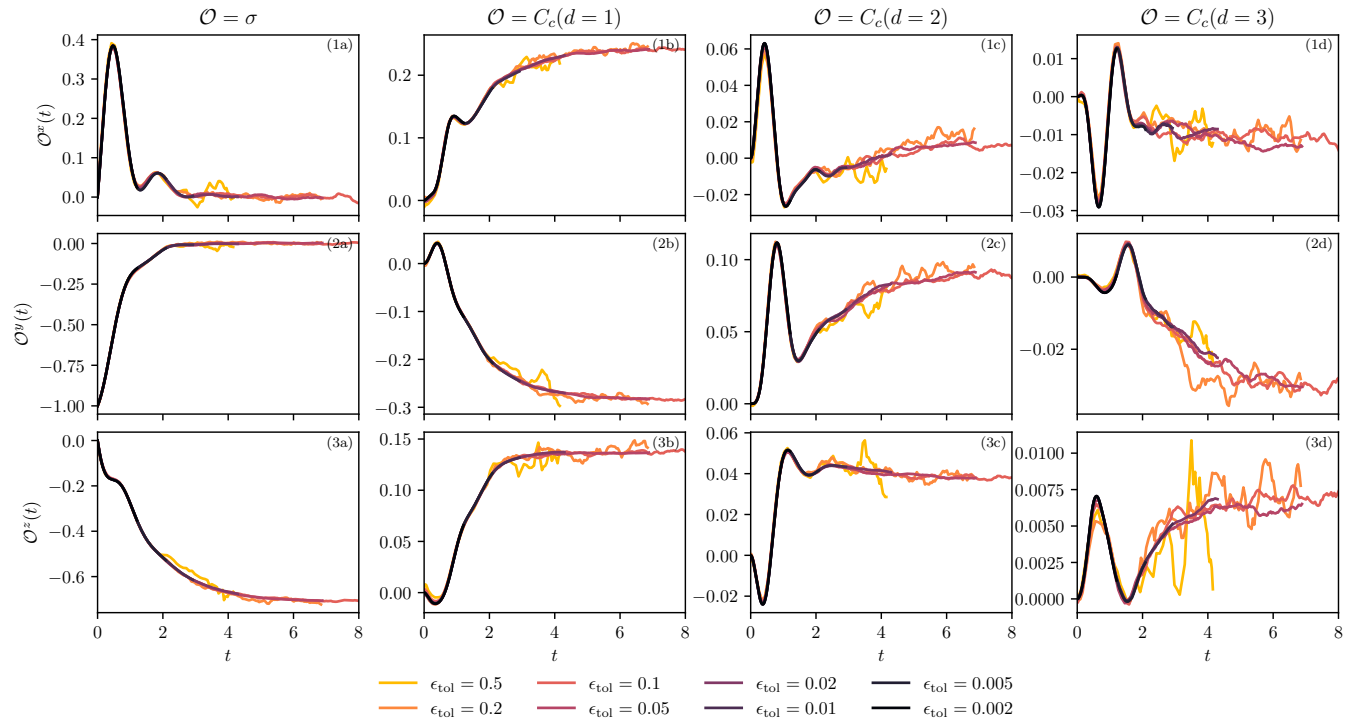

FIG. S59. **Convergence with ϵ_{tol}. XYZ model with long-range competing interactions,** $N = 50$**.** For panel descriptions, see Supplementary Note 2 F.

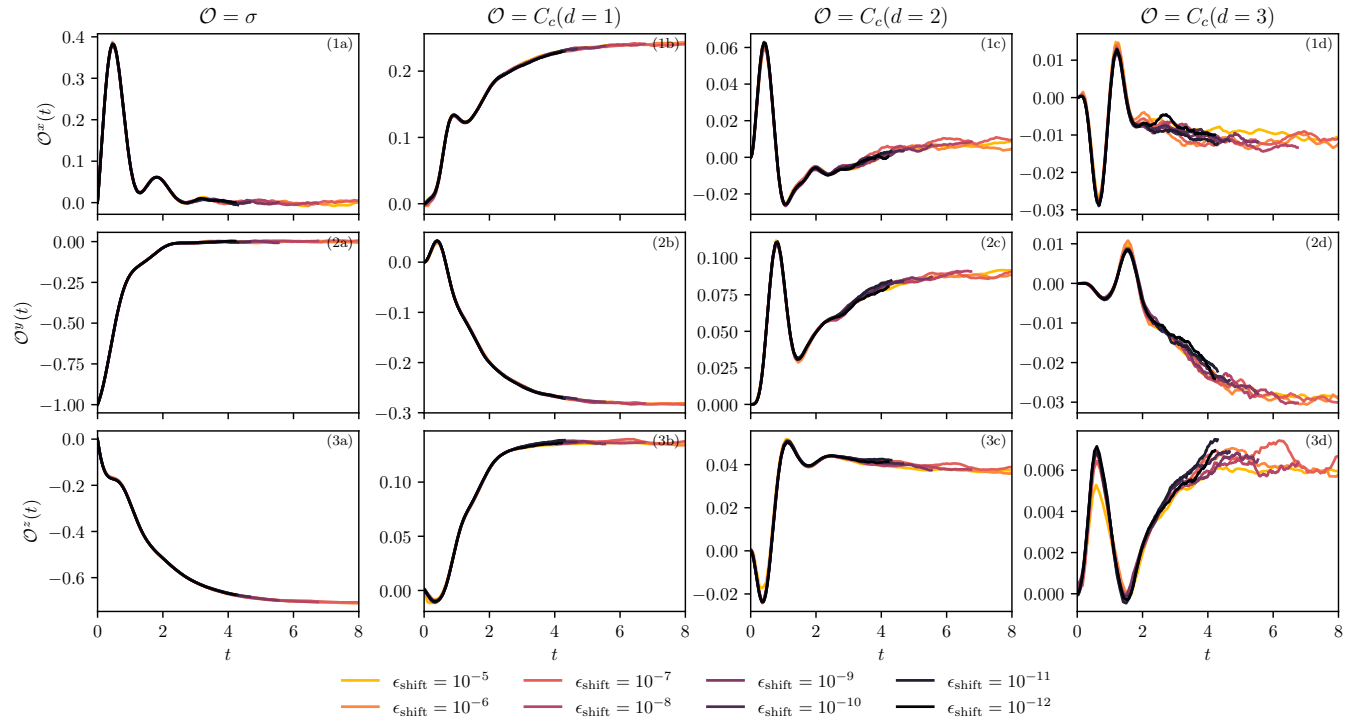

FIG. S60. **Convergence with ϵ_{shift}. XYZ model with long-range competing interactions,** $N = 50$**.** For panel descriptions, see Supplementary Note 2 F.

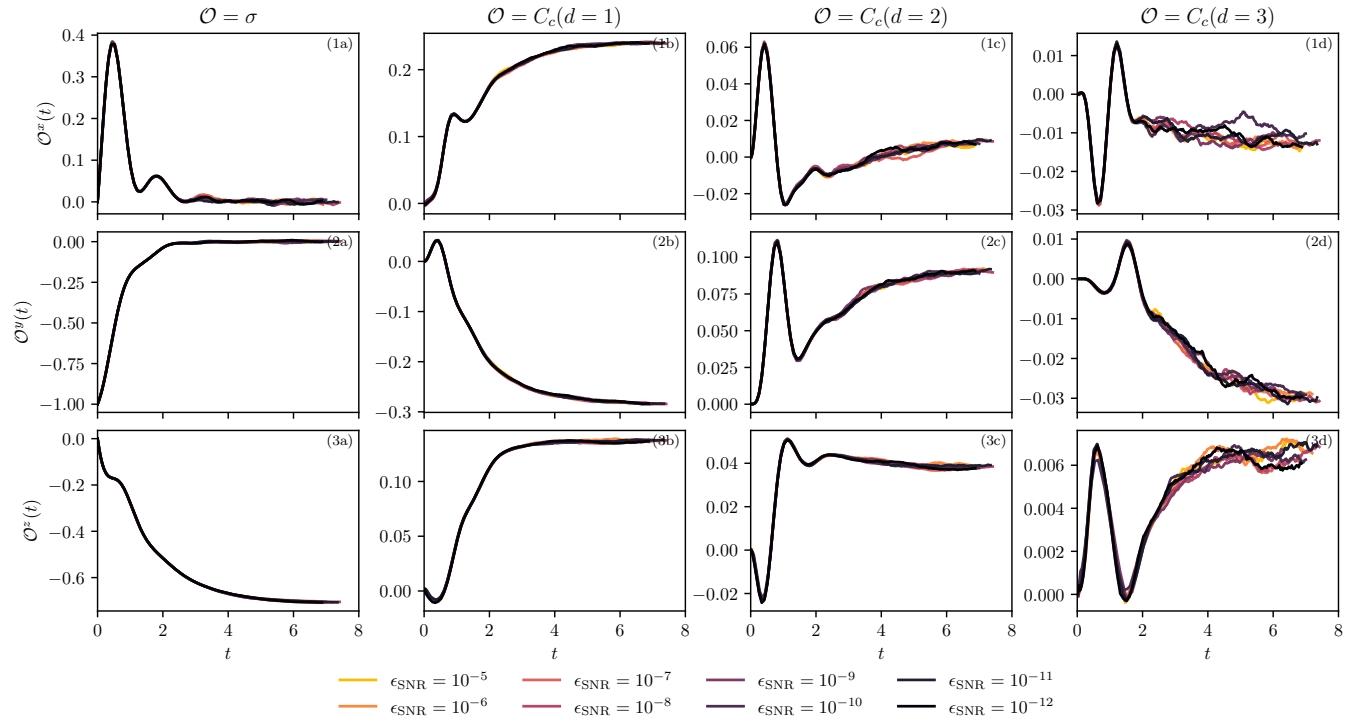

FIG. S61. **Convergence with ϵ_{SNR}. XYZ model with long-range competing interactions,** $N = 50$**.** For panel descriptions, see Supplementary Note 2 F.

S. Structure factor convergence

In Fig. S62 we analyse the convergence of t-VMC+MPO in the computation of the steady-state structure factor phase diagrams for $N = 10$. The small number of sites allows for a direct comparison with exact results to be made. In (a) and (d) the steady-state structure factors are computed via t-VMC+MPO and exact diagonalization. Excellent agreement can be seen, with mean relative errors of 0.08% and 0.04% with and without the competing Coulomb interaction, respectively. We also consider the value of $|\dot{\rho}|^2/N$ at the steady state (subplots (c) and (f)), which acts as a cost function in variational minimization approaches, and which is identically 0 at the true steady state [1]. Small values of less than 10^{-3} can be observed in the competing regime.

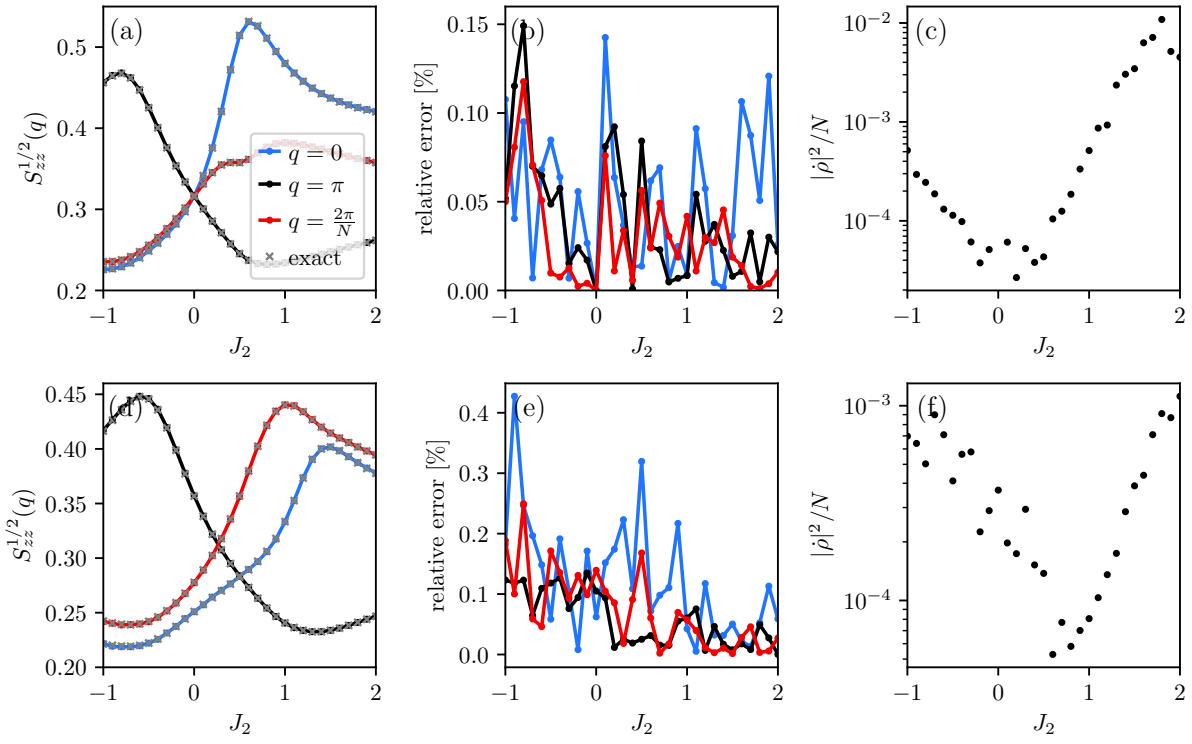

FIG. S62. **Convergence analysis of steady-state structure factor phase diagrams for spin chain with long-range dipolar Ising interactions of $N = 10$ sites**. In the bottom row, additional competing long-range Coulomb Ising interactions are present, following Fig. 5 in the main text. (a) and (d) steady state structure factors compared to exact results (grey crosses). (b) and (e) relative errors in the variational estimate of the structure factor in (a) and (d). (c) and (f) value of $|\dot{\rho}|^2/N$ at the steady-state.

[1] D. A. Hryniuk and M. H. Szymańska, Tensor-network-based variational Monte Carlo approach to the non-equilibrium steady state of open quantum systems, Quantum **8**, 1475 (2024).

[2] M. Schmitt and M. Heyl, Quantum many-body dynamics in two dimensions with artificial neural networks, Phys. Rev. Lett. **125**, 100503 (2020).

[3] E. Stoudenmire and S. R. White, Studying two-dimensional systems with the density matrix renormalization group, Annual Review of Condensed Matter Physics **3**, 111 (2012).

[4] S. Krämer, D. Plankensteiner, L. Ostermann, and H. Ritsch, Quantumoptics.jl: A julia framework for simulating open quantum systems, Computer Physics Communications **227**, 109 (2018).

Figure	N	h	$\boldsymbol{J}$	α	χ	D	method	N_{MC}	N_{MPI}	$\epsilon_{\mathrm{shift}}$	ϵ_{SNR}	$\epsilon_{\mathrm{tol}}/\tau_{\mathrm{Euler}}$
3 (a-c)	200	-1.0	$(J_x, J_y, J_z) = (-1.0, -0.9, -1.2)$	—	20	1	adaptive Heun	200	160	10^{-8}	10^{-4}	0.1
3 (d)	10	-1.0	$J = -0.5$	—	20	1	Euler	5000	8	10^{-5}	10^{-3}	0.05
4 (a-b)	200	0.5	$(J_1, J_2) = (-0.5, 1.0)$	$\alpha_1 = 3$ $\alpha_2 = 6$	10	1	adaptive Heun	2000	4	10^{-6}	10^{-4}	0.05
4 (c-d)	4×4	0.5	$(J_1, J_2) = (-0.25, 0.5)$	$\alpha_1 = 3$ $\alpha_2 = 6$	10	4	adaptive Heun	2000	80	10^{-9}	10^{-4}	0.1
5 (a-b)	20	0.5	$J_1 = 0$ $-1.0 \leq J_2 \leq 2.0$	$\alpha_1 = 1$ $\alpha_2 = 3$	20	1	adaptive Heun	3000	4	10^{-4}	10^{-4}	0.05
5 (c-d)	20-50	0.5	$J_1 = 1.0$ $-1.0 \leq J_2 \leq 2.0$	$\alpha_1 = 1$ $\alpha_2 = 3$	30	1	adaptive Heun	3000	4	10^{-4}	10^{-4}	0.05

TABLE S1. List of parameter and hyperparameter values used in the simulations presented in Figs. 3-5 in the main text. The columns list, in order, total number of sites N, local field strength h, interaction strength vector $\boldsymbol{J}$, interaction decay length α, bond dimension χ, unit cell size D, numerical integration method, number of Monte Carlo samples per Markov chain N_{MC}, number of Markov chains N_{MPI} (each running on a separate MPI process), regularization hyperparameters $\epsilon_{\mathrm{shift}}$ and ϵ_{SNR}, integration tolerance or step size $\epsilon_{\mathrm{tol}}/\tau_{\mathrm{Euler}}$.

Figure	N	h	$J\ (J_1, J_2)$	α_1, α_2	χ	N_{MC}	ϵ_{tol}	$\epsilon_{\mathrm{shift}}$	ϵ_{SNR}
S2	10	1.0	0.5	—	var.	10^5	0.01	10^{-8}	10^{-8}
S3	10	1.0	0.5	—	20	var.	0.01	10^{-8}	10^{-8}
S4	10	1.0	0.5	—	20	10^5	var.	10^{-8}	10^{-8}
S5	10	1.0	0.5	—	20	10^5	0.01	var.	10^{-8}
S6	10	1.0	0.5	—	20	10^5	0.01	10^{-8}	var.
S7	200	1.0	0.5	—	var.	10^5	0.01	10^{-8}	10^{-8}
S8	200	1.0	0.5	—	20	var.	0.01	10^{-8}	10^{-8}
S9	200	1.0	0.5	—	20	10^5	var.	10^{-8}	10^{-8}
S10	200	1.0	0.5	—	20	10^5	0.01	var.	10^{-8}
S11	200	1.0	0.5	—	20	10^5	0.01	10^{-8}	var.
S12	10	1.0	$0.5, -1.0$	3, 6	var.	10^5	0.01	10^{-8}	10^{-8}
S13	10	1.0	$0.5, -1.0$	3, 6	20	var.	0.01	10^{-8}	10^{-8}
S14	10	1.0	$0.5, -1.0$	3, 6	20	10^5	var.	10^{-8}	10^{-8}
S15	10	1.0	$0.5, -1.0$	3, 6	20	10^5	0.01	var.	10^{-8}
S16	10	1.0	$0.5, -1.0$	3, 6	20	10^5	0.01	10^{-8}	var.
S17	200	1.0	$0.5, -1.0$	3, 6	var.	10^5	0.01	10^{-8}	10^{-8}
S18	200	1.0	$0.5, -1.0$	3, 6	20	var.	0.01	10^{-8}	10^{-8}
S19	200	1.0	$0.5, -1.0$	3, 6	20	10^5	var.	10^{-8}	10^{-8}
S20	200	1.0	$0.5, -1.0$	3, 6	20	10^5	0.01	var.	10^{-8}
S21	200	1.0	$0.5, -1.0$	3, 6	20	10^5	0.01	10^{-8}	var.
S22	10	1.0	$1.0, -2.0$	3, 6	var.	10^5	0.01	10^{-8}	10^{-8}
S23	10	1.0	$1.0, -2.0$	3, 6	20	var.	0.01	10^{-8}	10^{-8}
S24	10	1.0	$1.0, -2.0$	3, 6	20	10^5	var.	10^{-8}	10^{-8}
S25	10	1.0	$1.0, -2.0$	3, 6	20	10^5	0.01	var.	10^{-8}
S26	10	1.0	$1.0, -2.0$	3, 6	20	10^5	0.01	10^{-8}	var.
S27	200	1.0	$1.0, -2.0$	3, 6	var.	10^5	0.01	10^{-8}	10^{-8}
S28	200	1.0	$1.0, -2.0$	3, 6	20	var.	0.01	10^{-8}	10^{-8}
S29	200	1.0	$1.0, -2.0$	3, 6	20	10^5	var.	10^{-8}	10^{-8}
S30	200	1.0	$1.0, -2.0$	3, 6	20	10^5	0.01	var.	10^{-8}
S31	200	1.0	$1.0, -2.0$	3, 6	20	10^5	0.01	10^{-8}	var.
S32	10	1.0	$0.5, -1.0$	2, 4	var.	10^5	0.01	10^{-8}	10^{-8}
S33	10	1.0	$0.5, -1.0$	2, 4	20	var.	0.01	10^{-8}	10^{-8}
S34	10	1.0	$0.5, -1.0$	2, 4	20	10^5	var.	10^{-8}	10^{-8}
S35	10	1.0	$0.5, -1.0$	2, 4	20	10^5	0.01	var.	10^{-8}
S36	10	1.0	$0.5, -1.0$	2, 4	20	10^5	0.01	10^{-8}	var.
S37	200	1.0	$0.5, -1.0$	2, 4	var.	10^5	0.01	10^{-8}	10^{-8}
S38	200	1.0	$0.5, -1.0$	2, 4	20	var.	0.01	10^{-8}	10^{-8}
S39	200	1.0	$0.5, -1.0$	2, 4	20	10^5	var.	10^{-8}	10^{-8}
S40	200	1.0	$0.5, -1.0$	2, 4	20	10^5	0.01	var.	10^{-8}
S41	200	1.0	$0.5, -1.0$	2, 4	20	10^5	0.01	10^{-8}	var.

TABLE S2. List of parameter and hyperparameter values used in the simulations of variants of the dissipative Ising chain presented in Figs. S2-S41 in the Supplementary Material. The columns list, in order, total number of sites N, local field strength h, interaction strength(s) $J\,(J_1, J_2)$, interaction decay lengths α_1, α_2, bond dimension χ, total number of Monte Carlo samples per Markov chain N_{MC}, integration tolerance ϵ_{tol}, regularization hyperparameters $\epsilon_{\mathrm{shift}}$ and ϵ_{SNR}. The N_{MC} column lists the total number of Monte Carlo samples used (where $N_{\mathrm{MPI}} = 10$ has been used throughout).

Figure	N	h	$\boldsymbol{J}$ $(\boldsymbol{J}_1, \boldsymbol{J}_2)$	α_1, α_2	χ	N_{MC}	ϵ_{tol}	$\epsilon_{\mathrm{shift}}$	ϵ_{SNR}
S42	10	0.5	(0.6, -0.5, 0.4)	—	var.	10^5	0.05	10^{-8}	10^{-8}
S43	10	0.5	(0.6, -0.5, 0.4)	—	20	var.	0.05	10^{-8}	10^{-8}
S44	10	0.5	(0.6, -0.5, 0.4)	—	20	10^5	var.	10^{-8}	10^{-8}
S45	10	0.5	(0.6, -0.5, 0.4)	—	20	10^5	0.05	var.	10^{-8}
S46	10	0.5	(0.6, -0.5, 0.4)	—	20	10^5	0.05	10^{-8}	var.
S47	50	0.5	(0.6, -0.5, 0.4)	—	var.	10^5	0.05	10^{-8}	10^{-8}
S48	50	0.5	(0.6, -0.5, 0.4)	—	20	var.	0.05	10^{-8}	10^{-8}
S49	50	0.5	(0.6, -0.5, 0.4)	—	20	10^5	var.	10^{-8}	10^{-8}
S50	50	0.5	(0.6, -0.5, 0.4)	—	20	10^5	0.05	var.	10^{-8}
S51	50	0.5	(0.6, -0.5, 0.4)	—	20	10^5	0.05	10^{-8}	var.
S52	10	0.5	(0.6, -0.5, 0.4), (-0.9, 1.0, -1.1)	3, 6	var.	10^5	0.05	10^{-8}	10^{-8}
S53	10	0.5	(0.6, -0.5, 0.4), (-0.9, 1.0, -1.1)	3, 6	20	var.	0.05	10^{-8}	10^{-8}
S54	10	0.5	(0.6, -0.5, 0.4), (-0.9, 1.0, -1.1)	3, 6	20	10^5	var.	10^{-8}	10^{-8}
S55	10	0.5	(0.6, -0.5, 0.4), (-0.9, 1.0, -1.1)	3, 6	20	10^5	0.05	var.	10^{-8}
S56	10	0.5	(0.6, -0.5, 0.4), (-0.9, 1.0, -1.1)	3, 6	20	10^5	0.05	10^{-8}	var.
S57	50	0.5	(0.6, -0.5, 0.4), (-0.9, 1.0, -1.1)	3, 6	var.	10^5	0.05	10^{-8}	10^{-8}
S58	50	0.5	(0.6, -0.5, 0.4), (-0.9, 1.0, -1.1)	3, 6	20	var.	0.05	10^{-8}	10^{-8}
S59	50	0.5	(0.6, -0.5, 0.4), (-0.9, 1.0, -1.1)	3, 6	20	10^5	var.	10^{-8}	10^{-8}
S60	50	0.5	(0.6, -0.5, 0.4), (-0.9, 1.0, -1.1)	3, 6	20	10^5	0.05	var.	10^{-8}
S61	50	0.5	(0.6, -0.5, 0.4), (-0.9, 1.0, -1.1)	3, 6	20	10^5	0.05	10^{-8}	var.

TABLE S3. List of parameter and hyperparameter values used in the simulations of variants of the dissipative XYZ chain presented in Figs. S42-S61 in the Supplementary Material. The columns list, in order, total number of sites N, local field strength h, interaction strength(s) $\boldsymbol{J}$ $(\boldsymbol{J}_1, \boldsymbol{J}_2)$, interaction decay lengths α_1, α_2, bond dimension χ, total number of Monte Carlo samples per Markov chain N_{MC}, integration tolerance ϵ_{tol}, regularization hyperparameters $\epsilon_{\mathrm{shift}}$ and ϵ_{SNR}. The N_{MC} column lists the total number of Monte Carlo samples used (where $N_{\mathrm{MPI}} = 10$ has been used throughout).